



Sound Synthesis and Acoustic Characterization of Rectangular Plates

Martin Czuka, BSc

Master's Thesis

Institute of Electronic Music and Acoustics
Graz University of Music and Performing Arts

Graz University of Technology

Advisor: DI Marian Weger, BSc
Assessor: O.Univ.-Prof. Mag.art DI Dr.techn. Robert Höldrich
Graz, April 2021



Acknowledgements

First of all, I would like to thank everyone who made this work possible with their support:

Prof. Robert Höldrich, thank you very much for the assessment of this thesis. I am grateful for the numerous enlightening discussions as well as for your encouragement and flexibility during every part of the work.

DI Marian Weger, thank you for the supervision of this thesis. Your valuable support and patience during countless meetings in person and online shaped this work significantly. Since the acquired knowledge was often accompanied by new questions out of curiosity, I can only cite Hermann Hesse at this point: *"Alles Wissen und alle Vermehrung unseres Wissens endet nicht mit einem Schlusspunkt, sondern mit Fragezeichen."*

Many thanks to all my colleagues at AIT Austrian Institute of Technology for their professional support as well as their flexibility, which made writing this thesis possible alongside my work at AIT.

Aurora, Erik and Katha, thank you for your unconditional friendship during the years in Graz, Vienna, and any other part of the world. And thank you Aurora for that wonderful custom-made mallet, which hit countless plates and other objects in the name of science.

Finally, I want to thank my parents for their support that gave me the possibility to not only study at university, but enroll in a subject that enriches my life every day. And Christine, having you as a big sister encouraged and still encourages me in treading extraordinary paths. Thank you for that.

Eidesstattliche Erklärung

Ich erkläre an Eides statt, dass ich die vorliegende Arbeit selbstständig verfasst, andere als die angegebenen Quellen / Hilfsmittel nicht benutzt, und die den benutzten Quellen wörtlich und inhaltlich entnommenen Stellen als solche kenntlich gemacht habe.

Wien, 28.04.2021

Ort und Datum

A handwritten signature in blue ink, appearing to read 'Karl G. G. G.', written above a horizontal line.

Unterschrift

Abstract

In everyday life, it is often possible to distinguish physical objects based on the sound that is created by tapping, knocking or scratching them. The perceptibility of object properties such as material, shape and size through acoustic feedback has already been studied in detail.

The aim of this work was to develop a method to conclude on the physical properties of a rectangular plate based on its sound, similar to the capabilities of the human ear. Therefore, the first part of the Master's thesis comprises the implementation of a physical model that simulates the vibration and radiation behaviour of bending waves in rectangular plates using modal synthesis. Inherent thermoelastic and viscoelastic damping as well as the coupling of the plate with the surrounding air were taken into account to simulate the decay of the individual plate modes. In the second part of this work, an analysis of sounds of impacted plates was carried out. The analysis procedure includes the extraction of the plate eigenfrequencies via pitch tracking with a subsequent determination of the model parameters. Based on this information, the material properties and the geometry of the plates were estimated.

Zusammenfassung

Im Alltag ist es oft möglich, physikalische Objekte anhand des Klangs, der durch Tasten, Klopfen oder Kratzen hervorgerufen wird, zu unterscheiden. Die Wahrnehmbarkeit von Objekteigenschaften wie Material, Form, Größe durch dieses akustische Feedback wurde bereits eingehend untersucht.

Ziel dieser Arbeit war es, ein Verfahren zu entwickeln, um - ähnlich dem menschlichen Gehör - aus dem Klang einer rechteckigen Platte auf dessen physikalische Eigenschaften rückzuschließen. Dazu wurde im ersten Teil der Arbeit ein physikalisches Modell implementiert, welches das Schwingungs- und Abstrahlverhalten von BiegeWellen in rechteckigen Platten mittels Modalsynthese simuliert. Die Beschreibung des Abklingverhaltens einzelner Moden erfolgt dabei unter der Berücksichtigung der inhärenten thermo- und viskoelastischen Dämpfung, sowie der Wechselwirkung zwischen der Platte und der umgebenden Luft. Im zweiten Teil wurden Klänge von angeschlagenen Platten analysiert. Die Eigenfrequenzen der angeregten Platten wurden mittels Pitch-Tracking extrahiert, um in weiterer Folge die Modellparameter zu ermitteln. Auf Basis dieser Informationen erfolgte eine Schätzung der Materialeigenschaften sowie der geometrischen Abmessungen der Platten.

Contents

1	Introduction	11
2	Acoustics of Thin Bars and Plates	13
2.1	Free Vibrations in Thin Bars	13
2.1.1	Torsional Waves in Thin Bars	21
2.2	Free Vibrations in Thin Plates	22
2.3	Damped Vibrations in Bars and Plates	33
2.3.1	Damping Mechanisms in Solid Materials	34
2.3.2	Generic Damping Models and Damping Models for Bars	36
2.3.3	Damping Model for Thin Plates	36
2.4	Mechanical Excitation of Objects	41
2.4.1	Hertz's Theory of Contact	41
2.5	Sound Radiation	42
2.5.1	Elementary Radiators	43
2.5.2	Plane, Baffled Radiators	45
2.6	Psychoacoustics of Bars and Plates	45
3	Modal Synthesis of Rectangular Plates	47
3.1	Modal Synthesis Model	48
3.1.1	Damped Mass-Spring System	48
3.1.2	Simulation of Damped Impacted Plates	49
3.2	Implemented Model	50
3.3	Validation	53
4	Acoustic Characterization of Rectangular Plates	65
4.1	Estimation of Eigenfrequencies and Decay Factors	66
4.2	Estimation of Geometry and Material Properties	71
4.3	Case Studies	78

5	Summary and Outlook	81
A	Derivations of Equations Regarded to Thin Rectangular Plates	83
A.1	Potential Energy in a Vibrating Plate	83
A.2	Eigenfrequencies of an Orthotropic Plate	83
A.3	Frequency Correction for Square Modes of a Free Plate	84
B	Modal Densities of Selected Objects	87
B.1	Thin Bars	87
C	Investigated Plates	89
D	FE Simulation Framework and its Validation	91
E	Laser Vibrometer Measurements	93

1 Introduction

Interaction with physical objects in an environment provides acoustic information about their composition via their radiated sounds. By tapping, knocking or scratching objects in everyday life, it is often possible to distinguish between them, based on the perceived acoustic feedback. The radiated sound is determined by its shape and size, its inherent material properties and as well as by the excitation mechanism.

Within the fields of sonic interaction design and sound design, knowledge about the connection between physical properties of an object and the perception of its emitted sound is of vital importance. Furthermore, in robotics not only the location of surrounding objects is crucial but also their composition. One way to detect the material-inherent properties and dimensions would comprise listening to sounds of these objects while striking them. Therefore, one aim of this work was the development of an acoustic characterization method to estimate the material properties and dimensions of objects with focus on rectangular plates. As visualized in figure 1, the method should be able to extract basic information from sounds of impacted plates analogously to the human auditory system.

In order to develop a deeper understanding about the acoustics of rectangular plates, this work also comprises the implementation of a physical model to synthesize the sounds of impacted plates. The implemented synthesis model provides valuable information about the important aspects for the acoustic characterization of rectangular plates and served as basis for the creation of synthesized sounds to validate the acoustic characterization method.

Both parts of this work furthermore aimed to answer the following research questions:

- What object information can be extracted from the sound of an impacted rectangular plate?
- Does the extracted information from a plate sound lead to a more accurate detection of the construction material and the plate dimensions as the human auditory system is capable to detect?

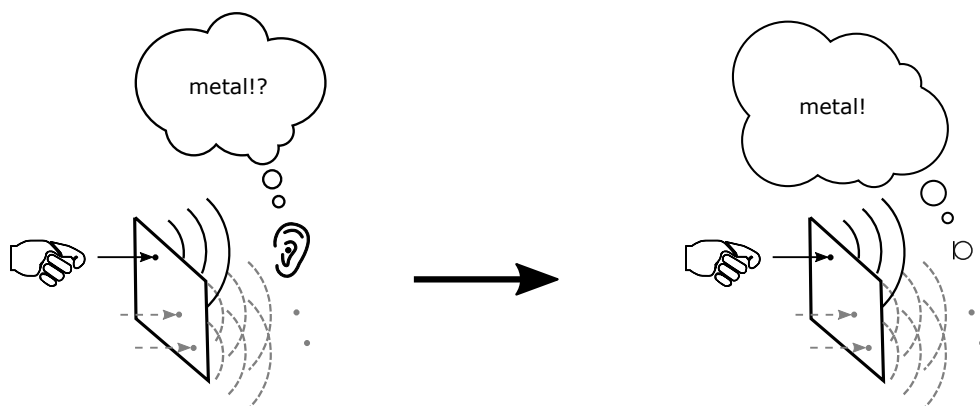


Figure 1 – Schematic principle of acoustic characterization (left) and the developed acoustic characterization method within this work (right).

In order to answer these research questions, a series of investigations was carried out, with the main results and findings being presented in this thesis. Section 2 to 5 of this document cover a detailed description of the following aspects:

- Section 2 comprises the necessary theory to implement a synthesis model for plates and bars using modal synthesis. Furthermore, the main results from already conducted studies, which address the acoustic characterization of simple objects, are summarized.
- The first part of section 3 contains a detailed description of the implemented model to synthesize the sound of an impacted rectangular plate. This also highlights the adaptations from and extensions to already existing plate synthesis models. Within the second part of this section, the validation of the implemented model with acoustic and laser vibrometer measurements from real plates is described.
- Section 4 contains the presentation of the developed method to estimate the physical properties of a rectangular plate from its impact sound. In addition, this part of the thesis includes a validation of the acoustic characterization method with the sounds of real and synthesized impacted plates.
- In section 5 the main findings from the implemented synthesis model and the acoustic characterization method are summarized. The outlook at the end of this chapter points out potential improvements to both the synthesis model as well as the characterization method.

2 Acoustics of Thin Bars and Plates

The present chapter deals with the mathematical description of vibrations in bars and plates with focus on waveforms responsible for sound radiation. Besides a compact summary of well-established knowledge that is available in numerous textbooks about acoustics, it also includes models and findings from publications that are of vital importance for the development of a physical modal synthesis model and the acoustic characterization of plates. In addition, it covers a literature overview of the auditory perception of impacted bars and plates.

2.1 Free Vibrations in Thin Bars

Vibrations in bars are mainly characterized by longitudinal, transversal, torsional and bending waves. The last wave type plays the most significant role for the sound radiation of bars.

Within the Euler-Bernoulli beam theory only bending waves are taken into account. Furthermore, several assumptions are made for the bar. The first states that a bar's length is significantly larger than its other dimensions. According to [1], this assumption holds if the wavelength of the bending wave propagating along the x-axis (see figure 2) is at least 20 times larger than the bar's dimensions in the y- and z-axis. In addition, cross-sectional areas of the bar that were normal to the bar axis before any deformation will remain normal to the bar axis after deformation, as shown in figure 2. The third assumption requires the bending deformation to be small in relation to the length of the bar.

Although the Euler-Bernoulli beam theory is commonly applied to describe the vibrational behaviour of thin bars, it is important to point out its range of validity. For large mode numbers where the transverse dimension of the bar is not negligible compared to the wavelength of the eigenfrequency, the bar cannot be considered as thin. In this case, the Timoshenko beam theory is preferred, since it also considers shear forces. Shear forces decrease the transverse vibration and lower the frequencies of modes for which the bar is not thin. Furthermore, if a bar is excited near an edge, the torsional waves that are not considered in the theory may contribute to the overall sound radiation.

In contrast to a string where the restoring force is caused by an external tension, the restoring force in a bar arises from its stiffness.

Bending waves propagate in a bar according to [2] p. 59 with

$$\frac{\partial^2 W}{\partial t^2} + \frac{EK^2}{\rho} \frac{\partial^4 W}{\partial x^4} = 0. \quad (1)$$

W represents the transverse vibration, E Young's modulus, K the radius of gyration and ρ the density of the bar. A bending wave is a superposition of a longitudinal wave

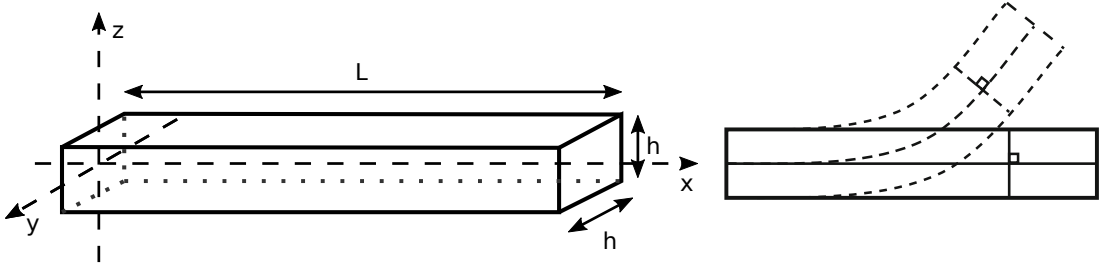


Figure 2 – Geometry (left) and Euler-Bernoulli kinematics (right) of a rectangular bar.

and a transversal wave. The wave propagates with the frequency-dependent speed

$$c = \sqrt{\omega K c_L}, \quad \text{where} \quad c_L = \sqrt{E/\rho} \quad (2)$$

represents the speed of pure longitudinal waves that occur in a bar. Hence, bending waves with a higher frequency propagate faster than at lower frequencies. The resulting dispersion relation between the angular frequency ω and the wavenumber k of the bending wave is

$$\omega = K c_L k^2. \quad (3)$$

The corresponding wavelength λ of the bending wave is proportional to $1/\sqrt{\omega}$ in

$$\lambda = \frac{1}{\sqrt{\omega}} \sqrt{4\pi^2 K c_L}. \quad (4)$$

For a bar with a circular cross section with the radius a and a rectangular cross section with the thickness h , the radii of gyration K are listed in [2] p. 59 with

$$K = \frac{h}{\sqrt{12}}, \quad K = \frac{a}{2}. \quad (5)$$

A well-known solution to equation 1, which contains a single frequency, is

$$W(x, t) = \sin(\omega t + \varphi) [A \cosh(kx) + B \sinh(kx) + C \cos(kx) + D \sin(kx)], \quad (6)$$

where A, B, C and D are assumed to be real-valued constants, that can be determined by defining boundary conditions and initial conditions. In total, four boundary conditions are necessary to establish a relationship between these constants. Three different boundary conditions will be considered, which are summarized in figure 3.

For a **bar free on both ends**, the bending moment and the shear force are zero at the boundaries. This corresponds to

$$\left. \frac{\partial^2 W(x, t)}{\partial x^2} \right|_{x=0, L} = \left. \frac{\partial^3 W(x, t)}{\partial x^3} \right|_{x=0, L} = 0. \quad (7)$$

Inserting equation 6 in 7 and considering both conditions at $x = 0$ leads to the relations

$$C = A \quad \text{and} \quad D = B \quad (8)$$

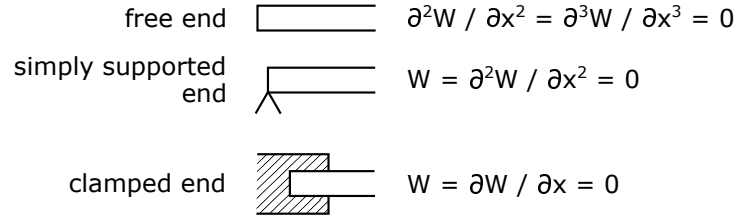


Figure 3 – Typical boundary conditions for a bar and the corresponding derivatives that become zero at the boundary.

for the constants. If these relations are applied on the equations for the remaining boundary conditions at $x = L$, one obtains

$$B = -A \frac{\cos(kL) - \cosh(kL)}{\sin(kL) - \sinh(kL)} = -A\gamma. \quad (9)$$

The resulting eigenfunction consists of the temporal part and the mode shape $\Theta_n(x)$ and equals to

$$\begin{aligned} W_n(x, t) &= A_n \sin(\omega_n t + \varphi_n) [\cos(k_n x) + \cosh(k_n x) - \gamma_n (\sin(k_n x) + \sinh(k_n x))] \\ &= A_n \sin(\omega_n t + \varphi_n) \Theta_n(x), \end{aligned} \quad (10)$$

whereas k_n and ω_n are specific wavenumbers and their associated angular frequencies that solve the bending wave equation with respect to the boundary conditions. Eigenfunctions are also referred to as modes and consist of the spatial mode shape $\Theta_n(x)$ and a time-oscillating part:

$$W_n(x, t) = A_n \Theta_n(x) \sin(\omega_n t + \varphi_n). \quad (11)$$

Due to the orthogonality property of the modes, the scalar product of two mode shapes is

$$\int_0^L \Theta_n(x) \Theta_{n'}(x) dx = 0 \quad \text{for } n \neq n'. \quad (12)$$

As stated in [3], the alternative representation of the mode shape of a bar with free ends

$$\Theta_n(x) = \cos(k_n x) - \gamma_n \sin(k_n x) + \cosh(k_n x) [1 - \gamma_n \tanh(k_n x)], \quad (13)$$

is numerically favourable for large k_n . For determining the allowed k_n and ω_n for the vibrational modes, the equation system

$$\begin{bmatrix} \cosh(k_n L) - \cos(k_n L) & \sinh(k_n L) - \sin(k_n L) \\ \sinh(k_n L) + \sin(k_n L) & \cosh(k_n L) - \cos(k_n L) \end{bmatrix} \begin{bmatrix} A \\ B \end{bmatrix} = \begin{bmatrix} 0 \\ 0 \end{bmatrix} \quad (14)$$

can be derived by considering the boundary conditions in equation 7. In order to obtain a non-trivial solution, the determinant of the matrix has to be zero. This occurs, if the equation

$$\cos(k_n L) = \frac{1}{\cosh(k_n L)} \quad (15)$$

or its alternate form

$$\tan\left(\frac{k_n L}{2}\right) = \pm \tanh\left(\frac{k_n L}{2}\right) \quad (16)$$

are fulfilled. The equations have an infinite number of solutions which can be determined numerically. Approximate values for these $k_n L$ are listed in table 1. By using the k_n in the dispersion relation in equation 3, one can calculate the eigenfrequencies of a bar with free ends. In [2] p. 62, the determination of these eigenfrequencies is approximated and simplified to

$$f_n = \beta \frac{K}{L^2} \sqrt{\frac{E}{\rho}}, \quad \beta = \frac{\pi}{8} \begin{cases} 3.011^2, & n = 1 \\ (2n + 1)^2, & n = 2, 3, 4, \dots \end{cases} \quad (17)$$

Note that there is no harmonic relation between the eigenfrequencies for this boundary condition, as the relations f_n/f_1 in table 1 show. Figure 4 illustrates exemplary bending modes of a bar with free ends. Beside the above eigenfunctions and eigenfrequencies for $n \geq 1$, two rigid body modes $W_{0,0}$ and $W_{0,1}$ exist for a free bar. For these special cases, $k_0 = 0$ and the resulting eigenfrequency is zero. In [3], the corresponding eigenfunctions that solve the bending wave equation in this case are given as

$$W_{0,0}(x, t) = A, \quad W_{0,1}(x, t) = A \frac{x}{L}. \quad (18)$$

A bar with one clamped and one free end, also called cantilever beam, represents a frequently encountered setup. At the clamped end, the transverse displacement and its slope vanish:

$$W(x, t) \Big|_{x=0} = \frac{\partial W(x, t)}{\partial x} \Big|_{x=0} = 0. \quad (19)$$

The free end at $x = L$ is described by equation 7. Applying these four conditions to equation 6 leads to the mode shape

$$\Theta_n(x) = -\cos(k_n x) + \cosh(k_n x) - \gamma_n [-\sin(k_n x) + \sinh(k_n x)] \quad (20)$$

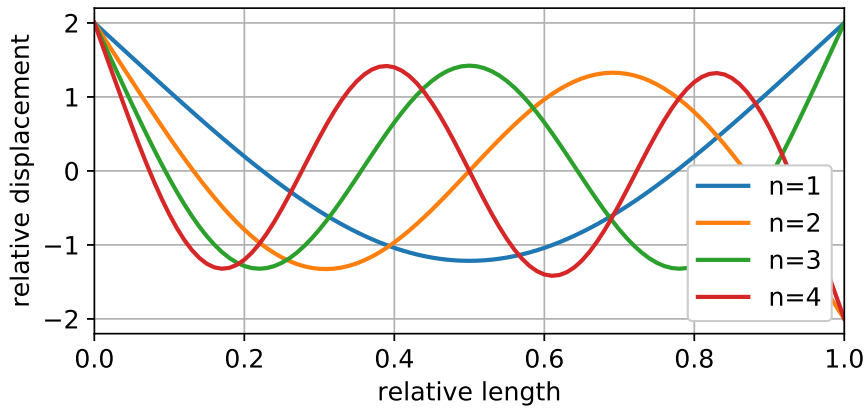


Figure 4 – First four bending mode shapes on a bar with free ends, not including rigid body modes.

Table 1 – Normalized eigenfrequencies, normalized wavelengths, nodal positions and allowed $k_n L$ for the first four bending modes of a bar with free ends, not including rigid body modes.

n	f_n/f_1	λ_n/L	nodal positions / L	$k_n L$
1	1.000	1.328	{0.224, 0.776}	4.730
2	2.758	0.8	{0.132, 0.5, 0.868}	7.853
3	5.405	0.571	{0.094, 0.356, 0.644, 0.906}	10.996
4	8.934	0.444	{0.073, 0.277, 0.5, 0.723, 0.927}	14.137

with

$$\gamma = \frac{\cos(k_n L) + \cosh(k_n L)}{\sin(k_n L) + \sinh(k_n L)}. \quad (21)$$

For large k_n , the representation

$$\Theta_n(x) = \cos(k_n x) - \gamma_n \sin(k_n x) + \cosh(k_n x) [1 - \gamma_n \tanh(k_n x)] \quad (22)$$

is preferred for numerical reasons. The eigenfrequencies can be determined with the same procedure as described for the bar with free ends. Analogous to equation 15, the transcendental equation that leads to eigenfrequencies is now

$$\cot\left(\frac{k_n L}{2}\right) = \pm \tanh\frac{k_n L}{2}. \quad (23)$$

Solving this equation approximately leads to the relation

$$f_n = \beta \frac{K}{L^2} \sqrt{\frac{E}{\rho}}, \quad \beta = \frac{\pi}{8} \begin{cases} 1.194^2, & n = 1 \\ 2.988^2, & n = 2 \\ (2n - 1)^2, & n = 3, 4, 5, \dots \end{cases} \quad (24)$$

for the eigenfrequencies. Compared to a bar with free ends, the fundamental frequency f_1 is about a 1/6 of f_1 of a free bar. Furthermore, the eigenfrequencies of a bar with one clamped and one free end increase approximately with the quadratic term $(2n - 1)^2$ while the frequencies of a free bar increase by $(2n + 1)^2$. Table 2 shows that as for a bar with free ends, eigenfrequencies with $n \geq 2$ are not harmonics of the fundamental frequency. Exemplary bending modes of a bar with a clamped and a free end are depicted in figure 5.

For a bar that is simply supported or hinged at both ends the boundary conditions are

$$W(x, t) \Big|_{x=0, L} = \frac{\partial^2 W(x, t)}{\partial x^2} \Big|_{x=0, L} = 0. \quad (25)$$

Inserted into equation 6, the resulting mode shape reduces to

$$\Theta_n(x) = \sin(k_n x). \quad (26)$$

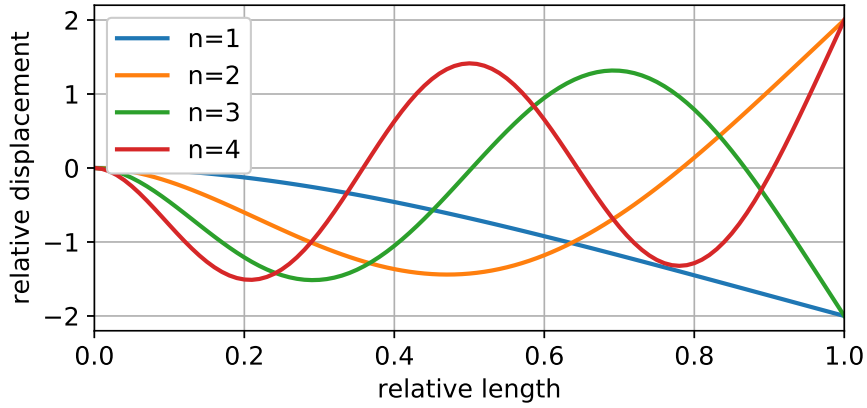


Figure 5 – First four bending mode shapes on a bar with one clamped end and one free end.

As figure 6 indicates, the mode shapes are equivalent to those of a vibrating string fixed at both ends. The eigenfrequencies f_n are harmonically related too, but differ from those of the string and equal to

$$f_n = \beta \frac{K}{L^2} \sqrt{\frac{E}{\rho}}, \quad \beta = \frac{\pi}{2} n^2, \quad n = 1, 2, 3, \dots \quad (27)$$

Compared to the eigenfrequencies from the previously described boundary conditions, the fundamental frequency of a hinged bar is significantly lower than the one of a free bar, but higher as for the cantilever condition. As shown in figure 7, the modal density of a bar decreases with increasing frequency. In contrast to the vibrating string where a larger thickness results in a decrease of the eigenfrequencies, the bending wave frequencies of a bar increase with a larger thickness h . Furthermore, doubling the length of the bar leads to a quartering of the eigenfrequencies.

Table 2 – Normalized eigenfrequencies, normalized wavelengths, nodal positions and allowed $k_n L$ for the first four bending modes of a bar with one clamped and one free end.

n	f_n/f_1	λ_n/L	nodal positions / L	$k_n L$
1	1.000	3.350	{0}	1.875
2	6.263	1.339	{0, 0.783}	4.694
3	17.536	0.800	{0, 0.504, 0.868}	7.855
4	34.371	0.571	{0, 0.358, 0.644, 0.906}	10.996

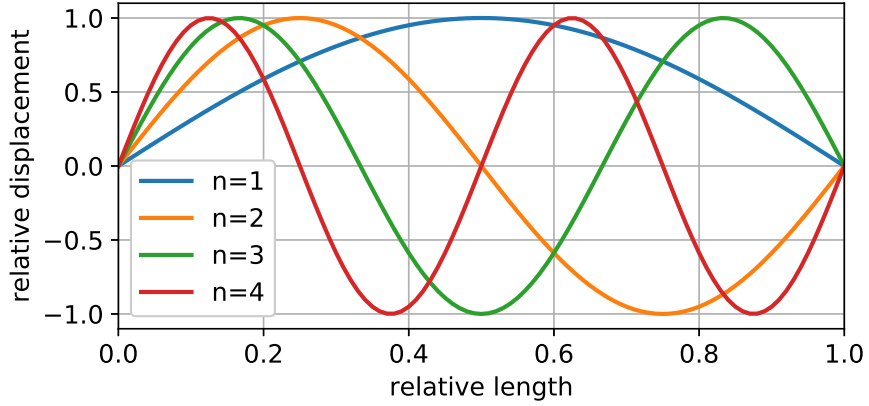


Figure 6 – First four bending mode shapes on a bar with hinged ends.

A more general method to determine the eigenfrequency of a bending wave in a bar is based on Rayleigh's principle. It considers the vibrating bar as a system with the constant total mechanical energy consisting of the potential energy E_{pot} and the kinetic energy E_{kin} . For a transverse displacement $W(x, t)$, those energies are

$$E_{pot} = \frac{1}{2} \int_0^L ESK^2 \left(\frac{d^2W}{dx^2} \right)^2 dx \quad (28)$$

and

$$E_{kin} = \frac{1}{2} \int_0^L \rho S \left(\frac{dW}{dt} \right)^2 dx, \quad (29)$$

where S is the cross-sectional area of the bar. Assuming that the mechanical energy stays constant in the bar, the amplitudes of E_{pot} and E_{kin} for a time-oscillating bending mode $W_n(x, t) = \Theta_n(x) \cos(\omega_n t + \varphi_n)$ are equal. Thereby, the corresponding angular eigenfrequency ω_n for a bar is

$$\omega_n = \sqrt{\frac{\int_0^L ESK^2 \left(\frac{d^2\Theta_n}{dx^2} \right)^2 dx}{\int_0^L \rho S \Theta_n^2 dx}}, \quad (30)$$

Table 3 – Normalized eigenfrequencies, normalized wavelengths and nodal positions for the first four bending modes of a bar with simply supported ends.

n	f_n/f_1	λ_n/L	nodal positions / L
1	1	2	{0, 1}
2	4	1	{0, 0.5, 1}
3	9	$0.\bar{6}$	{0, 0. $\bar{3}$, 0. $\bar{6}$, 1}
4	16	0.5	{0, 0.25, 0.5, 0.75, 1}

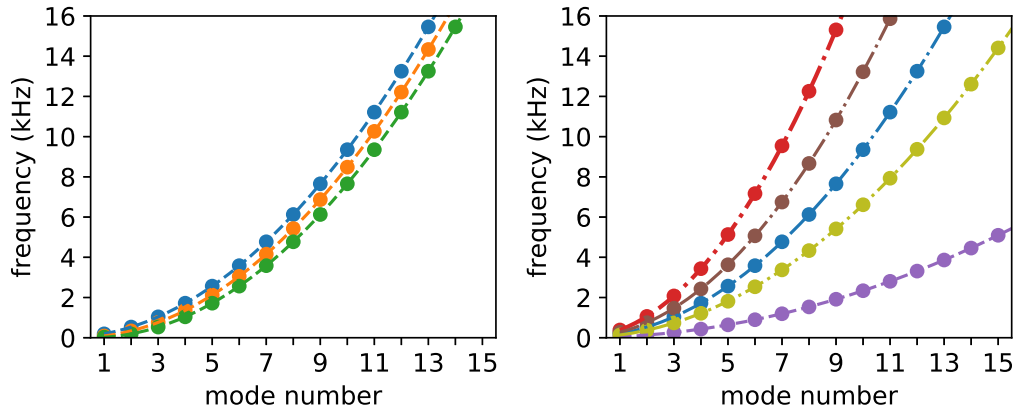


Figure 7 – Bending mode eigenfrequencies for different boundary conditions of the same bar (left) for the conditions free (blue), simply supported (orange), clamped-free (green) and for a free bar (right) when doubling the following bar properties: thickness (red), Young’s modulus (brown), density (lime) and length (violet). The dashed curves have no physical meaning but indicate modes of the same boundary condition / object dimensions / material properties.

as stated in [3]. Equation 30 expressed with ω_n^2 is also called Rayleigh quotient. It allows the determination of ω_n for any eigenfunction W_n that satisfies the defined boundary conditions of the bar.

Besides the eigenfrequencies and the mode shapes the modal density is a useful quantity to characterize vibrational properties of a bar. Being a statistical measure, the modal density $D(f)$ describes the number of modes per Hz. As mentioned in [4] and derived in detail in Appendix B, the modal density is

$$D(f) = \frac{2L}{c} \quad (31)$$

for all combinations of free, simply supported and clamped boundary conditions. The influence of the frequency-dependent bending wave speed c leads to a decrease of the modal density with the factor $1/\sqrt{f}$.

Figure 8 shows a comparison of the discussed combinations of boundary conditions for a selected mode shape Θ_n . The node observed at approximately $0.13 L$ for a bar with free ends moves outwards to the end if the left end of the bar gets clamped or simply-supported. In contrast to a simply supported end, the area around the clamped and free end is dominated by the exponential behaviour of the hyperbolic functions of the mode shapes.

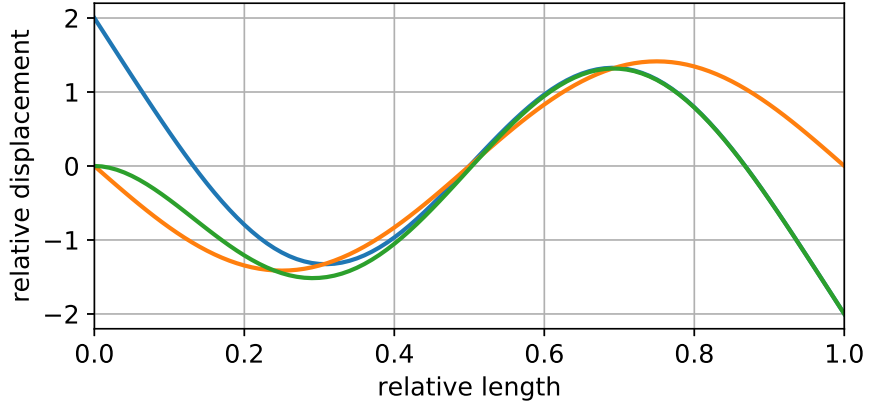


Figure 8 – Comparison between the normalized mode shapes of a bar with free ends (blue), one clamped and one free end (green) and simply supported ends (orange).

2.1.1 Torsional Waves in Thin Bars

Although not taken into account by the Euler-Bernoulli beam theory, torsional waves may contribute to the radiated sound, especially if the bar is excited near an edge. In contrast to bending waves, torsional waves are non-dispersive and propagate with the speed

$$c_T = \sqrt{\frac{GK_T}{\rho I_p}}, \quad (32)$$

where the shear modulus G is

$$G = \frac{E}{2(1 + \nu)}, \quad (33)$$

and I_p represents the polar moment of inertia. For a rectangular cross section with the width L_y and a circular cross section with the radius a , the polar moments of inertia are

$$I_p = \frac{L_y h}{12} (L_y^2 + h^2), \quad I_p = \frac{1}{2} \pi a^4, \quad (34)$$

and the factors K_T are given by

$$K_T = \frac{L_y h^3}{16} \left[\frac{16}{3} - 3.36 \frac{h}{L_y} \left(1 - \frac{h^4}{12L_y^4} \right) \right], \quad K_T = \frac{1}{2} \pi a^4. \quad (35)$$

The torsional eigenfrequencies $f_{T,n}$ of a bar can be determined with

$$f_{T,n} = \beta_{T,n} \frac{c_T}{2L}. \quad (36)$$

Depending on the boundary condition listed in table 4, the factor $\beta_{T,n}$ may lead to torsional eigenfrequencies that are harmonically related to $f_{T,1}$.

Table 4 – Boundary condition (bc) dependent expressions for the factor $\beta_{T,n}$ for a bar with free ends (ff), clamped ends (cc), one clamped and one free end (cf).

bc	$\beta_{T,n}$	allowed n
ff / cc	n	1, 2, 3, ...
cf	$n + \frac{1}{2}$	0, 1, 2, ...

2.2 Free Vibrations in Thin Plates

Like in a bars, longitudinal, transversal, torsional and bending waves can propagate in plates. With bending waves being the most significant type for the radiation of sound, the widely employed Kirchoff-Love plate theory is presented in this section. It involves the same assumptions as the Euler-Bernoulli beam theory except that both the plates length and width are much larger than its thickness, as illustrated in figure 9 for a rectangular plate. Hence, this plate theory can be interpreted as an extension of the bending wave equation to a second spatial dimension. In case of an orthotropic plate, the elastic material properties do now depend also on the spatial direction. Within the scope of this thesis, orthotropy in a plate is associated with different elastic constants along the x-axis and y-axis as in figure 9.

In a thin orthotropic homogeneous plate with the thickness h , bending waves propagate according to [5] p. 24 with

$$\frac{\rho}{h^2} \frac{\partial^2 W}{\partial t^2} + D_1 \frac{\partial^4 W}{\partial x^4} + D_3 \frac{\partial^4 W}{\partial y^4} + (D_2 + D_4) \frac{\partial^4 W}{\partial x^2 \partial y^2} = 0, \quad (37)$$

where W is the transverse displacement. The four rigidity constants D_1 to D_4 are required to describe the potential energy in the plate and are given by

$$\begin{aligned} D_1 &= \frac{E_x}{12(1 - \nu_{xy}\nu_{yx})}, \\ D_2 &= \frac{E_x\nu_{yx}}{6(1 - \nu_{xy}\nu_{yx})} = \frac{E_y\nu_{xy}}{6(1 - \nu_{xy}\nu_{yx})}, \\ D_3 &= \frac{E_y}{12(1 - \nu_{xy}\nu_{yx})}, \quad D_4 = \frac{G_{xy}}{3}. \end{aligned} \quad (38)$$

The indices x and y indicate the direction dependency of Young's modulus E , the in-plane shear modulus G_{xy} and Poisson's ratio ν in Cartesian coordinates. With the bending moments \mathcal{M}_x , \mathcal{M}_y and the twisting moment \mathcal{M}_{xy} the relation between the rigidity constants and the corresponding displacement curvature can be described as

$$\begin{bmatrix} \mathcal{M}_x \\ \mathcal{M}_y \\ \mathcal{M}_{xy} \end{bmatrix} = -h^3 \begin{bmatrix} D_1 & D_2/2 & 0 \\ D_2/2 & D_3 & 0 \\ 0 & 0 & D_4/2 \end{bmatrix} \begin{bmatrix} \partial^2 W / \partial x^2 \\ \partial^2 W / \partial y^2 \\ \partial^2 W / (\partial x \partial y) \end{bmatrix}. \quad (39)$$

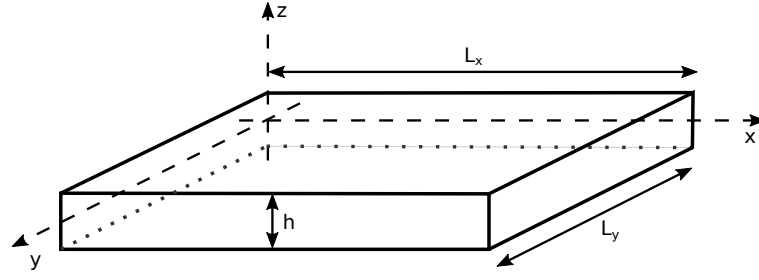


Figure 9 – Geometry of a rectangular plate.

If the plate's material shows an isotropic behaviour, then $E_x = E_y = E$, $\nu_{xy} = \nu_{yx} = \nu$ and the in-plane shear modulus becomes $G_{xy} = E/(2(1+\nu))$. Subsequently, the rigidity constants can be rewritten to

$$D_1 = D_3 = \frac{E}{12(1-\nu^2)} = D, \quad D_4 = \frac{E}{6(1+\nu)}, \quad (40)$$

and

$$D_2 = 2D_1 - D_4 = \frac{E\nu}{6(1-\nu^2)}. \quad (41)$$

This leads to the homogeneous bending wave equation for a thin isotropic homogeneous plate independent of the coordinate system

$$\frac{\rho}{h^2} \frac{\partial^2 W}{\partial t^2} + D \nabla^4 W = 0 \quad (42)$$

that includes the biharmonic operator ∇^4 . As for bars, the speed of bending waves depends on the frequency and is for an isotropic plate

$$c = \sqrt{\omega K c_L} \quad \text{with} \quad K = \frac{h}{\sqrt{12}}, \quad (43)$$

with c_L being the propagation speed of longitudinal waves in an infinite plate:

$$c_L = \sqrt{\frac{E}{\rho(1-\nu^2)}}. \quad (44)$$

For a rectangular plate the biharmonic operator ∇^4 in Cartesian coordinates equals to

$$\nabla^4 = \frac{\partial^4}{\partial x^4} + 2 \frac{\partial^4}{\partial x^2 \partial y^2} + \frac{\partial^4}{\partial y^4}. \quad (45)$$

A time-oscillating solution that solves the homogeneous differential equation for a rectangular plate has a form of

$$W(x, y, t) = AX(x)Y(y) \sin(\omega t + \varphi), \quad (46)$$

whereas $X(x)$ and $Y(y)$ represent functions which depend on a single spatial direction, and a weighting factor A . For describing the boundary conditions, a rectangular plate

as depicted in figure 9 with the dimensions L_x and L_y is assumed. Analogous to the bending modes of a bar, the corresponding modes of a plate can be written as

$$W_{mn}(x, y, t) = A_{mn} \Theta_{mn}(x, y) \sin(\omega_{mn}t + \varphi_{mn}) \quad \text{with} \quad \Theta_{mn} = X_m(x)Y_n(y). \quad (47)$$

Because of their orthogonality property, the plate bending mode shapes Θ_{mn} fulfill

$$\int_0^{L_y} \int_0^{L_x} \Theta_{mn}(x, y) \Theta_{m'n'}(x, y) dx dy = 0 \quad \text{for} \quad m \neq m' \vee n \neq n'. \quad (48)$$

In contrast to a bar, the dispersion relation

$$\omega = K_{CL} k^2 \quad (49)$$

can only be used for specific boundary conditions to determine the eigenfrequencies for a certain wavenumber k . For a plate that is simply supported on all edges, k is a 2-dimensional wavenumber vector $k = \sqrt{k_x^2 + k_y^2}$ of the bending wave. Hence, for every eigenfrequency of the plate there are a wavelength λ_x in x-direction and a wavelength λ_y in y-direction that depend on the boundary conditions of the plate.

Finding mode shapes and corresponding eigenfrequencies that solve the Kirchhoff-Love plate equation is a problem that has been studied by countless authors in the past. A comprehensive summary of these attempts was published by Leissa in [6] that also includes an approach by Warburton from [7]. Warburton used characteristic beam functions for $X(x)$ and $Y(y)$ to obtain the plate bending modes to solve equation 42 for combinations of free, clamped and simply supported edges. Furthermore, he presented a simple equation to determine the associated eigenfrequencies based on the mode shapes and the Rayleigh quotient. In this document, only combinations of boundary conditions relevant for this work, which are depicted in figure 10, are described from his approach. It is known that the characteristic beam functions lead to modes that solve the bending wave equation only approximately if free edges are involved. The accuracy of the approach is also discussed on the next pages. Note that although in the first place considered for rectangular isotropic plates, the derived mode shapes Θ_{mn} can also be used to solve equation 37 and are therefore also valid for orthotropic plates.

In case of a **rectangular plate that is simply supported on all edges**, the displacement and the bending moments perpendicular to the edges must vanish:

$$\begin{aligned} W(x, y, t) \Big|_{x=0, L_x} &= W(x, y, t) \Big|_{y=0, L_y} = 0, \\ \mathcal{M}_x(x, y, t) \Big|_{x=0, L_x} &= \mathcal{M}_y(x, y, t) \Big|_{y=0, L_y} = 0. \end{aligned} \quad (50)$$

The functions $X(x)$ and $Y(y)$ then become

$$X(x) = \sin\left(\frac{(m-1)\pi x}{L_x}\right) \quad m = 2, 3, 4, \dots,$$

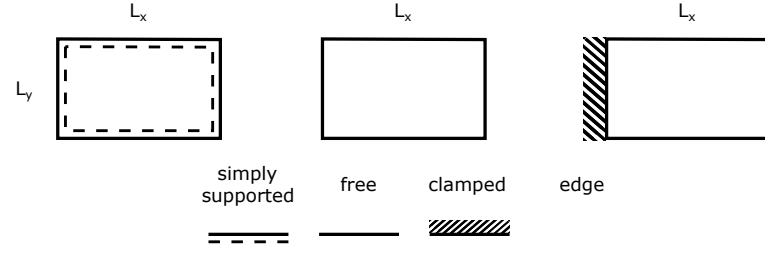


Figure 10 – Top view of selected boundary conditions of a rectangular plate.

$$Y(y) = \sin\left(\frac{(n-1)\pi y}{L_y}\right) \quad n = 2, 3, 4, \dots \quad (51)$$

Hence, the mode shape

$$\Theta_{mn}(x, y) = \sin\left(\frac{(m-1)\pi x}{L_x}\right) \sin\left(\frac{(n-1)\pi y}{L_y}\right) \quad (52)$$

obtained from equation 47 does solve the plate bending wave equation exactly with the corresponding eigenfrequency. Furthermore, the shapes are equivalent to the one of a rectangular membrane with fixed edges. The exemplary mode shapes depicted in figure 11 show that the nodal lines are always parallel to the edges of the plate. This behaviour does not change, even for square plates. Note that compared to the allowed mode numbers of the eigenfunctions of a bar, the simply supported plate starts with mode numbers $m \geq 2$ and $n \geq 2$. This convention considers the number of nodal lines parallel to a pair of edges, if present.

A plate that is free at all four edges must fulfill the conditions

$$\mathcal{M}_x(x, y, t) \Big|_{x=0, L_x} = \mathcal{M}_y(x, y, t) \Big|_{y=0, L_y} = 0, \quad (53)$$

$$\mathcal{F}_x(x, y, t) \Big|_{x=0, L_x} = \mathcal{F}_y(x, y, t) \Big|_{y=0, L_y} = 0, \quad (54)$$

where the shear force in x-direction \mathcal{F}_x of an orthotropic plate is

$$\mathcal{F}_x = \frac{\partial \mathcal{M}_x}{\partial x} + \frac{\partial}{\partial y} \left(h^3 D_4 \frac{\partial^2 W}{\partial x \partial y} \right). \quad (55)$$

The shear force in y-direction \mathcal{F}_y can be obtained by swapping the variables x and y in the equation above. At the corner of two free edges of a plate, the twisting moment

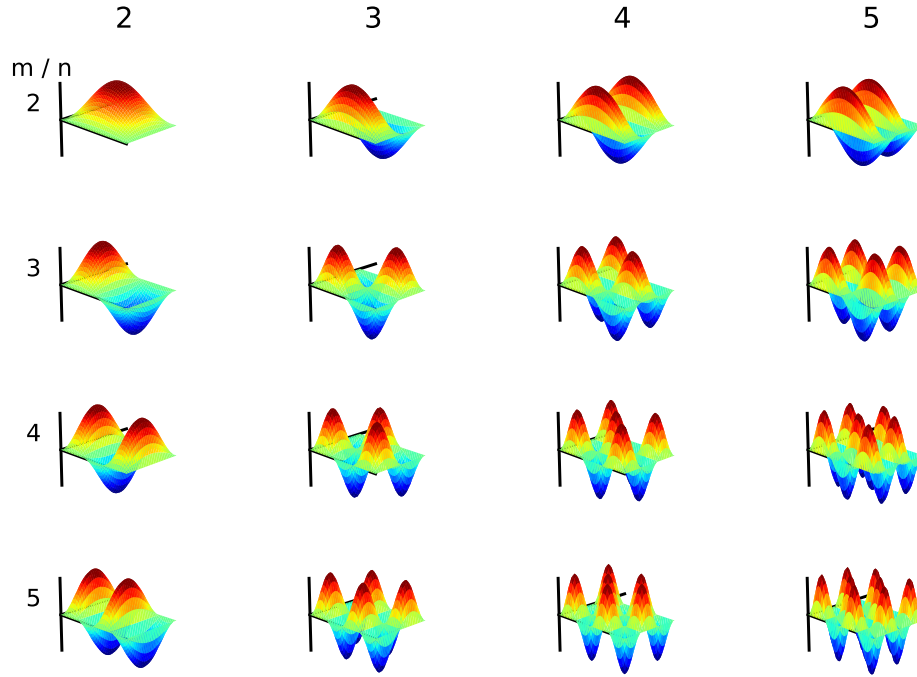


Figure 11 – Exemplary normalized vibrational mode shapes of a rectangular plate with simply supported edges.

must fulfill

$$\mathcal{M}_{xy} \Big|_{x=0,y=0} = \mathcal{M}_{xy} \Big|_{x=L_x,y=L_y} = 0. \quad (56)$$

If the plate material is isotropic and homogeneous, the conditions at the edges simplify to

$$\frac{\partial^2 W}{\partial x^2} + \nu \frac{\partial^2 W}{\partial y^2} \Big|_{x=0,L_x} = \frac{\partial^2 W}{\partial y^2} + \nu \frac{\partial^2 W}{\partial x^2} \Big|_{y=0,L_y} = 0, \quad (57)$$

and

$$\frac{\partial^3 W}{\partial x^3} + (2 - \nu) \frac{\partial^3 W}{\partial x \partial y^2} \Big|_{x=0,L_x} = \frac{\partial^3 W}{\partial y^3} + (2 - \nu) \frac{\partial^3 W}{\partial y \partial x^2} \Big|_{y=0,L_y} = 0. \quad (58)$$

Warburton found the following characteristic beam functions that approximately satisfy those boundary conditions:

$$X(x) = \begin{cases} 1 & m = 0, \\ 1 - \frac{2x}{L_x} & m = 1, \\ \cos\left(\beta\left(\frac{x}{L_x} - \frac{1}{2}\right)\right) + \gamma \cosh\left(\beta\left(\frac{x}{L_x} - \frac{1}{2}\right)\right) & m = 2, 4, 6, \dots, \\ \sin\left(\beta'\left(\frac{x}{L_x} - \frac{1}{2}\right)\right) + \gamma' \sinh\left(\beta'\left(\frac{x}{L_x} - \frac{1}{2}\right)\right) & m = 3, 5, 7, \dots, \end{cases} \quad (59)$$

with

$$\gamma = -\frac{\sin\left(\frac{1}{2}\beta\right)}{\sinh\left(\frac{1}{2}\beta\right)}, \quad \gamma' = \frac{\sin\left(\frac{1}{2}\beta'\right)}{\sinh\left(\frac{1}{2}\beta'\right)}, \quad (60)$$

where β and β' are the $\lfloor m/2 \rfloor$ -th non-zero positive roots of the equations

$$\tan\left(\frac{1}{2}\beta\right) + \tanh\left(\frac{1}{2}\beta\right) = 0, \quad \tan\left(\frac{1}{2}\beta'\right) - \tanh\left(\frac{1}{2}\beta'\right) = 0 \quad (61)$$

for the spatial solution in x-dimension. If X, x, L_x, m in equation 59 and 60 are substituted by Y, y, L_y, n , one obtains the beam function $Y(y)$ in y-dimension. For plates with the aspect ratio $r_a = L_x/L_y$ much larger or much smaller than one, the resulting mode shapes for this boundary condition can be determined by inserting $X(x)$ and $Y(y)$ into equation 47. As visible in figure 12, the nodal lines of the shapes are always parallel to one pair of edges. However, if r_a approaches the value one, elastic interaction occurs between modes with the mode numbers $\{m, n\}$ and $\{n, m\}$ that leads to mode shapes different than depicted in figure 12. Furthermore, the nodal lines are not parallel to one pair of edges and the resulting mode shapes are not of the type $\{m, n\}$ and $\{n, m\}$, but $\{m, n\} \pm \{n, m\}$ as r_a approaches the value one. This mixing of the shapes, e.g. of the modes $\{2, 0\}$ and $\{0, 2\}$ leads to a nodal cross for $\{2, 0\} + \{0, 2\}$ or a nodal ring for $\{2, 0\} - \{0, 2\}$, as visualized in figure 13. Consequently, the mixed mode shapes $\Theta'_{mn\pm}$ for a free plate can be expressed with

$$\Theta'_{mn\pm} = A\Theta_{mn} \pm B\Theta_{nm}, \quad (62)$$

where Θ_{mn} and Θ_{nm} are the mode shapes without the effect of elastic interaction. In [7], Warburton determined the factors A and B for certain modes by using the Rayleigh-Ritz method. It must be noted that the elastic interaction depending on the aspect ratio also

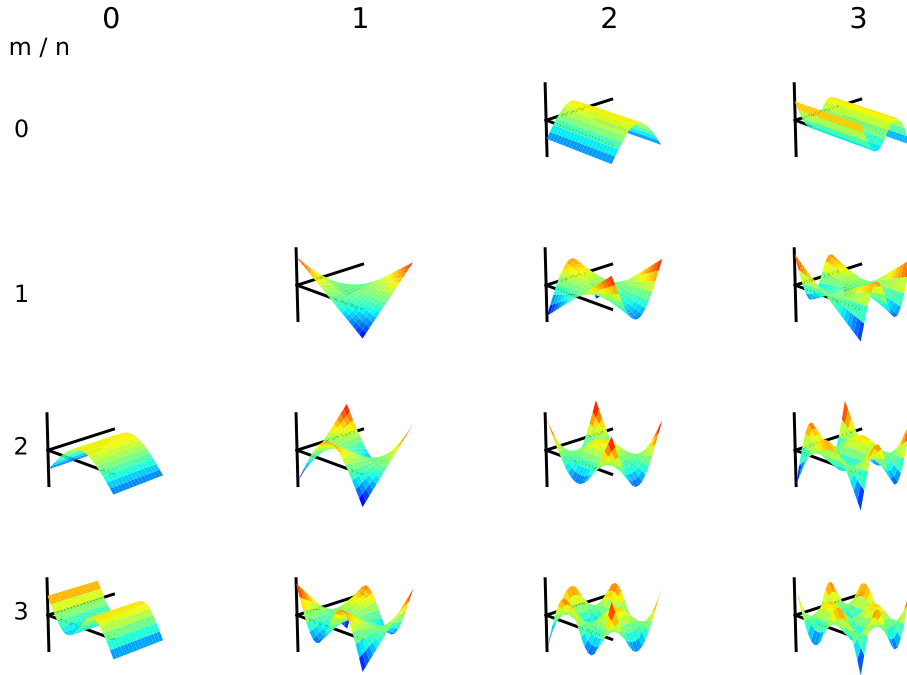


Figure 12 – Exemplary normalized vibrational mode shapes of a rectangular plate with free edges according to Warburton that lead to an eigenfrequency $\neq 0$.

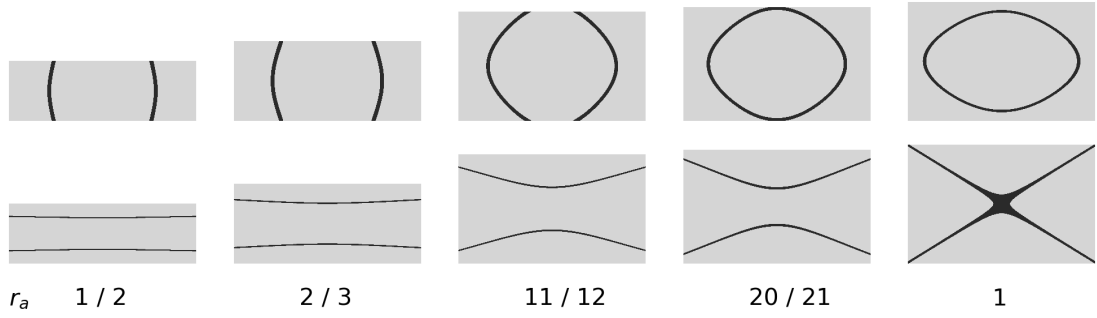


Figure 13 – Nodal patterns for the mode shapes $\{2, 0\} + \{0, 2\}$ (top) and $\{2, 0\} - \{0, 2\}$ (bottom) for different aspect ratios of a free plate after Warburton [7]. Not to scale.

affects the eigenfrequencies of a rectangular free plate, if $m - n$ is an even number except zero. This influence is discussed later in this section.

The so-called **cantilever plate** has one fixed edge beside three free edges. Assuming that the plate is fixed at $x = 0$ and free at $x = L_y$, $y = 0$, $y = L_y$, the beam function in x-direction is

$$X(x) = \cos\left(\frac{\beta x}{L_x}\right) - \cosh\left(\frac{\beta x}{L_x}\right) - \gamma \left[\sin\left(\frac{\beta x}{L_x}\right) - \sinh\left(\frac{\beta x}{L_x}\right) \right]$$

with

$$\gamma = \frac{\sin(\beta) - \sinh(\beta)}{\cos(\beta) - \cosh(\beta)}, \quad \cos(\beta) \cosh(\beta) = -1, \quad (63)$$

for

$$m = 1, 2, 3, \dots$$

As for two opposing free edges, this beam function solves the free edge boundary condition at $x = L_y$ only approximately. The beam function $Y(y)$ for the cantilever plate is the same $Y(y)$ as for the plate with all free edges.

Exemplary mode shapes for the described boundary conditions are visualized in the figures 11, 12 and 14. Note that for a rectangular plate with free edges the mode $\{0, 0\}$, the mode $\{1, 0\}$ and the mode $\{0, 1\}$ are not depicted since they represent rigid body modes with an eigenfrequency of zero. Furthermore, for a free plate eigenmodes with one mode number being zero lead to shapes of a two-dimensional free bar as depicted in figure 12, if the plates aspect ratio r_a is much larger or much smaller than 1. The same is true for the cantilever plate - if the mode number associated to the two opposing free edges is zero, one obtains the mode shapes of a two-dimensional bar with one clamped and one free edge.

As already indicated, the mode shapes resulting from a plate that includes one or more free edges only solve the Kirchhoff-Love plate equation approximately. For a plate with free edges only, e.g. the twisting moments \mathcal{M}_{xy} and \mathcal{M}_{yx} of the mode $\{1, 1\}$ do not va-

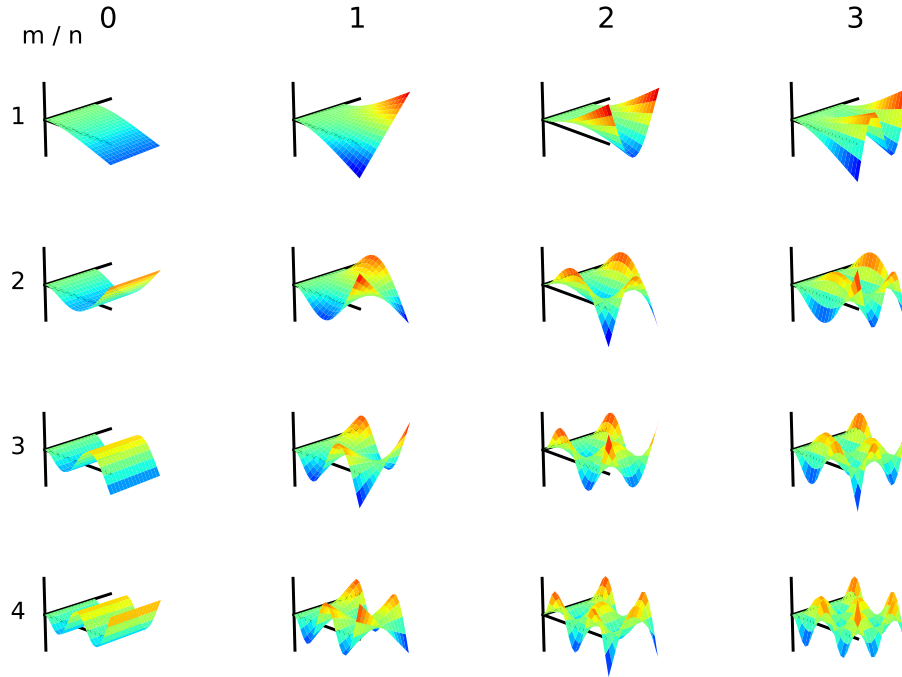


Figure 14 – Exemplary normalized vibrational mode shapes of a rectangular plate with one clamped and three free edges according to Warburton.

-nish at the corners of the plate. Hence, such errors propagates to all calculations that rely on mode shapes, such as Warburton’s simple approach to determine the eigenfrequencies of a rectangular plate. Despite being only an approximation for certain boundary conditions, Warburton’s mode shapes can be applied regardless whether the plate is isotropic or orthotropic. However, the same mode shapes of an isotropic and orthotropic plate with the same dimensions have different associated eigenfrequencies, as the next pages will show.

In order to obtain the eigenfrequencies that solve the bending wave equation for various boundary conditions, an approach has been presented in [7]. It is based on Rayleigh’s quotient which has already been introduced in section 2.1. A vibrating plate with the transverse displacement W has the potential energy

$$E_{pot} = \frac{h^3}{2} \int_{y=0}^{L_y} \int_{x=0}^{L_x} \left[D_1 \left(\frac{\partial^2 W}{\partial x^2} \right)^2 + D_2 \frac{\partial^2 W}{\partial x^2} \frac{\partial^2 W}{\partial y^2} + D_3 \left(\frac{\partial^2 W}{\partial y^2} \right)^2 + D_4 \left(\frac{\partial^2 W}{\partial x \partial y} \right)^2 \right] dx dy \quad (64)$$

and the kinetic energy

$$E_{kin} = \frac{\rho h}{2} \int_{y=0}^{L_y} \int_{x=0}^{L_x} \left(\frac{\partial^2 W}{\partial t^2} \right)^2 dx dy. \quad (65)$$

If the total mechanical energy consisting of E_{kin} and E_{pot} stays constant, the circular eigenfrequency ω_{mn} of a time-oscillating bending mode of the form

$$W_{mn}(x, y, t) = \Theta_{mn}(x, y) \sin(\omega_{mn}t + \varphi_{mn}) \quad \text{is} \quad \omega_{mn} = \sqrt{\frac{E_{pot,max}}{E_{kin,max}}}, \quad (66)$$

where $E_{pot,max} = E_{pot}(W_{mn} = \Theta_{mn})$ and $E_{kin,max} = E_{kin}(\partial^2 W_{mn}/\partial t^2 = \Theta_{mn})$. With equation 66, one can determine the eigenfrequencies accurately for boundary conditions that contain only simply supported and clamped edges. However, in case of free edges the spatial solution solves the isotropic plate equation only approximately. The hereby introduced constraints lead to slightly higher eigenfrequencies than the eigenfrequencies of the exact solution to equation 42.

A simplified approach to determine the eigenfrequencies is also based on equation 66, but does not require to solve the integrals in equation 64 and 65. Instead, approximate predetermined expressions that depend on the mode number have been computed by Warburton for all combinations of boundary conditions, that include not more than two different conditions out of free, clamped and simply supported edges. These predetermined expressions and the corresponding formulas were introduced in [7] for isotropic plates. The present document includes an extension of this approach to orthotropic plates derived by Marian Weger. Subsequently, the eigenfrequencies f_{mn} are linked to the four orthotropic rigidity constants D_1 to D_4 via

$$f_{mn} = \frac{h\pi}{2\sqrt{\rho}L_xL_y} \sqrt{D_1 G_x^4 \frac{L_y^2}{L_x^2} + D_3 G_y^4 \frac{L_x^2}{L_y^2} + D_2 H_x H_y + D_4 J_x J_y}. \quad (67)$$

A detailed derivation of this extension is part of appendix A.2. The coefficients G_x , H_x , J_x in x-dimension for the here discussed boundary conditions can be found in table 5. By substituting m with n in the table, one obtains the coefficients for G_y , H_y , J_y to the corresponding boundary conditions in y-dimension. In case of an isotropic plate equation 67 can be rewritten to

$$f_{mn} = \frac{h\pi}{2\sqrt{\rho}L_xL_y} \sqrt{D \left(G_x^4 \frac{L_y^2}{L_x^2} + G_y^4 \frac{L_x^2}{L_y^2} + 2\nu H_x H_y + 2(1 - \nu) J_x J_y \right)}, \quad (68)$$

in which D is the rigidity constant defined in equation 40. From the above equation, the second term in the square root can also be rewritten to the non-dimensional frequency factor κ with

$$\kappa^2 = G_x^4 + G_y^4 \frac{L_x^4}{L_y^4} + 2 \frac{L_x^2}{L_y^2} [\nu H_x H_y + 2(1 - \nu) J_x J_y], \quad (69)$$

Table 5 – Coefficients to determine the eigenfrequencies of a rectangular plate in single dimension for the boundary conditions (bc) free-free edges (ff), simply supported edges (ss) and clamped-free edges (cf) from [7].

bc	m	G_x	H_x	J_x
ss	2, 3, 4, ...	$m - 1$	$(m - 1)^2$	$(m - 1)^2$
ff	0	0	0	0
	1	0	0	$12/\pi^2$
	2	1.506	1.248	5.017
	3, 4, 5, ...	$m - \frac{1}{2}$	$(m - \frac{1}{2})^2 \left[1 - \frac{2}{(m - \frac{1}{2})\pi} \right]$	$(m - \frac{1}{2})^2 \left[1 + \frac{6}{(m - \frac{1}{2})\pi} \right]$
cf	1	0.597	-0.087	0.471
	2	1.494	1.347	3.284
	3, 4, 5, ...	$m - \frac{1}{2}$	$(m - \frac{1}{2})^2 \left[1 - \frac{2}{(m - \frac{1}{2})\pi} \right]$	$(m - \frac{1}{2})^2 \left[1 + \frac{2}{(m - \frac{1}{2})\pi} \right]$

if $\frac{L_y^2}{L_x^2}$ is lifted out of the parentheses. The eigenfrequencies f_{mn} depend on the material parameters of the plate, its dimensions and the boundary conditions. Exemplary eigenfrequencies of a metal plate under various boundary conditions are depicted in figure 15. As for bending waves in a bar, the eigenfrequencies increase non-linearly with increasing m if the mode number n is held constant and vice versa.

Note that this calculation method approximates the eigenfrequencies for rectangular plates and is only exact if the plate is simply supported on all edges. If free edges are involved, the mode shapes to the corresponding eigenfrequencies fulfill the boundary conditions only approximately. Furthermore, for a free plate with an aspect ratio close to one, the elastic interaction between modes with the mode numbers $\{m, n\}$ and $\{n, m\}$ leads to an additional deviation from the exact eigenfrequency. As exemplarily depicted for the mixed modes $\{2, 0\} \pm \{0, 2\}$ in figure 16, the resulting difference between Warburton's simple approach and the more accurate Rayleigh-Ritz method is not negligible, if the plate's aspect ratio is close to one. Therefore, Warburton introduced a correction factor $\Delta\kappa_{sq}$ for free square plates that changes the frequency factor κ to

$$\kappa_{sq\pm}^2 = \kappa^2 \pm \Delta\kappa_{sq}^2. \quad (70)$$

Equations to determine the correction factor are listed in appendix A.3. A comparison of the relative difference between κ and $\kappa_{sq\pm}$ for $\nu = 1/3$ in figure 16 shows a maximum relative difference of 13.5 % for $\{2, 0\} - \{0, 2\}$. However, for higher mode numbers the relative difference decreases and becomes $< 1\%$ for $m > 10$, or $n > 10$.

According to Warburton [7], the eigenfrequencies of a cantilever plate with the simple approach were up to 27 % and 12 % higher for the modes $\{1, 1\}$ and $\{2, 1\}$ than the results obtained with the Rayleigh-Ritz method. However, for both sets of boundary conditions the frequency deviations decrease with increasing mode numbers.

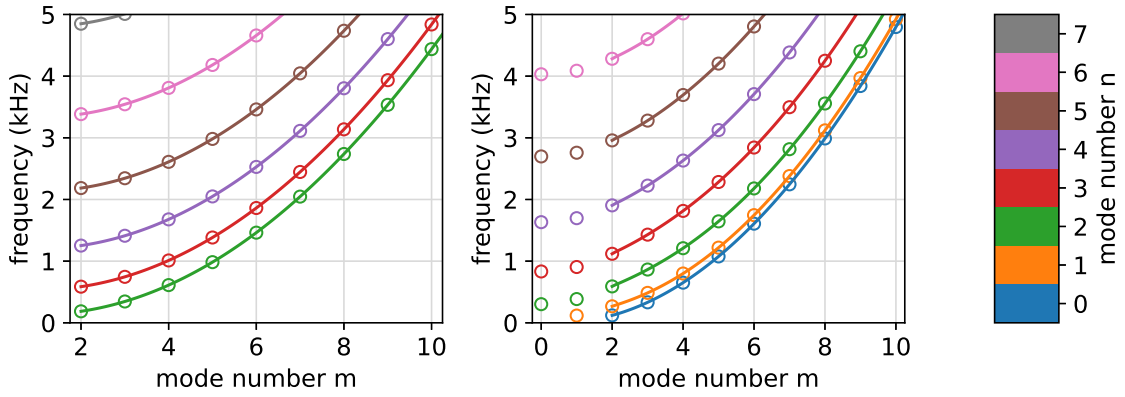


Figure 15 – Eigenfrequencies of a rectangular plate with simply supported (left) and free (right) edges. The solid curves have no physical meaning but connect modes with the same n .

Although the two introduced methods allow the determination of the eigenfrequencies of a rectangular thin plate with any combination of free, simply supported and clamped edges, the influence of the material parameters and plate dimensions on the eigenfrequencies can be presented much clearer for specific boundary conditions. This provides valuable information which may be used for the acoustic characterization of rectangular plates. For an orthotropic plate with all edges simply supported, equation 67 simplifies by inserting the coefficients from table 5 to

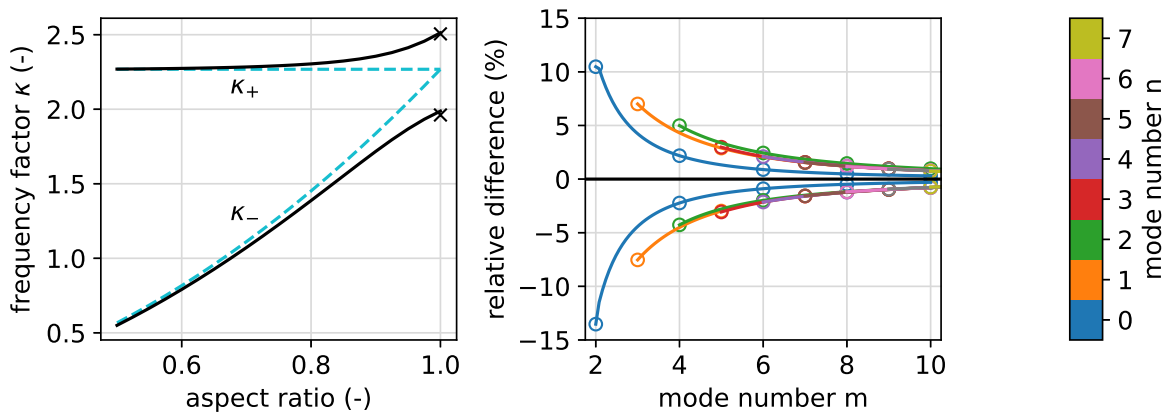


Figure 16 – Variation of the frequency factor κ (left) for the transition from rectangular to a square plate between the modes $\{2, 0\}$, $\{0, 2\}$ and the corresponding mixed modes $\{2, 0\} \pm \{0, 2\}$ if equation 69 (dashed light blue lines), the Rayleigh-Ritz method (solid black lines) in [7] is applied, and with Warburton's added square correction factor $\Delta\kappa_{sq}$ (black crosses); difference between frequency factor $\kappa_{sq\pm}$ and κ for different mode pairs for a square plate (right). The solid curves (right) have no physical meaning but connect modes with the same n .

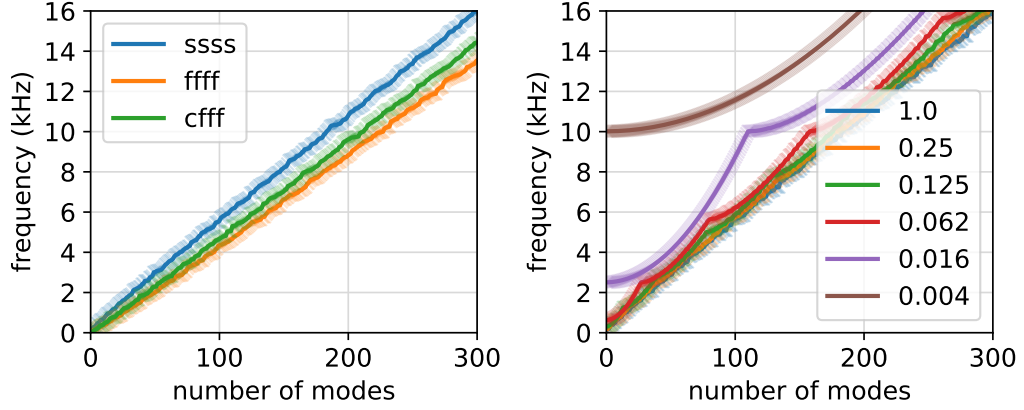


Figure 17 – Left: eigenfrequencies sorted in ascending order for a rectangular steel plate - for the boundary conditions all edges simply supported (ssss), all edges free (ffff) and one edge clamped and the rest free (cfff) with a constant aspect ratio of 0.64. Right: comparison, if the steel plate has the same boundary conditions (ssss) and the same surface area but a varying aspect ratio.

$$f_{mn} = \frac{\pi h}{2} \frac{1}{\sqrt{\rho}} \sqrt{D_1 \frac{(m-1)^4}{L_x^4} + D_3 \frac{(n-1)^4}{L_y^4} + (D_2 + D_4) \frac{(m-1)^2(n-1)^2}{L_x^2 L_y^2}}. \quad (71)$$

If the plate's material is isotropic, the formula can be further reduced to

$$f_{mn} = \frac{\pi h}{2} \sqrt{\frac{D}{\rho}} \left(\frac{(m-1)^2}{L_x^2} + \frac{(n-1)^2}{L_y^2} \right). \quad (72)$$

Typically, the modal density is frequency-independent for a rectangular plate. In case of a pure simply supported boundary condition, the modal density $D(f)$ can be estimated via

$$D(f) \approx \frac{L_x L_y}{h} \sqrt{\frac{3\rho(1-\nu^2)}{E}}, \quad (73)$$

as described in [5] p. 757. As visualized in figure 17, the resulting linear increase of the number of modes with increasing observed frequency interval is valid for all here presented boundary conditions, if the plate has an aspect ratio r_a close to one. For significantly smaller or larger r_a , the object is more bar- than plate-shaped and subsequently the modal density is no longer constant and tends to decrease with increasing mode number.

2.3 Damped Vibrations in Bars and Plates

The previous sections described free vibrations in bars and plates of various shapes and different boundary conditions. However, if these objects get excited by an impact force,

the resulting vibrations usually decay over time. The mechanical energy introduced into the system dissipates through conversion into thermal energy internally and via the radiation of sound externally. More specific, physical models of vibrations in bars [8] and plates [9] consider viscoelastic, thermoelastic, and radiation losses. While the first two damping mechanisms originate from the inherent characteristics of the object, radiation damping is caused by the coupling between the solid object and the surrounding fluid. A comprehensive overview about energy dissipation and damping in solid materials is given in [5]. This section summarizes the causes of these damping mechanisms and describes models that quantify damping.

In order to quantify the effect of damping, a so-called decay factor α is defined. Considering the transverse displacement W of a bar or plate, α describes the temporal decay according to

$$W(t)e^{-\alpha t}. \quad (74)$$

Since the decay factor is usually frequency-dependent, α becomes $\alpha(\omega)$. The time dependency in W is usually caused by an oscillating function like $\sin(\omega t + \varphi)$ that decays over time. Throughout literature, the inherent loss factor η of the material, the modal decay time T_{60} , the quality factor Q , the damping ratio ζ and the internal friction $\tan(\phi)$ are common quantities that are connected to the decay factor via

$$\eta = \frac{2\alpha}{\omega}, \quad T_{60} = \frac{\ln(10^3)}{\alpha}, \quad Q = \frac{1}{\eta}, \quad \zeta = \frac{\alpha}{\omega} \quad \text{and} \quad \tan(\phi) = \eta. \quad (75)$$

2.3.1 Damping Mechanisms in Solid Materials

Thermoelastic losses are caused by the coupling between the thermoelastic stress–strain relations and the temperature field in the solid. Thermoelastic losses are most dominant in materials with significant thermal conductivity, e.g. in metals. A practical example of this behaviour can be observed when bending a metallic bar and measuring the temperature at points at areas of high strain.

In case of orthotropic plates, small variations of the inherent temperature T are governed by the equations

$$\begin{aligned} \sigma_x &= -12z \left(D_1 \frac{\partial^2 W}{\partial x^2} + \frac{D_2}{2} \frac{\partial^2 W}{\partial y^2} \right) - \phi_x T, \\ \sigma_y &= -12z \left(D_3 \frac{\partial^2 W}{\partial y^2} + \frac{D_2}{2} \frac{\partial^2 W}{\partial x^2} \right) - \phi_y T, \\ \sigma_{xy} &= -6z D_4 \frac{\partial^2 W}{\partial x \partial y}, \end{aligned} \quad (76)$$

where σ indicates the stress, the second derivative of the transverse vibration W the strain, and ϕ the thermal material coefficient. The indices x and y represent the direction of the quantities in the corresponding plane $z = 0$. Assuming that T spatially depends only on z as depicted in figure 18, the corresponding heat diffusion equation is described by

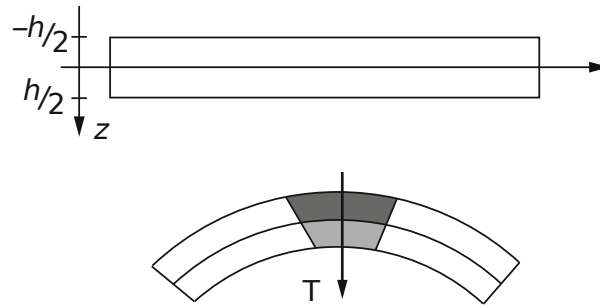


Figure 18 – Temperature distribution in a bent plate.

$$\kappa_t \frac{\partial^2 T}{\partial z^2} - \rho C_t \frac{\partial T}{\partial t} = -z T_0 \frac{\partial}{\partial t} \left(\phi_x \frac{\partial^2 W}{\partial x^2} + \phi_y \frac{\partial^2 W}{\partial y^2} \right). \quad (77)$$

Here, T_0 stands for the absolute temperature and C_t for the heat capacity at constant strain. Both equation can be used to derive a damping model for thermoelastic losses in plates. This model is described in detail in section 2.3.3.

Viscoelastic losses are caused by the viscoelasticity of a material and represent the main cause of thermal energy dissipation in materials with low thermal conductivity, such as wood, glass and carbon fibres. A viscoelastic material shows both elastic and viscous behaviour. If a material is deformed by a mechanical stress σ and the deformation is completely reversed when removing the stress, then the deformation is purely elastic. In case of a viscous deformation the strain ϵ caused by a stress is completely irreversible. Figure 19 depicts exemplary stress-strain curves for elastic and viscoelastic deformation.

The principles behind the damping of vibrations due to the radiation of sound will be described in chapter 2.5. A damping model for plates that explicitly considers radiation damping is presented in section 2.3.3.

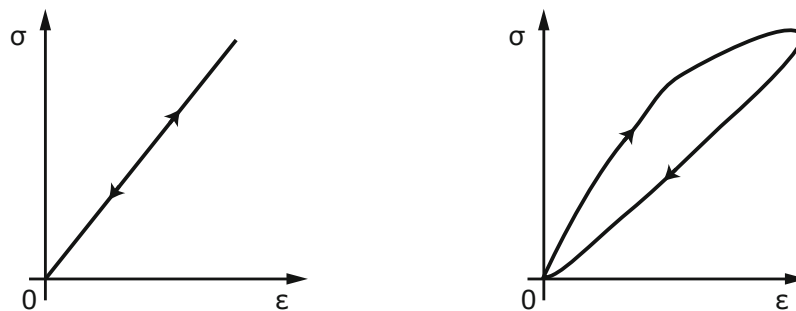


Figure 19 – Stress-strain relation for a pure elastic deformation (left) and a linear viscoelastic deformation (right).

2.3.2 Generic Damping Models and Damping Models for Bars

Throughout the literature, several models have been developed to describe the effect of damping. In [10], a damping law according to

$$\alpha(f) = \frac{\gamma}{2} + 2\pi^2\eta_v f^2, \quad (78)$$

where γ represents the fluid damping and η_v the viscoelastic damping coefficient, has been used for modelling wooden bars. In [11], the generic damping law

$$\alpha(f) = e^{\alpha_G + \alpha_R 2\pi f} \quad (79)$$

was assumed to model losses of various materials. The parameters α_G and α_R represent the losses of the intrinsic properties of the material.

2.3.3 Damping Model for Thin Plates

For plates, a comprehensive model that considers viscoelastic, thermoelastic as well as radiation losses has been presented in [9], [5] and [12]. All of those three damping mechanisms are assumed to be uncorrelated. For an orthotropic plate, the decay factor α can be determined with

$$\alpha(\omega_{mn}) = \sum_{i=1}^4 \frac{\omega_{mn}}{2} \eta_i(\omega_{mn}) J_{i,mn} + \frac{R_f}{2}, \quad (80)$$

where η represents the loss factor, J a mode shape dependent weighting, R_f a pure viscous damping, and $i = \{1, 2, 3, 4\}$ the index associated to one of the four rigidity constants \tilde{D}_i . In contrast to undamped plate vibrations that have been described in section 2.2, the rigidity constants are now complex-valued. For "small damping" the loss factors become

$$\eta_i(\omega) \approx \text{Im} \left\{ \frac{\tilde{D}_i(j\omega)}{D_i} \right\} = \text{Im} \{ \tilde{d}_i(j\omega) \} \quad (81)$$

with the pertubation term \tilde{d}_i being

$$\tilde{d}_i(j\omega) = \tilde{d}_{i,t}(j\omega) + \tilde{d}_{i,v}(j\omega) + \tilde{d}_r(j\omega). \quad (82)$$

The index t in the above equation indicates the intrinsic thermoelastic losses, which can be derived from the equations that govern the vibrations of an orthotropic plate and the heat diffusion equation (equation 76 and 77). Assuming no heat transfer between the plate and the surrounding air and a spatial temperature distribution of

$$T(z) = T_0 \sin \left(\frac{\pi z}{h} \right), \quad (83)$$

the resulting pertubation term $\tilde{d}_{i,t}$ can be determined with

$$d_{i,t}(j\omega) = \begin{cases} \frac{j\omega R_{i,t}}{j\omega + c_1/h^2}, & i = 1, 2, 3 \\ 0, & i = 4, \end{cases} \quad (84)$$

where $R_{i,t}$ is

$$R_{1,t} = \frac{8T_0\phi_x^2}{\pi^4 D_1 \rho C_t}, \quad R_{2,t} = \frac{16T_0\phi_x\phi_y}{\pi^4 D_3 \rho C_t}, \quad R_{3,t} = \frac{8T_0\phi_y^2}{\pi^4 D_3 \rho C_t}. \quad (85)$$

The dependency of $\tilde{d}_{i,t}$ on h^2 indicate that the thermoelastic losses decrease with increasing thickness of the plate. Furthermore, the damping caused by thermoelastic losses depends on the mode shape - the corresponding weighting factor $J_{i,mn}$ will be described later in this section. For an isotropic plate, the thermal material coefficients are independent of the direction and $\phi_x = \phi_y = \phi$. In addition, the thermal material coefficient is related to the thermal expansion coefficient α_t of a material by

$$\phi = \alpha_t \frac{E}{1 - 2\nu}. \quad (86)$$

The factor c_1 is connected to the thermoelastic relaxation factor τ_t via

$$\frac{c_1}{h^2} = \frac{1}{\tau_t}, \quad \tau_t = \frac{\rho C_t h^2}{\kappa_t \pi^2}, \quad (87)$$

in which κ_t is the thermal conductivity of the material. Typical thermal constants from various materials can be found in [5] and are listed in table 6. In [9], the coefficients c_1 and R_1 were obtained by fitting the model to measured decay factors.

The viscoelastic losses are considered in the perturbation term $\tilde{d}_{i,v}$ and represent the main cause of thermal energy dissipation in materials with low thermal conductivity. Viscoelastic properties combine both aspects of elastic and viscous deformation of materials. For the present damping model, the viscoelastic phenomenon is modelled using a generalized dissipative Maxwell model of the order $N = 2$ of the form

$$\tilde{d}_{i,v}(j\omega) = \frac{j\omega R_{i1,v}}{j\omega + s_{i1,v}} + \frac{j\omega R_{i2,v}}{j\omega + s_{i2,v}}. \quad (88)$$

In [9], values for the damping coefficients $R_{i1,v}$, $R_{i2,v}$, $s_{i1,v}$ and $s_{i2,v}$ have been determined for various materials from measurements. The results are listed in table 7.

For both the thermoelastic and the viscoelastic losses, it can be necessary to introduce a pure viscous damping term R_f to prevent decay factors close to zero for low frequencies. Reasonable values determined for various materials by fitting them to achieve the measured decay times are listed in table 8.

Table 6 – Thermal constants heat capacity C_t , thermal expansion coefficient α_t and thermal conductivity κ_t for typical materials from [5] p. 223.

	wood	steel	glass	aluminium
C_t (J / kg °C)	2000	460 - 625	700	900
α_t (10^{-6} / K)	4	14	6 - 10	22
κ_t (W / m K)	0.04 - 0.4	11 - 46	1.1	105 - 250

Table 7 – Viscoelastic parameters measured in [9]. The row number in each value matrix indicates the index n of the dissipative Maxwell model, the row number the index i (if available).

	wood	glass	carbon fibres
$R_{in,v} (\times 10^{-3})$	$\begin{bmatrix} 8.18 & 0 & 16.7 & 15.2 \\ 10 & 0 & 70 & 35 \end{bmatrix}$	$\begin{bmatrix} 1.63 \\ 1.962 \end{bmatrix}$	$\begin{bmatrix} 1.32 & 0 & 8.8 & 10.4 \\ 5 & 0 & 44 & 14.4 \end{bmatrix}$
$s_{in,v} (\times 10^3 \text{ rad s}^{-1})$	$\begin{bmatrix} 3.2 & 0 & 1.1 & 1.75 \\ 50.2 & 0 & 0.0502 & 50.2 \end{bmatrix}$	$\begin{bmatrix} 5.18 \\ 55.1 \end{bmatrix}$	$\begin{bmatrix} 10.1 & 0 & 2.5 & 2.27 \\ 94 & 0 & 0.07 & 40 \end{bmatrix}$

Besides the internal damping mechanisms, the plate model also considers the interaction between the vibrating plate and the surrounding air. The so-called radiation damping was derived in [9] for an isotropic infinite plate. By applying a Padé development of the order three, the radiation perturbation term \tilde{d}_r can be determined with

$$\tilde{d}_r(j\omega) = \frac{2\rho_{air}c \sum_{M=1}^3 b_M (j\omega/\omega_c)^M}{\omega_c \rho h \sum_{N=0}^3 a_N (j\omega/\omega_c)^N}, \quad (89)$$

in which ω_c is the critical angular frequency of the plate, and $a_0 = 1.1669$, $a_1 = 1.6574$, $a_2 = 1.5528$, $a_3 = 1$ and $b_1 = 0.062$, $b_2 = 0.595$, $b_3 = 1.0272$. Note that the above equation approximates only the radiation perturbation of an isotropic plate.

The weighting factors $J_{i,mn}$ in the damping model depend primarily on the spatial mode shape $\Theta_{mn}(x, y)$, abbreviated by Θ in this section. In

$$J_{i,mn} = \frac{\langle \Theta, \Theta \rangle_i}{\omega_{mn}^2 \|\Theta\|^2}, \quad (90)$$

the scalar products $\langle \Theta, \Theta \rangle_i$ are defined as

$$\begin{aligned} \langle \Theta, \Theta \rangle_1 &= \int_S h^3 D_1 \left(\frac{\partial^2 \Theta}{\partial x^2} \right)^2 dS, \\ \langle \Theta, \Theta \rangle_2 &= \int_S h^3 D_2 \frac{\partial^2 \Theta}{\partial x^2} \frac{\partial^2 \Theta}{\partial y^2} dS, \\ \langle \Theta, \Theta \rangle_3 &= \int_S h^3 D_3 \left(\frac{\partial^2 \Theta}{\partial y^2} \right)^2 dS, \\ \langle \Theta, \Theta \rangle_4 &= \int_S h^3 D_4 \left(\frac{\partial^2 \Theta}{\partial x \partial y} \right)^2 dS, \end{aligned} \quad (91)$$

and the squared norm is given by

Table 8 – Viscous constants for typical materials from [9].

	wood	glass	aluminium	carbon
$R_f (\text{s}^{-1})$	2.4	0.88	0.032	0.8

$$\|\Theta\|^2 = \int_S \rho h \Theta^2 dS. \quad (92)$$

The above equations indicate that the scalar products depend on the curvature of the mode shapes. This means the resulting decay factor can vary from mode to mode substantially, as shown later. Furthermore, the weighting factors $J_{i,mn}$ lead to a decay factor that depends on the boundary condition of the plate. Since the $J_{i,mn}$ for a specific mode indicate the partitioning of the potential energy,

$$J_{1,mn} + J_{2,mn} + J_{3,mn} + J_{4,mn} = 1 \quad (93)$$

must be true.

Besides the damping due to sound radiation, all aspects of the described damping model are intended for orthotropic plates. In case of an isotropic plate, the damping model can be simplified to

$$\alpha(\omega_{mn}) = \frac{\omega_{mn}}{2} [\eta_1(\omega_{mn})I_{1,mn} + \eta_4(\omega_{mn})I_{4,mn}] + \frac{R_f}{2}, \quad (94)$$

with $I_{1,mn}$ and $I_{4,mn}$ given by

$$I_{1,mn} = J_{1,mn} + J_{3,mn} + \frac{2D_1}{D_2}J_{2,mn}, \quad I_{4,mn} = J_{4,mn} - \frac{D_4}{D_1}J_{2,mn}. \quad (95)$$

In order to illustrate the influence of the different damping mechanisms of the plate damping model, a free isotropic aluminium plate is assumed as a first example. For metallic plates the measurements carried out in [9] indicate that the damping primarily depends on the thermoelastic losses and radiation damping. Considering these two damping mechanisms and the isotropic behaviour of the plate, the perturbation terms \tilde{d}_1 and \tilde{d}_4 only depend on

$$\tilde{d}_1(j\omega) = \tilde{d}_{1,t}(j\omega) + \tilde{d}_r(j\omega), \quad \tilde{d}_4(j\omega) = \tilde{d}_r(j\omega). \quad (96)$$

Inserting the terms in equation 94, one obtains

$$\alpha(\omega_{mn}) = \frac{\omega_{mn}}{2} \text{Im}\{\tilde{d}_{1,t}(j\omega)I_{1,mn} + \tilde{d}_r(j\omega)\} + \frac{R_f}{2}, \quad (97)$$

for the damping law of an isotropic metallic plate. The resulting decay factor of an exemplary aluminium plate in figure 20 shows, that the damping is characterized by the radiation damping for frequencies within the range around and above the critical radiation frequency f_{crit} of the plate. For lower frequencies the radiation damping decreases and the thermoelastic losses become the dominant factor. Note that the apparent randomness of the decay factors is introduced by $I_{1,mn}$, which includes the mode shape dependent weighting factors $J_{i,mn}$.

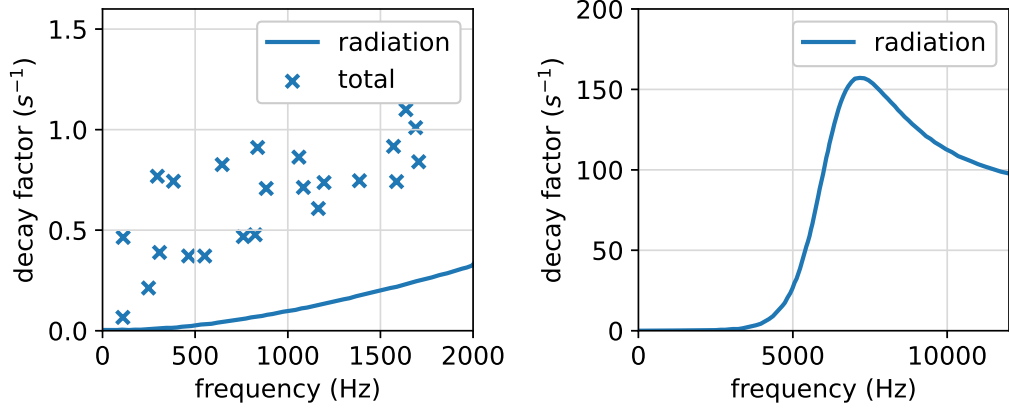


Figure 20 – Predicted decay factors of a free isotropic aluminium plate from [9].

As a second example, a free isotropic glass plate is assumed. In this case measurements in [9] confirmed that there is an almost linear relationship between ω_{mn} and α below the critical frequency of the plate where inherent damping mechanisms dominate. Hence, the decay factor can be assumed to be independent of the mode shape. Analogous to the aluminium plate example, the perturbation terms simplify to

$$\tilde{d}_1(j\omega) = \tilde{d}_{1,v}(j\omega) + \tilde{d}_r(j\omega), \quad \tilde{d}_4(j\omega) = \tilde{d}_r(j\omega), \quad (98)$$

and the inherent viscoelastic losses are now considered. For the total decay factor,

$$\alpha(\omega_{mn}) = \frac{\omega_{mn}}{2} \text{Im}\{\tilde{d}_{1,v}(j\omega) + \tilde{d}_r(j\omega)\} + \frac{R_f}{2}, \quad (99)$$

is obtained. As shown in figure 21, the damping law of an exemplary glass plate shows an almost linear relationship between decay factors and the eigenfrequencies below 3 kHz. the same behaviour as the aluminium plate. However, the inherent viscoelastic losses for glass lead to significantly higher decay factors as the thermoelastic losses in aluminium for plates with a comparable size.

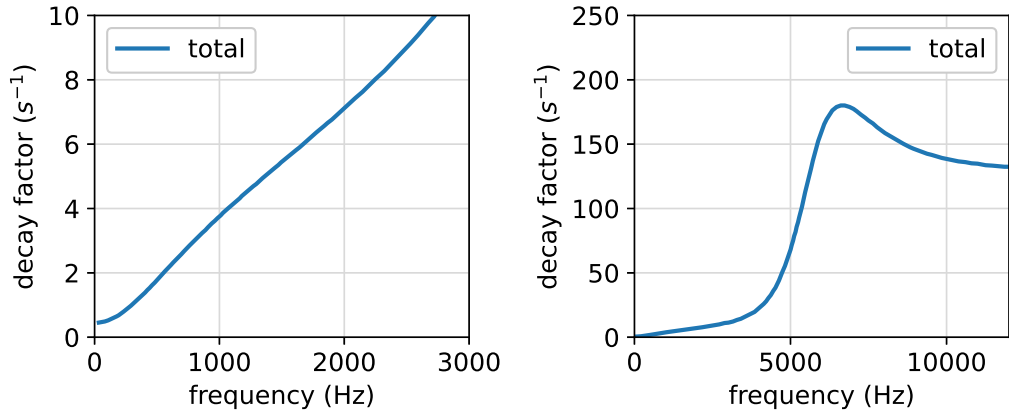


Figure 21 – Damping law of a free isotropic glass plate from [9].

2.4 Mechanical Excitation of Objects

So far, forced vibrations of various objects have been described without specifically considering the excitation that causes the vibrations. The process of identifying an object acoustically starts with a mechanic excitation, such as tapping. Therefore, this section is devoted to the description of the mechanical excitation of simple objects.

2.4.1 Hertz's Theory of Contact

It is known that the interaction force from an object that impacts on a structure results from the elastic deformation of both solids in contact. In studies such as [8] and [9], Hertz's law of contact is used to model this transient excitation on bars and plates.

For the following considerations, it is assumed that the impactor is a sphere with a radius much smaller than the struck object. The interaction force $F(t)$ between the impactor and a struck object is governed by the nonlinear relation

$$F(t) = K|U(t) - W(t)|^{3/2}, \quad (100)$$

with W being the displacement of the object at the impact point and U the displacement of the impactor. In figure 22, the contact between the objects is visualized under the assumption that $|U(t) - W(t)|$ deforms only the sphere. The motion of the impactor is given by Newton's second law

$$M_e \frac{d^2U}{dt^2} = -F(t) \quad \text{with} \quad \frac{dU(0)}{dt} = V_0, \quad (101)$$

where V_0 represents the initial velocity of the sphere at the time of impact. If the impactor is a head of a mallet that is held by a person, the effective M_e is slightly larger than the actual mass of the mallets head. This is due to the stick that is held by the persons hand. Note that the above equations neglect any vibrations in the impactor and assume that the surface of the struck object remains constant during the impact. With

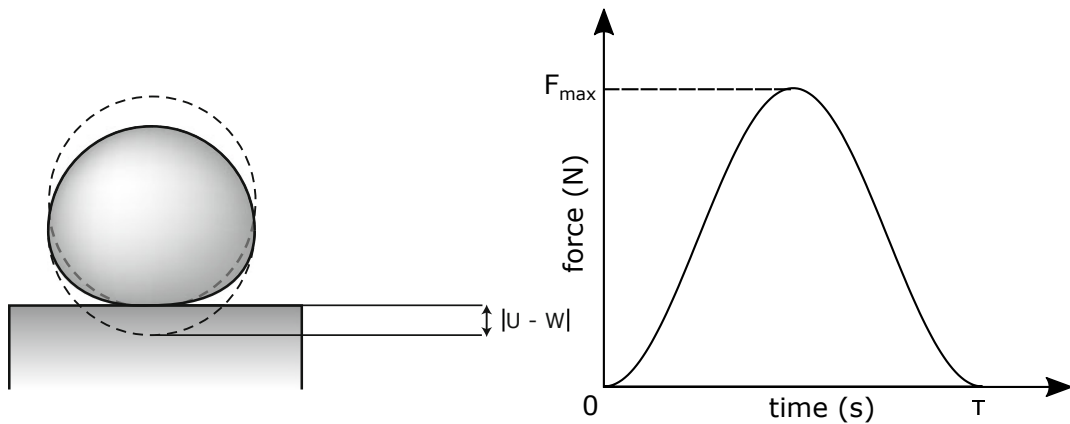


Figure 22 – Contact of a sphere with an infinite rigid plane (left) and resulting interaction force modelled with a Hanning window (right).

the material properties of both the impactor and the struck object known, the stiffness coefficient K can be calculated with

$$K = \frac{\sqrt{R_I}}{D_H}, \quad (102)$$

where D_H is

$$D_H = \frac{3}{4} \left(\frac{1 - \nu^2}{E} + \frac{1 - \nu_I^2}{E_I} \right). \quad (103)$$

The quantities R_I , ν_I and E_I stand for the radius, Poisson's ratio and Young's modulus of the impactor. Analogous, ν and E represent the material parameters of the struck object. As derived in [8], the interaction time τ_H between the two solids can be determined with

$$\tau_H = 3.218 \left(\frac{\mu^2}{K^2 V_0} \right)^{1/5} \quad (104)$$

based on the conservation of mechanical energy. The maximum interaction force F_{max} and the radius of the maximum contact area $r_{H,max}$ are

$$F_{max} = \frac{\mu^3}{\left(\frac{K \tau_H^3}{35.4} \right)^2}, \quad r_{H,max} = \sqrt{\left(\frac{5\mu}{4K} \right)^{2/5} V_0^{4/5} R_I}, \quad (105)$$

with μ being the reduced mass

$$\mu = \frac{M_I M}{M_I + M} \quad (106)$$

between the mass M_I of the impactor and the mass M of the struck object. Figure 22 shows the shape of the resulting interaction force $F(t)$, if τ_H and F_{max} are used with a Hanning window. In order to determine $F(t)$, the material properties of the impactor as well as of the struck object and the impact speed V_0 must be known. Furthermore, it is interesting that the interaction time depends hardly on the impact speed. Note that during the interaction process, the contact area r_H varies with time. However, the study in [8] indicates that a constant contact area does not lead to significant differences in the vibrational behaviour, except when the contact area is situated near an antinode. Therefore, a commonly applied method comprises a spatial weighting window that accounts for the distribution of the force over a constant contact area, weighted with a temporal window.

2.5 Sound Radiation

If the vibrational behaviour of an object is known, the sound radiation into a surrounding fluid can be calculated. In this section selected aspects of sound radiation from vibrating objects will be described.

Note that the presented methods do not aim to describe the radiated sound in the most comprehensive way, but with a degree of complexity so that they can be incorporated in

an efficient modal synthesis model. The application of equations such as the Kirchhoff-Helmholtz integral would require numerical simulation methods like the boundary element method (BEM). However, a comprehensive discussion on sound radiation that considers these aspects can be found in many books, such as [5], [13] and [14].

2.5.1 Elementary Radiators

The simplest radiator archetype is an omnidirectional source represented by a pulsating sphere. As a basic solution of the wave equation in spherical coordinates, the complex sound pressure \tilde{p} of the wave radiated by the source is

$$\tilde{p} = \frac{A}{r} e^{-jkr} e^{j\omega t}. \quad (107)$$

The sound particle velocity is given by

$$\tilde{v} = \frac{A}{\rho_{air} c_{air}} \left(\frac{1}{r} - \frac{j}{kr^2} \right) e^{-jkr} e^{j\omega t}. \quad (108)$$

The second term in the parentheses of the above equation becomes relevant for $kr < 1$ and is responsible for the reactive sound power in the vicinity of the radiator. Under the condition $kr \gg 1$, the phase difference between \tilde{p} and \tilde{v} tends to zero and the pulsating sphere can be replaced by a point source. Both quantities decrease with $1/r$ in this case.

If the radiated sound field of two omnidirectional sources with the same strength but opposite phase is superimposed, the sound field of a dipole source is obtained. A vibrating plane can be described as a dipole for sufficiently low frequencies. As shown in figure 23, the distance between the two monopole sources is given by L . By superimposing the sound fields of both sources that radiate with the same frequency, one gets

$$\tilde{p} = \left(\frac{A}{r_1} e^{-jkr_1} - \frac{A}{r_2} e^{-jkr_2} \right) e^{j\omega t}, \quad (109)$$

where r_1 and r_2 represent the distances from the monopoles to the observation point. Depending on the location of the observation point and the relation L/λ , a constructive or destructive interference occurs for the resulting pressure \tilde{p} . In the far field around the dipole where $r_1 \gg L$ and $r_2 \gg L$, the distances r_1 and r_2 can be approximated to be equal with regards to amplitude in equation 109. The phase terms on the other hand must be handled separately since they determine if the interference is constructive or de-

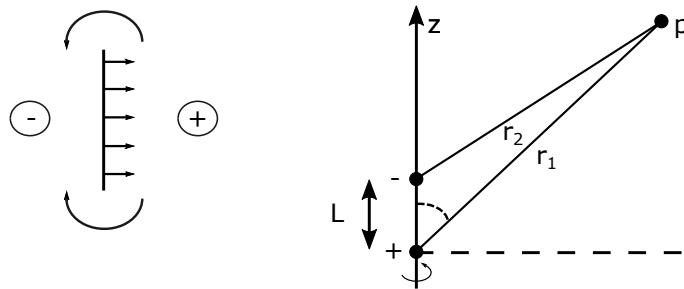


Figure 23 – Conphase vibrating plane described with two monopole sources (left) and corresponding geometric setup (right).

-structive. As derived in [14] p. 88, this leads to

$$\tilde{p} \approx \left(\frac{A}{r_1} - \frac{A}{r_2} e^{-jkL \cos(\vartheta)} \right) e^{j\omega t} \quad (110)$$

as approximation for the sound pressure in the far field. By determining the radiated sound power P in the far field the dipole can be characterized independent of the observation point. After the spatial integration of the sound pressure one gets

$$P = P_1 \left(1 + \left(\frac{A_2}{A_1} \right)^2 + 2 \frac{A_2}{A_1} \frac{\sin(kL)}{kL} \right). \quad (111)$$

As third elementary radiator, the sound radiation of an infinite plate is discussed. For this purpose, a plate depicted in figure 24 and extended to an infinite size along the x- and the y-axis is assumed.

The critical frequency or coincidence frequency f_{crit} of a plate represents the frequency, at which the wavelength of the bending wave λ_B equals the wavelength of the radiated sound wave λ_{air} . According to [15], it is given by

$$f_{crit} = \frac{c_{air}^2}{2\pi} \sqrt{\frac{12\rho(1-\nu^2)}{Eh^2}}. \quad (112)$$

In case of an infinite plate, free bending waves lead to sound radiation only above f_{crit} . Below the coincidence frequency, $\lambda_{air} > \lambda_B$ and an exponentially decaying near field is formed. The larger λ_{air} becomes in comparison to λ_B the faster the sound pressure decays with increasing distance from the plate. The decaying near field is caused by the compensation of pressure areas of the opposite phase in the vicinity of the plate, as shown schematically in figure 25. In terms of the radiation damping used in the plate damping model in section 2.3.3, the radiation damping is low below f_{crit} . Above the critical frequency, bending waves lead to a sound radiation into the far field which corresponds to a high radiation damping.

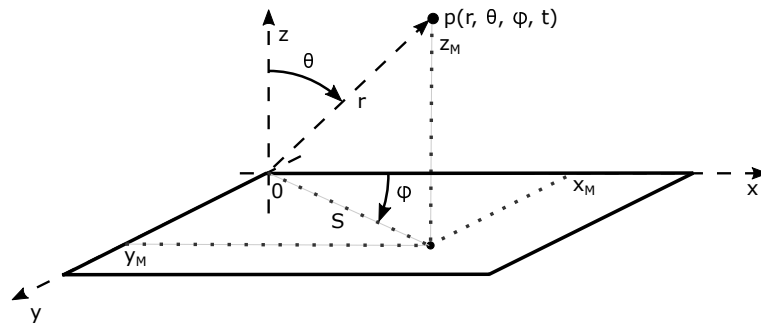


Figure 24 – Vibrating plate with the area S in an infinite baffle in the plane $z = 0$ and sound pressure p evaluated at a large distance r (not to scale).

2.5.2 Plane, Baffled Radiators

Considering the baffled radiator with the surface S as shown in figure 24, the sound pressure p at a point $\{x_M, y_M, z_M\}$ in the infinite half space can be determined with

$$p(r, \theta, \varphi, t) = \frac{\rho_{air}}{2\pi} \int_S \frac{\partial^2 W(x, y, t - d/c_{air})}{\partial t^2} \frac{1}{d} dS. \quad (113)$$

with $d = \sqrt{(x - x_M)^2 + (y - y_M)^2 + z_M^2}$. Known as Rayleigh's integral, the above equation can be solved analytically only for special cases. Therefore, a frequently used approach discretizes the radiator into small surface elements with point sources at their centres. The sound pressure p is then determined by summing the contribution of all point sources, whereas the term $t - d/c_{air}$ accounts for the appropriate time delay to the point $\{x_M, y_M, z_M\}$.

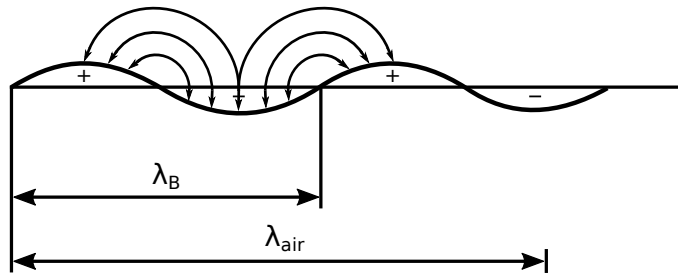


Figure 25 – Acoustic shortcut for $\lambda_{air} > \lambda_B$ for a 1-dimensional bending wave.

2.6 Psychoacoustics of Bars and Plates

The acoustic identification and perception of solid objects - in various literature sources also referred to as psychomechanics, auditive kinetics or ecological acoustics [16] - provides vital information about a surrounding environment in everyday life. The radiated sound created by tapping, knocking or scratching an object often enables a distinction between different objects. A vivid example for this would be the distinction between the sounds of a knocked wooden furniture plate and a desk glass plate, whereas the sound of the latter usually contains a larger number of longer decaying partials.

Systematic research on the acoustic classification and basic object identification was already conducted in various studies. In [16] and [15] the effect of size and material properties on the identification of plates was investigated. Furthermore, the authors of the first study introduced a description of a physical object on three different levels: in terms of physical or mechanical properties of the object as a sound source, on the acoustic level considering characteristics of the emitted sound, and on a perceptual basis of the recognized sound event. Listening tests in [17] and [10] with synthesized sounds of struck bars as well as with synthesized plate sounds in [15] identified the material-inherent loss factor η as a main correlating parameter with the listeners ability to distinguish between certain material groups. Being directly connected to the decay time T_{60} and the decay factor α , η characterizes the decay behaviour of the emitted sound of an impacted

object. While in [16] listening experiment participants could clearly identify the material classes steel-glass and wood-plexiglass of impacted plates, separating materials within each group was ambiguous. Besides the decay behaviour as an important cue for the acoustic identification of materials, participant material dissimilarity ratings in [15] and material identification decisions in [17] showed a correlation with the perceived pitch of the sound, which can be attributed to the wave velocity within the material. However, direct acoustic material identification results in [16] showed that participants mostly ignored the pitch information.

With respect to the development of an acoustic characterization method for rectangular plates within this work, it can be summarized that the average auditory system of humans is able to identify and distinguish coarse material groups like metal-glass or wood-plexiglass from the sound of an impacted plate or bar. Furthermore, the studies mentioned in this section consistently highlight the correlation between the inherent damping properties of a material and the results from the conducted listening experiments in these studies.

3 Modal Synthesis of Rectangular Plates

Within this project, a modal synthesis model to simulate the emitted sound of rectangular plates has been implemented. Like all physical modelling techniques, modal synthesis aims to create a sound based on the physics responsible for the sound production. For the excitation of vibrations in thin bars and rectangular plates, corresponding models have been described in chapter 2. If sound radiation is also taken into account, the basic steps involved in the physical model can be summarized as in figure 26. An excitation signal such as caused by Hertz's law of contact serves as input signal to the model. Furthermore, the behaviour of the model can be controlled with the material properties and the dimensions of the physical object.

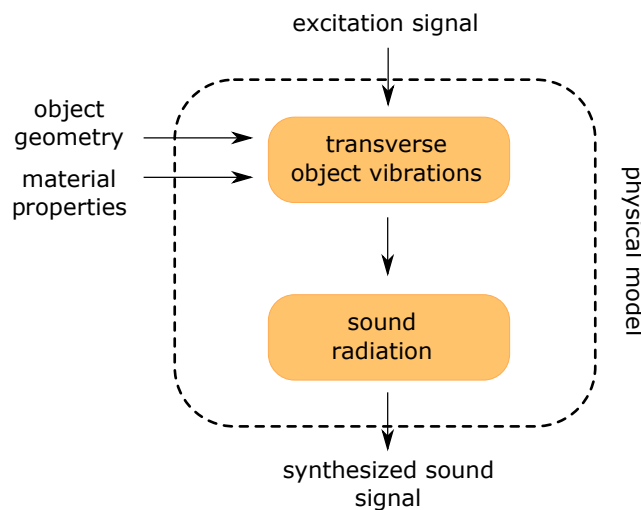


Figure 26 – Steps involved in the implemented physical sound synthesis model.

In modal synthesis, the vibration of an object consists of weighted contributions of modes with their associated eigenfrequencies. Under the assumption that the modes are independent to each other, each mode can be represented by a single damped mass-spring system. Therefore, in the next section this basic mechanical system and its important characteristics for the synthesis model will be recapitulated. Subsequently, the selected physical synthesis model from the literature for this work is explained. In the third part of this chapter the implementation of the selected modal synthesis model and its extensions are described. The last section deals with the model validation using results from various literature sources and real sounds of impacted plates.

3.1 Modal Synthesis Model

3.1.1 Damped Mass-Spring System

A simple damped mass-spring system is governed by the equation

$$M \frac{\partial^2 W}{\partial t^2} + R \frac{\partial W}{\partial t} + KW = F(t) \quad (114)$$

and characterized by the mass M , the mechanical resistance R and the spring constant K . If the external force $F(t)$ is a Dirac impulse $\delta(t - t_0)$, then the impulse response of the system is

$$h(t - t_0) = \frac{1}{M\omega_d} \sin[\omega_d(t - t_0)] e^{-\zeta\omega_0(t-t_0)}, \quad (115)$$

where ζ is the damping ratio defined by

$$\zeta = \frac{R}{2M\omega_0}. \quad (116)$$

The resonance frequency ω_d is slightly lower than the resonance frequency ω_0 of the undamped system:

$$\omega_d = \omega_0 \sqrt{1 - \zeta^2}, \quad \omega_0 = \sqrt{\frac{K}{M}} \quad (117)$$

The impulse response $h(t)$ can be used to determine the displacement $W(t)$ to an arbitrary external force by convolving $F(t)$ with $h(t)$. The transfer function $H(s)$ of the system is given by

$$H(s) = \frac{1}{M} \frac{1}{s^2 + s(2\zeta\omega_0) + \zeta^2\omega_0^2 + \omega_d^2}. \quad (118)$$

In figure 27 the corresponding magnitude response shows that for ζ close to 1 the high damping prevents the resonance peak at ω_d and leads to characteristics of a second-

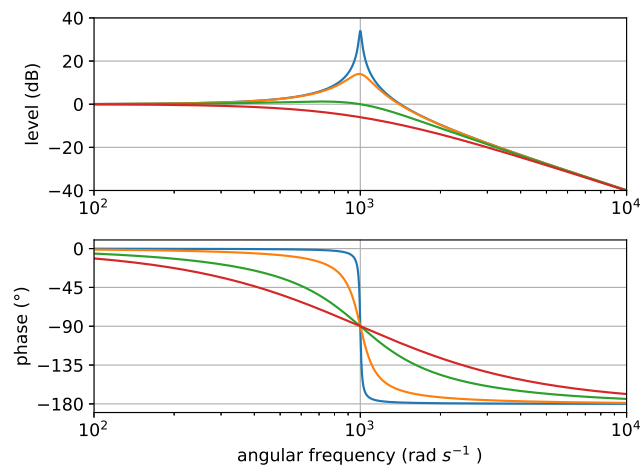


Figure 27 – Magnitude response (top) and phase response (bottom) of a damped mass-spring system for the damping ratios 1 (red), 0.5 (green), 0.1 (orange) and 0.01 (blue).

order Butterworth filter. With damping ratios $\ll 1$, a pronounced resonance peak appears that becomes larger and narrower with lower damping ratios. From the modal synthesis perspective, a mode with high damping possesses a broad spectrum due to the fast decay of the sine wave. The energy of the resulting broadband spectrum is distributed over a large interval around the resonance frequency. In extreme cases the fast decay leads to a pulse-shaped impulse response, which sounds like a click. In case of low damping, the impulse response becomes long and the spectrum has a narrow band around the resonance frequency. Hence, the modal impulse response sounds like a sinusoid that decreases in volume over time. Both scenarios of fast and slow decaying modes occur in the synthesis model from Troccaz [18], which is summarized in the next section.

3.1.2 Simulation of Damped Impacted Plates

In [18], Troccaz presented a model to determine the sound radiation of a thin rectangular plate based on a geometric setup depicted in figure 28. Hereby, the impact of a sphere causes a force F that acts at a point of the plate with the size L_x , L_y and the thickness h . The vibrations on the plate are governed by the inhomogeneous plate equation

$$h\rho\frac{\partial^2 W}{\partial t^2} + h^3 D \nabla^4 W + C \frac{\partial W}{\partial t} = F. \quad (119)$$

The rigidity constant D is

$$D = \frac{E}{12(1 - \nu^2)} \quad (120)$$

and C represents the damping coefficient. By applying the method of separation of variables on the plate equation, the solution is split up into a spatial part and a temporal part. For a rectangular plate, the solution for a single mode $\{m, n\}$ becomes

$$W_{mn}(x, y, t) = \frac{1}{\rho h} Z_{mn}(x, y) W_{mn}(t). \quad (121)$$

The spatial part of the solution

$$Z_{mn}(x, y) = A_{mn} \Theta_{mn}(x, y) \Theta_{mn}(x_0, y_0) \quad (122)$$

is characterized by the mode shapes Θ_{mn} of the plate for a specific boundary condition and the evaluation of the modes at the impact point $\{x_0, y_0\}$ of the force F . Suitable mode shapes and their corresponding eigenfrequencies have been described in section 2.2 and [7]. The factor A_{mn} ensures that $\int \int \Theta_{mn}^2 dx dy = 1$. For a plate simply supported on all edges, $A_{mn} = \frac{4}{L_x L_y}$. The temporal part

$$W_{mn}(t) = \frac{1}{\omega_{d,mn}} \int_0^t F(\tau) e^{-\zeta \omega_{mn}(t-\tau)} \sin[\omega_{d,mn}(t-\tau)] d\tau \quad (123)$$

convolves the point force with an exponentially decaying sinusoid. Considering the factor $1/(\rho h L_x L_y)$ in equation 121, the temporal part can be interpreted as the convolution of the excitation force with the impulse response of a damped mass-spring system, as

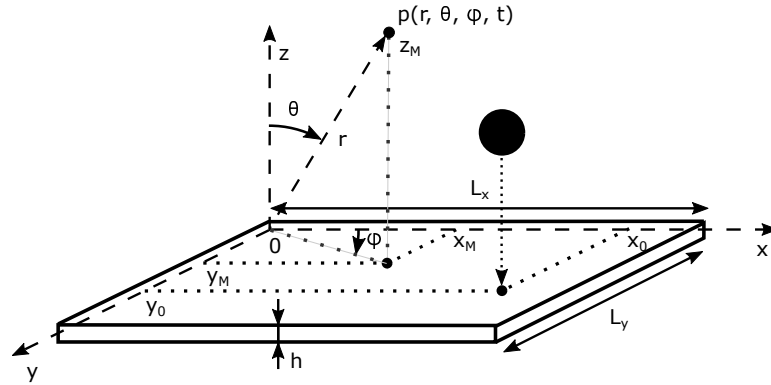


Figure 28 – Geometric setup of the Troccaz synthesis model and the implemented modal synthesis model.

denoted in section 3.1.1. Each eigenfunction of the plate adds a damped mass-spring system with the diminished angular eigenfrequency $\omega_{d,mn}$ to the overall vibration, which becomes

$$W(x, y, t) = \frac{1}{\rho h} \sum_{n=0}^{\infty} \sum_{m=0}^{\infty} Z_{mn}(x, y) W_{mn}(t). \quad (124)$$

The point force $F(t)$ caused by the impact of a sphere on the plate is determined by an extended version of Hertz's law that accounts also for plastic deformations. In the first part of the contact period between the sphere and the plate, purely elastic deformation occurs as described in section 2.4.1. The second phase is governed by a purely plastic deformation, followed a mixed deformation that models the deformation during the rebound. In order to model the sound radiation of the baffled plate, Rayleigh's integral is applied as described in equation 113.

3.2 Implemented Model

In this work, an adapted version of the synthesis model presented in [18] that utilizes the comprehensive plate damping law in [9] has been implemented. Hence, the geometric setup and the plate properties are the same as described in section 3.1.2. Furthermore, the model has been extended to synthesize the transverse vibrations in orthotropic plates with any combination of free, simply supported or clamped edges. An overview about the steps involved in the synthesis model is depicted in figure 29. By default, the modes shapes and their corresponding eigenfrequencies are determined internally based on material properties, object dimensions and boundary conditions. However, it is also possible to provide the mode shapes and eigenfrequencies externally. This possibility was exploited throughout the validation of the synthesis model, where the results from finite element method (FEM) simulations were partly used as a reference. The model outputs synthesized sound pressure signals over time.

In order to conveniently incorporate the plate damping law into the model, equation 119

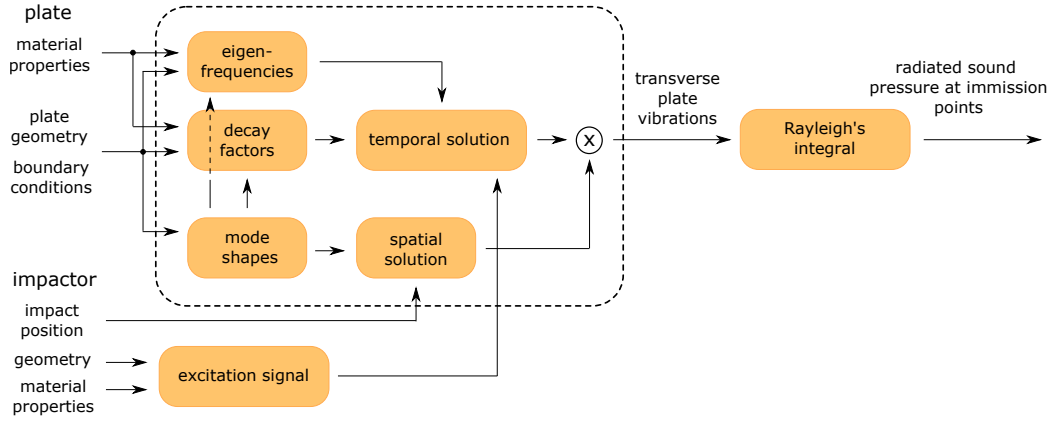


Figure 29 – Steps involved in the implemented physical sound synthesis model.

is written in the temporal Laplace domain and extended for orthotropic plates to

$$\frac{\rho}{h^2} s^2 \tilde{W} + \tilde{D}_1 \frac{\partial^4 \tilde{W}}{\partial x^4} + \tilde{D}_3 \frac{\partial^4 \tilde{W}}{\partial y^4} + (\tilde{D}_2 + \tilde{D}_4) \frac{\partial^4 \tilde{W}}{\partial x^2 \partial y^2} + R_f s \tilde{W} = \tilde{F}. \quad (125)$$

The complex displacement $\tilde{W} = \tilde{W}(x, y, s)$ and the impact force $\tilde{F} = \tilde{F}(s)$ depend now on the complex frequency variable $s = \sigma + j\omega$. Furthermore, the rigidity constants \tilde{D}_1 to \tilde{D}_4 are complex and related to the perturbation terms as described in section 2.3.3. Note that the above bending wave equation is written in the temporal Laplace domain for a more compact notation - the actual model synthesizes a sound in the time domain. In analogy to the solution in equation 121, the transverse displacement of a plate mode can be written as

$$\tilde{W}_{mn}(x, y, s) = \frac{1}{\rho h} Z_{mn}(x, y) \tilde{W}_{mn}(s), \quad (126)$$

with

$$Z(x, y) = \Theta_{mn}(x, y) \Theta_{mn}(x_0, y_0) \quad (127)$$

and

$$\tilde{W}_{mn}(s) = \tilde{F}(s) \mathcal{L} \left\{ \frac{1}{\omega_{mn}} e^{-\alpha_{mn} t} \sin(\omega_{mn} t) \right\} = \tilde{F}(s) \tilde{H}_{mn}(s), \quad (128)$$

where \mathcal{L} represents the Laplace transform. The influence of the complex rigidity constants in the plate equation is taken into account by the decay factor α_{mn} , which is determined according to

$$\alpha(\omega_{mn}) = \sum_{i=1}^4 \frac{\omega_{mn}}{2} \eta_i(\omega_{mn}) J_{i,mn} + \frac{R_f}{2}. \quad (129)$$

A description of the loss factors η_i , their corresponding weighting factors $J_{i,mn}$, and the theory behind the damping law can be found in section 2.3.3. $\tilde{H}_{mn}(s)$ is given by

$$\tilde{H}_{mn}(s) = \frac{1}{s^2 + s(2\alpha_{mn}) + \alpha_{mn}^2 + \omega_{mn}^2}. \quad (130)$$

Note that contrary to the damping applied by Troccaz the eigenfrequencies are not diminished due to the modal damping characteristics, since in Chaigne's comprehensive model the decay factors depend on the eigenfrequencies of free transverse vibrations of bending waves. The eigenfrequencies ω_{mn} can be determined with Rayleigh's quotient using Warburton's mode shapes or with the pre-computed solutions by Warburton [7]. Both approaches are described in section 2.2. The force F acting at the point $\{x_0, y_0\}$ is modelled with Hertz's law of contact as described in section 2.4.1. Hence, $F(t)$ is based on a Hanning window specified by the maximum force F_{max} and the interaction time τ_H . The mode shapes for the spatial solution $Z_{mn}(x, y)$ are obtained using Warburton's characteristic beam functions that were described in section 2.2. Note that the mode shapes Θ_{mn} were normalized to a scalar product of one to ensure a uniform weighting of all modes for a point force $F = \delta(t)\delta(x - x_0, y - y_0)$. In order to model the sound radiation of the plate with Rayleigh's integral, the plate is discretized into small rectangular surface elements with the area $dS = dx dy$, as schematically shown in figure 30. The center of each element contains a point source at the position $\{x_i, y_i\}$ that radiates with the acceleration component normal to the plate at this specific point. Hence, the sound pressure is determined with Rayleigh's integral

$$p(r, \theta, \varphi, t) = \frac{\rho_{air}}{2\pi} \sum_i \frac{\partial^2}{\partial t^2} \frac{W(x_i, y_i, t - d_i/c_{air})}{d_i} dx dy, \quad (131)$$

where the integration over the plate surface is carried out as a summation of the contribution of all point sources. The sound pressure is synthesized at two observation points $p_l(t)$ and $p_r(t)$ that are later used for playback over headphones for the left and right ear. Since the model is intended to synthesize the sound of unbaffled objects, the acoustic shortcut between front and back surface of the object must be taken into account. To this end, a comprehensive numerical approach as described in [19] has been considered. However, since an implementation of this method was out of scope of this work, a more simple but effective approach was chosen for the final implementation. In [20], an empirical formula for the average radiation efficiency of an unbaffled plate was derived. With respect to the implemented synthesis model, the most important part of this formula represents the decrease of the radiation efficiency below the critical radiation frequency f_{crit} down to the lowest eigenfrequency with approximately 20 dB / decade. Hence, all modes below f_{crit} are simply weighted with the attenuation of a first-order highpass with a cutoff frequency at f_{crit} .

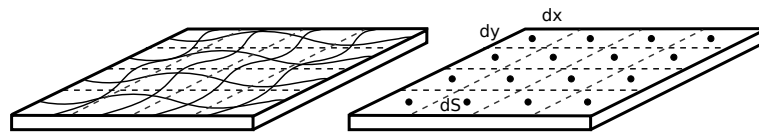


Figure 30 – Schematic displacement on a vibrating plate (left) and slicing of plate into rectangular surface elements with a point source at their centres (right).

3.3 Validation

Since the implemented synthesis model includes adapted and extended models from multiple literature sources, this section comprises a validation of the most important employed models. With reference to the block diagram in figure 29, the following aspects of the synthesis model have been validated:

- the excitation force $F(t)$ that serves as excitation signal,
- the determination of mode shapes with their associated eigenfrequencies,
- the plate damping law to determine the decay factors α_{mn} . For this reason, laser vibrometer measurements were carried out on selected plates.

In addition, the entire model was validated by comparing the synthesized sound pressure signal with results from literature as well as with recorded sounds of real impacted plates.

The excitation force was modelled with Hertz's law of contact as described in section 2.4.1 and in [8]. As validation, the implemented model is used to recreate the two examples from this literature source. The examples comprise a wooden bar that is excited with a mallet. While in the first scenario the head of the mallet consists of rubber, a mallet with a boxwood head is used in the second example. The employed model parameters are listed in table 9 and include all necessary material properties and the geometry of both the bar and the mallet. Only the bar's mass that influences the reduced mass was not available and has therefore been determined with the help of the impact duration τ_H . Note that for both mallets the measured and simulated data from the literature source was extracted directly from figures using the software WebPlotDigitizer¹. Thereby, the visualized literature data in figure 31 and figure 32 as well as the determination of the impact durations are approximations. Nevertheless, the comparison of the impact forces from the implemented model shows a very good agreement between the implementation and the simulated results by Chaigne. The difference in figure 31 for the maximum force between the simulations and Chaigne's measured results originates from the measurement standard deviation (34 %) for the determination of the stiffness constant K in [8]. With rubber being a material that would require a far more complex model to describe the impact, the simulated impact durations are about 20 % shorter than the measured one. Subsequently, the corresponding magnitude spectra contain less energy and their low-pass behaviour starts at higher frequencies.

Table 9 – Model parameters for Hertz's law of contact for a mallet with a rubber and a boxwood head for a weak (piano) and strong (mezzo-forte) impact. *Data from from [8].

	rubber	boxwood
stiffness constant K (N m ^{-3/2})	3.7×10^7 *	1.31×10^9 *
reduced mass μ (g)	14.1	14.2
impact speed V_0 (m / s)	0.26*; 1.0*	0.07*; 0.474*

1. freely available at www.automeris.io/WebPlotDigitizer

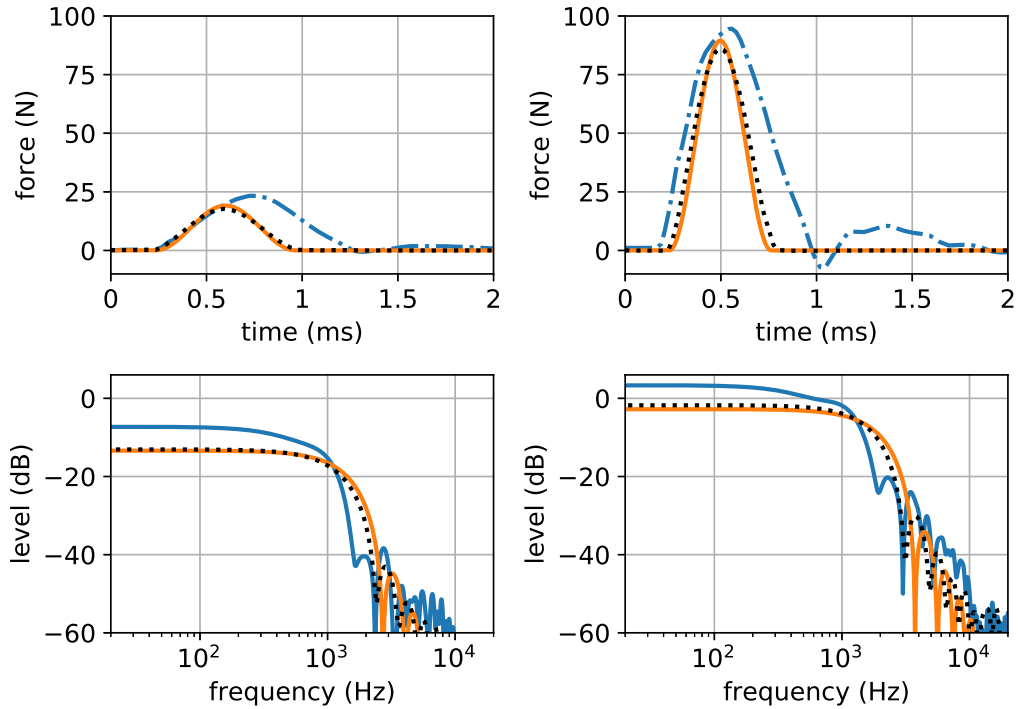


Figure 31 – Temporal progression (top) and magnitude spectrum (bottom) of the impact force for a rubber mallet with a weak impact (piano, left) and a strong impact (mezzo-forte, right). Comparison between results from implemented model (solid orange), simulated (dotted black) and measured (dashed-dotted / solid blue) result from Chaigne [8].

The results for the boxwood mallet in figure 32 show that the higher stiffness constant caused by the mallet material leads to a shorter impact duration and furthermore to a broader magnitude spectrum compared to the rubber mallet results. In general it can be said that the duration τ_H is the most important parameter for the excitation in the synthesis model since it defines the spectral characteristics of the impact force and therefore the weighting of a mode depending on its eigenfrequency. The employed window shape does influence the spectral characteristic of the impact force - however, simulations in [8] showed that small variations in the window shape have no significant consequences on the solution.

The next validation step includes the determination of the mode shapes and their associated eigenfrequencies ω_{mn} for various boundary conditions. By default, the synthesis model uses the plate mode shapes introduced by Warburton in [7]. For the trivial case of a plate simply supported on all edges no validation was carried out, since exact solutions of the plate bending wave equation are available. However, this configuration was used to test an employed finite element method (FEM) framework, which was used throughout this work for numeric simulations. Information on the used FEM framework and its validation with a simply supported plate can be found in appendix D. The validated FE model was then used to simulate plates with boundary conditions with no exact analytic

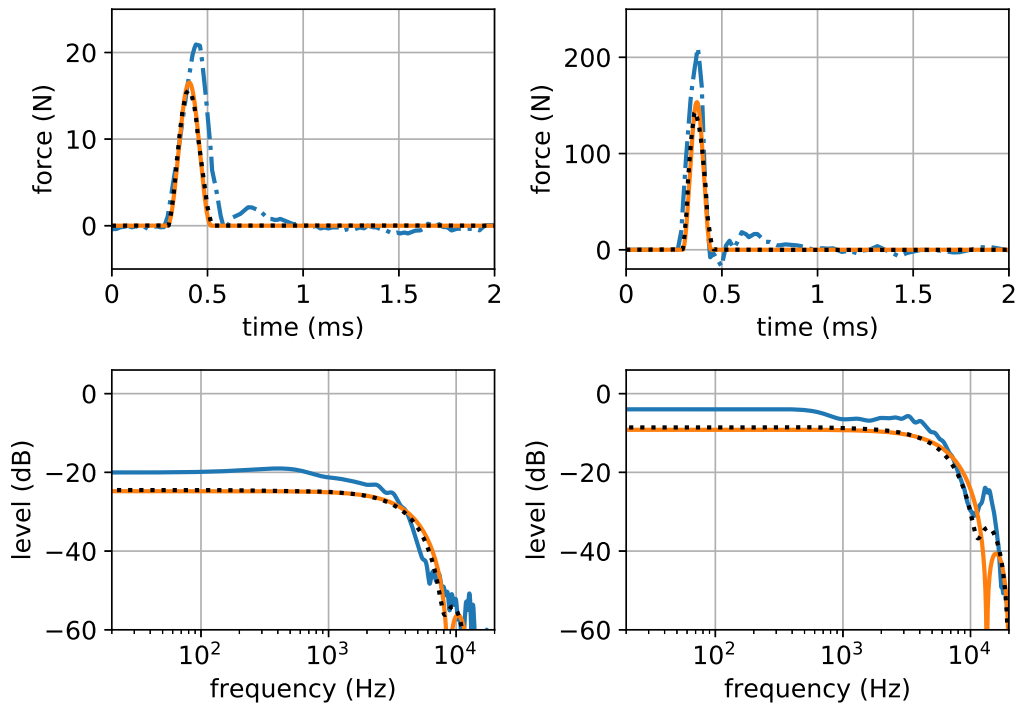


Figure 32 – Temporal progression (top) and magnitude spectrum (bottom) of the impact force for a boxwood mallet with a weak impact (piano, left) and a strong impact (mezzo-forte, right). Comparison between results from implemented model (solid), simulated (dotted) and measured (dashed-dotted) result from Chaigne.

solutions available. For these cases, the resulting mode shapes and eigenfrequencies served as ground truth. This approach was chosen analogously to [7], where a numerical method was used to get a ground truth for the model validations. However, Warburton applied the less sophisticated Rayleigh-Ritz method.

As mentioned in section 2.2, the mode shapes obtained with Warburton’s method solve the bending wave equation only approximately, if free edges are involved. Furthermore, the more the aspect ratio is closer to one, the more the effect of elastic interaction influences the mode shapes for these cases. For the model validation, the boundary conditions all edges free (ffff) and cantilever (cfff) from figure 10 were taken into account. Figure 33 shows a comparison between mode shapes of a square plate from Warburton’s approach and from FE simulations. The largest differences can be observed for the $\{2, 0\}$ - and $\{0, 2\}$ -mode and the corresponding mixed modes $\{2, 0\} \pm \{0, 2\}$, because Warburton’s mode shapes do not take into account elastic interaction. This influences the numeric calculation of Rayleigh’s integral, which may result in a deviation of the synthesized sound pressure for certain radiated modes, depending on the location of the observation points. From an acoustic perception point of view, these deviations have only a minor impact compared to the plate eigenfrequencies ω_{mn} and the corresponding decay factors α_{mn} , which also depend on the mode shapes.

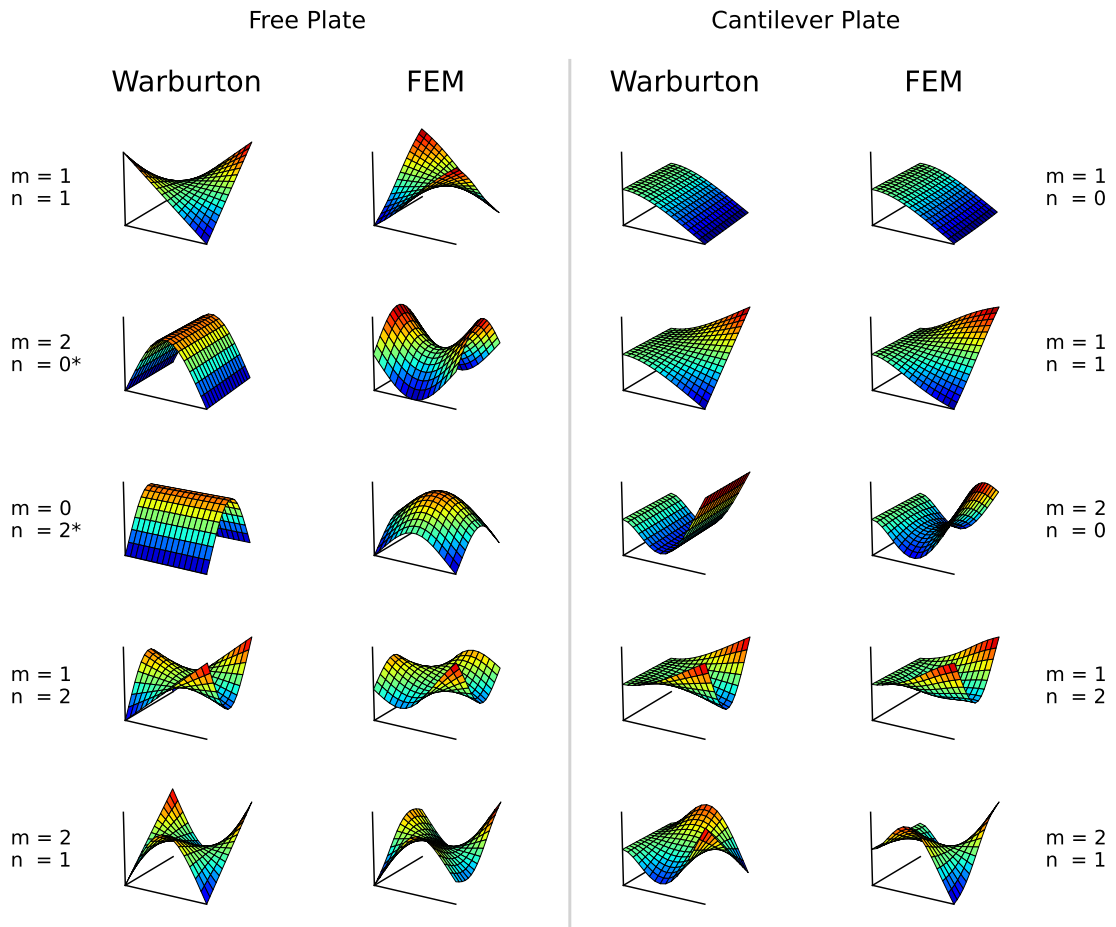


Figure 33 – Comparison between synthesis model mode shapes and shapes obtained from FE simulations for a square plate. *FE-simulated modes are actually mixed pair of the form $\{2, 0\} \pm \{0, 2\}$.

For the validation of the eigenfrequency determination method of the model, the results from own FE simulations as well as from Chaigne in [9] were taken into account. Therefore, a set of three plates was investigated, which has the same dimensions and material properties as the aluminium plates a_1 , a_3 and the glass plate v_1 in [9]. Basic and detailed information about these three plates are part of figure 34 and appendix C.

The synthesis model offers the possibility to determine ω_{mn} with Rayleigh's quotient or with the simplified Warburton formula. As described in section 2.2, both approaches rely on the product of the characteristic beam functions introduced by Warburton in [7], which are known to solve the plate bending wave equation only approximately if free edges are involved. However, the first validation step includes a comparison of these approaches for the considered plate set and the boundary conditions ffff and cfff. Taking the lowest 200 modes for each case into account, the relative frequency difference between the Rayleigh's quotient calculations and the simplified Warburton approach did not exceed 0.07 %, except for shapes with the mode number 1 associated with the clamped and

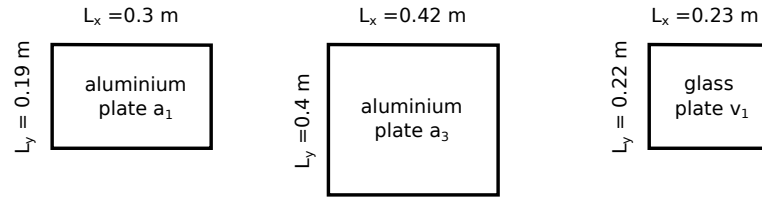


Figure 34 – Basic information of investigated plates. Not to scale. Accurate dimensions and material properties can be found in appendix C.

the opposing free edge of the cantilever plate. The maximum relative deviation of 4.6 % for this special case can be traced back to the corresponding expression given in table 5, which is in fact an approximate calculation of the integrals in equation 64 and 65. Hence, apart from modes including $m = 1$ for the cantilever plate, Warburton's simple approach delivers very similar results with the additional benefit of less computational effort.

The second validation step comprises a comparison between eigenfrequencies obtained with Warburton's approach, FE simulations and the literature results from Chaigne for plates with all edges free. As exemplary results for the plates a_3 and v_1 in figure 35 show, there is generally a good agreement between analytic model, FE simulations and literature results in terms of absolute values. However, since both plates have an aspect ratio close to one, the determined eigenfrequencies for low mode numbers from Warburton's approach are different from the FE and the literature results in terms of relative deviations. These deviations can be attributed mainly to two aspects. The first aspect concerns the characteristic beam functions introduced in equation 59, which solve the bending wave equation only approximately. The second represents the elastic interaction between modes with the numbers $\{m, n\}$ and $\{n, m\}$, where $m - n$ is a non-zero even number, if the aspect ratio is close to one. Poisson coupling for the mode $\{m, n\} + \{n, m\}$ increases and the added stiffness for the mode $\{m, n\} - \{n, m\}$ decreases the resulting eigenfrequency compared to the eigenfrequencies of the modes $\{m, n\}$ and $\{n, m\}$. As mentioned in section 2.2, Warburton introduced a correction factor to address these deviations for square plates. Within this work, ideas were developed to empirically derive a correction factor also applicable for non-square free plates. However, since the implementation of such a factor was out of scope, by default the implemented synthesis model uses Rayleigh's quotient or the simplified Warburton formula without a frequency correction factor.

Another aspect of vital importance to the synthesis model is the plate damping law from section 2.3.3. For validating the damping law the same set of plates in figure 34 was investigated to recreate the literature examples from [9]. In addition, the model was assessed with own laser vibrometer measurements on replica plates. Apart from manufacturing tolerances, these plates had the same dimensions and were made of the same materials as in [9]. A detailed description of the laser vibrometer measurements and the procedure to estimate the decay factors α_{mn} can be found in appendix E. Note that the theory behind the damping law is summarized in section 2.3.3 of this work.

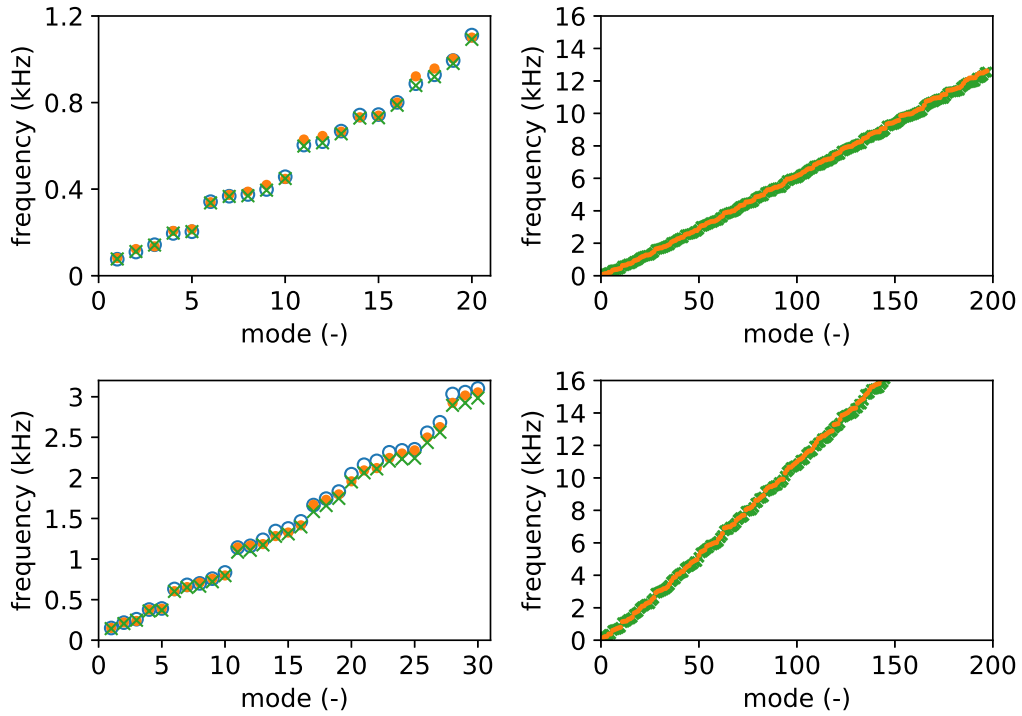


Figure 35 – Comparison between eigenfrequencies obtained with the implemented Warburton method (orange dots), FE simulations (green "x"), and measured eigenfrequencies from Chaigne for the aluminium plate a_3 (top) and the glass plate v_1 (bottom) with all edges free.

The validation procedure of the damping law was divided into two parts. In the first, attempts were made to recreate the literature results from Chaigne, including an estimation of the thermoelastic and viscoelastic constants. The second step comprised a fit of the damping law parameters to own measurement results from the replica plates. A detailed discussion of the results for the aluminium plate a_1 will reveal the reasons behind the chosen validation approach for the plate damping law.

The first investigated plate was the aluminium plate a_1 with the corresponding results visualized in figure 36. As mentioned in section 2.3.3, the damping law considers thermoelastic and radiation damping for metals. Using the mode shapes from Warburton or from FE simulations to determine the decay factors both lead to comparable results and show a good agreement with the literature results. The erratic behaviour of Chaigne's measurement results within the region of the critical radiation frequency and above are very likely due to measurement uncertainties, since a decay factor of 100 would already correspond to a hardly accurately measurable decay time T_{60} of 69 ms.

Although the measurement setup and the plate itself were recreated as close as possible as described in [9], the own measured decay factors are consistently larger than the decay factors measured by Chaigne. A possible explanation to this could be a different influence of the suspension of the plate. However, as shown later in this section, the measured decay factors for the own glass plate v_1 with the same suspension method

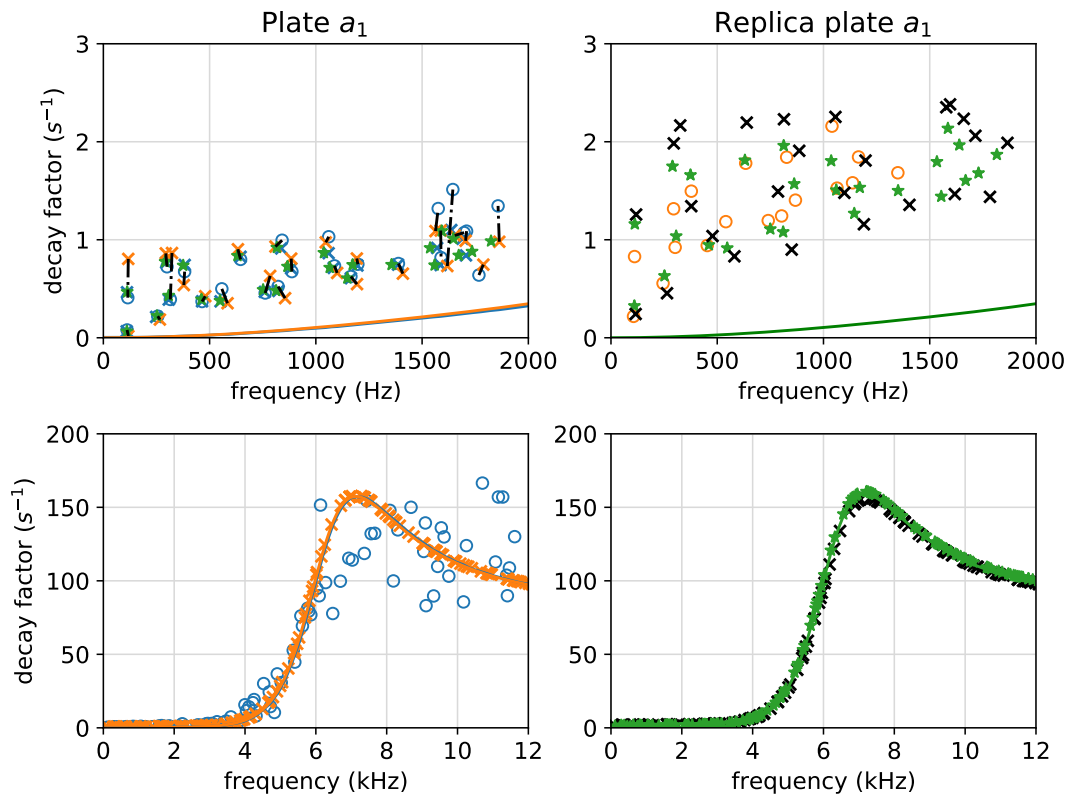


Figure 36 – Left: comparison between decay factors from Chaigne’s [9] measurements (blue circles) and prediction (blue "x"), own predicted values using Warburton’s (orange "x") and FE-simulated (green stars) mode shapes. Right: comparison between decay factors from own measurements (orange circles), predicted values from FE-simulated mode shapes using a least-squares fit for R_1 and c_1 (green stars) and prediction with Warburton’s mode shapes using literature values for thermal constants (black "x"). The solid lines represent the radiation damping obtained by Chaigne (blue) and own implementation (orange and green).

showed a significantly better agreement with the literature results. Furthermore, not all thermoelastic constants determined by Chaigne are within a plausible value range for the material aluminium. For example the constant c_1 , listed with a value of $8 \cdot 10^{-4}$ in [9], is significantly smaller than determined according to equation 87 with typical values for the material aluminium. This can be attributed to the fact that Chaigne’s thermoelastic constants were determined from a best fit to his measurement results using the damping model. Thus, own values for the thermoelastic constants R_1 , c_1 as well as elastic constants were determined to best fit the decay factors from the own measurements with respect to plausible values ranges for aluminium. The obtained final results with these constants using FE mode shapes are visualized in the right part of figure 36 and show a fairly good agreement with the measured decay factors. In addition, the decay factors were also predicted using only literature values for the elastic and thermoelastic constants. This last naive approach utilized the simplified Warburton

equations to determine the eigenfrequencies and the associated mode shapes. As a consequence, the resulting eigenfrequencies in figure 36 show a larger deviation from the measured and the FE-simulated eigenfrequencies. However, the predicted decay factors are still within a similar range, if a correction factor for the modes $\{1, 1\}$, $\{2, 0\}$ and $\{0, 2\}$ is considered.

In summary, the validation of the damping law with focus on thermoelastic damping showed predicted decay factors, which are within a similar range as the measured decay factors. Differences between decay factors also occurred between the literature measurement results from [9] and the own results from own laser vibrometer measurements. Although the exact origin of these deviations is not known, it can be concluded that the accuracy of the implemented damping law is sufficient for the synthesis model, if the deviations are within a similar value range as the measurements and the predictions with the FE mode shapes and eigenfrequencies.

In order to validate the damping model with focus on viscoelastic damping, the second plate under investigation was the glass plate v_1 . Analogous to the comparison for the plate a_1 , predicted and measured decay factors are visualized in figure 37. As already mentioned - apart from measurement uncertainties due to the larger damping - the decay factors obtained from the own laser vibrometer measurements show a good agreement with the measured and predicted literature results, as well as with the own predictions. The difference between the predicted decay factors above the critical frequency for the literature plate and the replica plate could be traced back to the thickness difference of 0.2 mm, which is in fact a manufacturing tolerance. However, from a perceptive point of view, a higher critical frequency might have an actual influence, but e.g. decay factors of 150 and 200 would correspond to T_{60} decay times of 46 ms and 35 ms. Due to obvious reasons, this difference is negligible. The underlying viscoelastic constants R_1 , R_2 and s_1 , s_2 for the plate damping are not directly connected to any material properties. However, the slope of the approximately linear increase of the decay factor below the critical frequency is connected to the inherent loss factor η of the material. For the plate v_1 , the estimated loss factor for both the literature and the replica plate are within a plausible value range for the material glass. Hence, using a loss factor from [13] or the provided viscoelastic constants R_1 , R_2 and s_1 , s_2 in [9] led to a good agreement with the measured decay factors.

The final validation of the overall sound synthesis model was also carried out in two steps. Since the main part of the model is based on [18], the first step comprises a comparison with the available literature results, which consist of simulations and acoustic measurements. In the second step, the model is used with the dimensions and average literature material parameters of the replica plate a_1 . The synthesized sound is then compared to a real sound recording from the replica plate struck with a felt mallet. Detailed information about the replica plate a_1 can be found in appendix C.

For the comparison of the overall synthesis model with the literature data from [18], different settings and parameters had to be selected than for the already described validations. In order to ensure comparability, the first 10^4 modes were taken into account as in this specific literature. Together with the requirement to separate the initial defor-

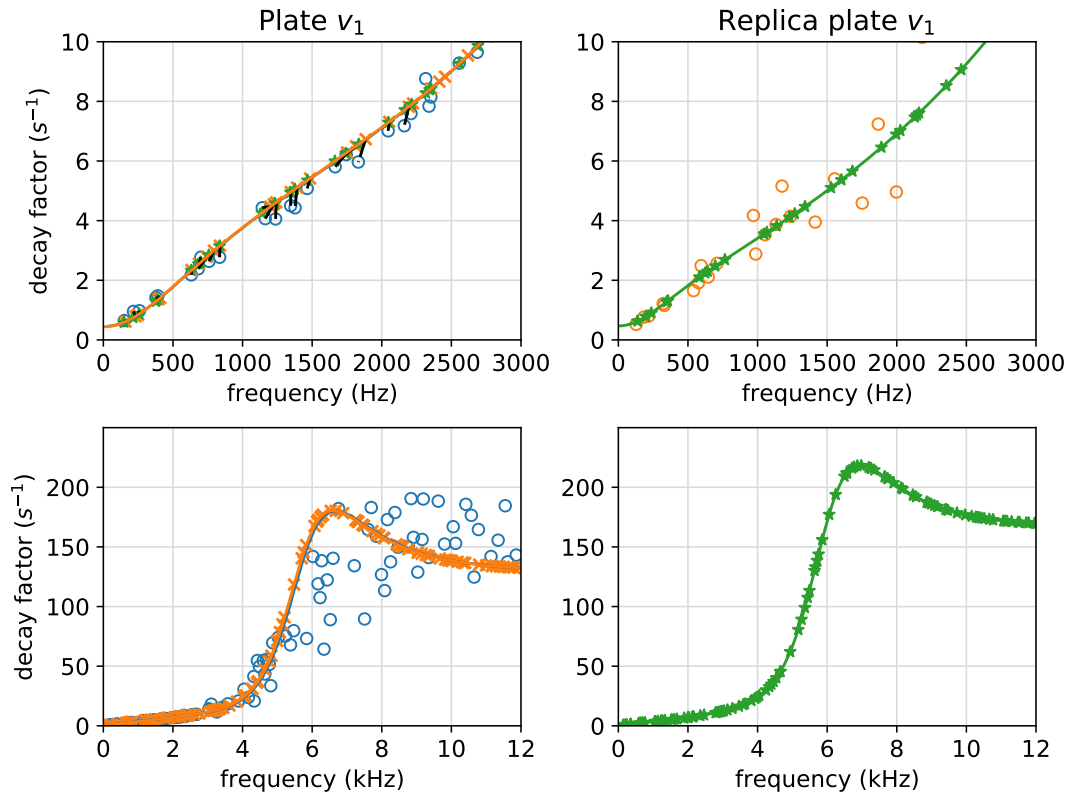


Figure 37 – Left: comparison between decay factors from Chaigne’s [9] measurements (blue circles), own predicted values using Warburton’s (orange "x") and FE-simulated (green stars) mode shapes. Right: comparison between decay factors from own measurements (orange circles), predicted values from FE-simulated mode shapes using a least-squares fit for R_1 , R_2 and s_1 , s_2 (green stars). The solid lines represent the viscoelastic damping (top) and total damping (bottom) obtained by Chaigne (blue) and own implementation (orange and green).

mation at the impact point from the radiated modes, a sample rate of 2.4 MHz was chosen. This also allowed a faithful reproduction of the impact force in figure 38 that was used in [18]. Note that this impact force originates from a more sophisticated model that simulates an elasto-plastic impact between a steel sphere and the employed aluminium plate. Detailed information about this investigated plate is provided in appendix C. On the other hand, the employed damping behaviour for this case is simply a constant damping ratio of $\zeta = 0.025$, which equals to a damping law of $\alpha = \zeta\omega$. The geometric synthesis setup is equivalent to the one in figure 28.

The results for this first overall model validation are visualized in figure 39. For both observation points, the own simulation results show a very good agreement with the measured and simulated literature results from [18]. In case of the observation point close above the center of the plate, the contribution of the initial deformation at the impact point and the radiation of the evolving modes can be separated clearly. Furthermore, this comparison shows that the implemented synthesis model is able to adequately synthesize

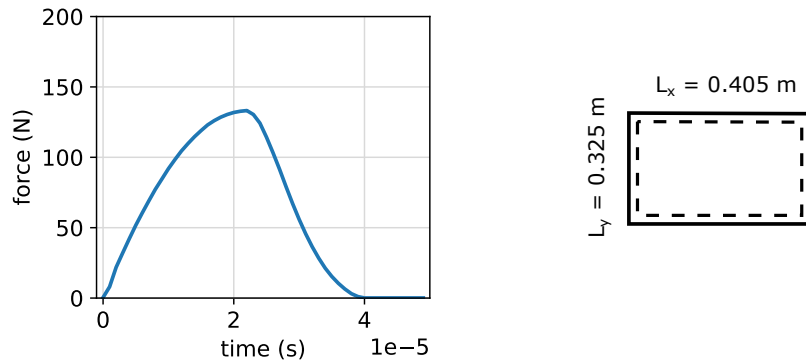


Figure 38 – Interaction force of an elasto-plastic impact (left) of a steel sphere with the investigated aluminium plate (right) from [18].

the actual sound pressure in terms of absolute physical values.

In order to validate the overall synthesis model with the sound of a real impacted plate, own acoustic measurements were carried out with the aluminium replica plate a_1 . As visualized in figure 40, the plate was struck with a felt mallet near a corner of the plate to excite as many plate modes as possible with a single impact. The radiated sound was captured with two microphones positioned along an imaginary axis perpendicular to the plate. While the microphone mic 1 in the vicinity of the plate was intended to record the plate sound with minor influence of any destructive acoustic interferences, the sound captured by mic 2 should mimic a more common listening position. The parameters used as input for the synthesis model are listed in table 10, with the dimensions and the density of the replica plate being part of table 14.

A comparison between the magnitude spectra of the synthesized and the real impact sound of the aluminium plate a_1 in figure 41 shows a good agreement in terms of lo-

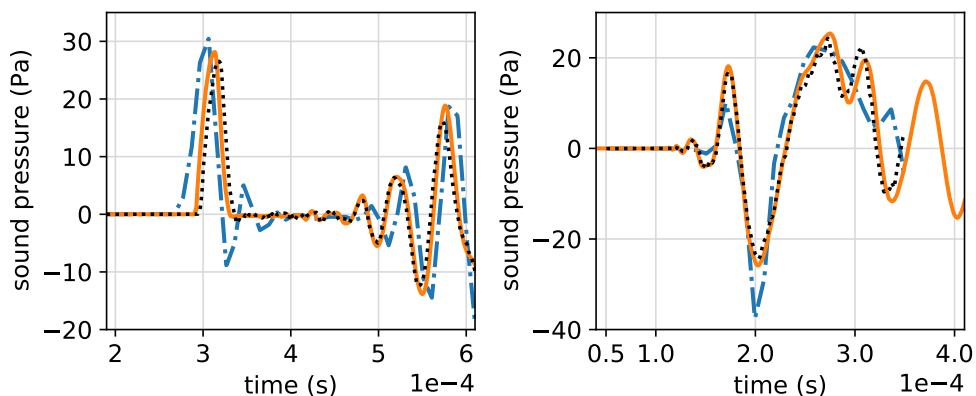


Figure 39 – Comparison between sound pressure of own implemented model (solid), simulated (dotted) and measured (dashed-dotted) results from [18] for observation points located at $x_M = L_x / 2$, $y_M = L_y / 2$, $z_M = 10$ cm (left) and at $x_M = 0.304$ m, $y_M = 0.163$ m, $z_M = 0.031$ m (right).

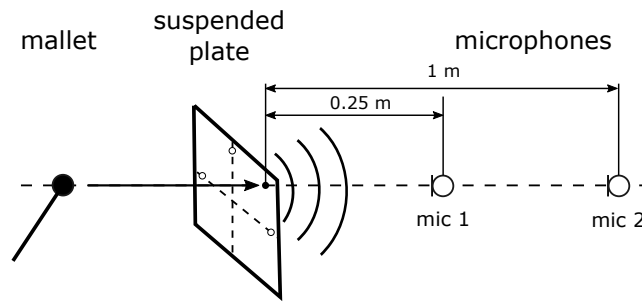


Figure 40 – Acoustic measurement setup. Not to scale.

-cation of the eigenfrequencies. The individual differences between specific modes of the real and the synthesized sound could be traced back to multiple aspects. On the one hand, the differences between decay factors as exemplarily highlighted in figure 36 led to a slower or faster decay of the modes, as observable in the spectrograms in figure 41. Furthermore, constructive and destructive acoustic interferences differ between the sounds obtained from the real and simulated setup. However, from a perception point of view, the synthesis of all investigated replica plates a_1 , a_3 and v_1 led to sounds similar to their real-life counterparts.

Table 10 – Parameters and material properties used to synthesize the sound of the aluminium replica plate a_1 . *Material parameters based on average of typical values ranges from text books.

sample rate (kHz)	44.1
spatial sample rate (m^{-1})	$100 / L_x; 100 / L_y$
number of modes (-)	256
heat capacity C_t (J / kg °C)	900
thermal expansion coefficient α_t ($10^{-6} / K$)	24
thermal conductivity κ_t (W / m K)	117
Young's modulus E (GPa)	69*
Poisson's ratio ν (-)	0.3*
mallet impact position (m)	$L_x / 10; L_y / 10$
mallet radius R_I (mm)	10
mallet mass M_I (g)	23.6
mallet stiffness constant K ($m N^{-2/3}$)	$9 \cdot 10^6$
impact speed V_0 (m / s)	0.6

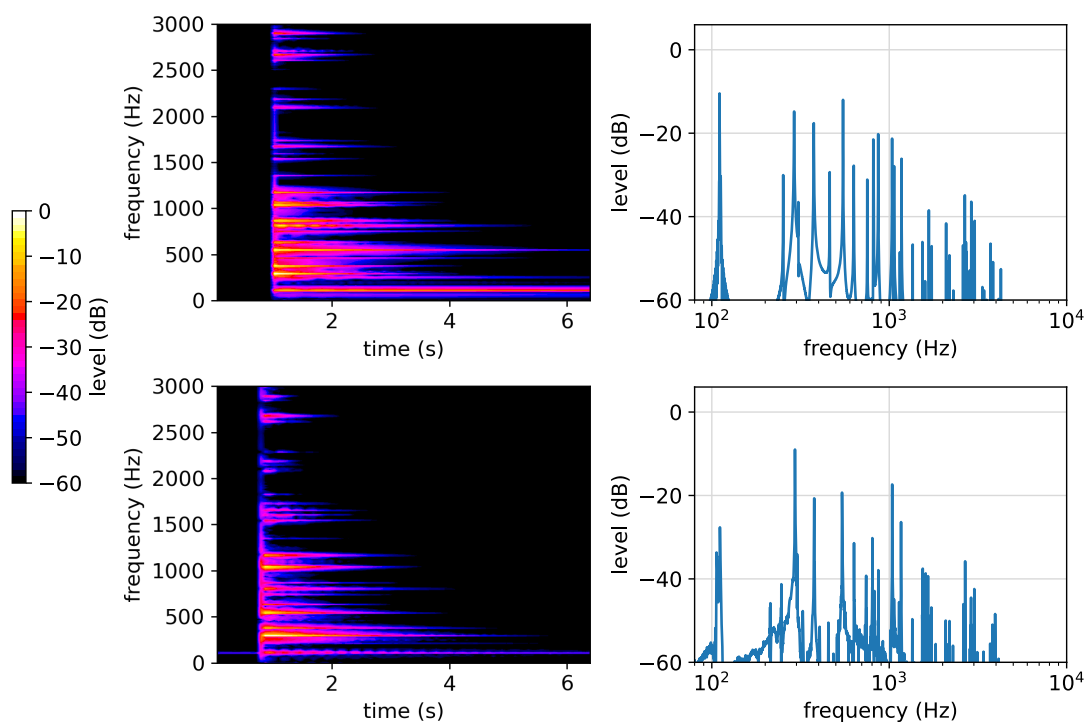


Figure 41 – Spectrograms (left) and magnitude spectra (right) of the synthesized (top) and real (bottom) sound of the impacted replica plate a_1 at the observation position of mic 1.

4 Acoustic Characterization of Rectangular Plates

In the following section, a method developed to estimate the geometry and material properties of rectangular plates will be presented. It utilizes both the knowledge from literature on the acoustics and psychoacoustics of plates described in section 2, as well as the findings from the implemented synthesis model and the corresponding measurements from section 3.

For the descriptions and investigations in this section, a simple model of the form

$$x(t) = \sum_{m=1}^M A_m \sin(\omega_m t + \varphi_m) e^{-\alpha_m t} \quad (132)$$

is assumed for the sound of an impacted plate. Depending on the position of the impact on the plate and the subsequent sound radiation to the observation point, the mode m with the angular eigenfrequency $\omega_m = 2\pi f_m$ is weighted with the factor A_m and subsides with a decay factor α_m over time.

A realistic situation in which a human would try to detect the properties of a physical object by ear would consist of tapping, knocking and scratching the object at multiple positions while listening to the emitted sounds in the vicinity of the object. In order to mimic this situation in a simplified and reproducible way, the plate sound $x(t)$ is assumed to be caused by a single mallet impact at the corner of the plate captured at a listening position in the vicinity of the plate. This ensures a sound rich in excited modes while minimizing destructive acoustic interferences at the observation point. Figure 42 illustrates the acoustic identification setup and its simplification for the implemented characterization method.

The first part of the characterization method comprises the extraction of the parameters f_m and α_m , as depicted in figure 43. The extracted eigenfrequencies and the associated decay factors then serve as basis for multiple procedures - a frequency band analysis of the decay factors to determine the critical radiation frequency f_{crit} , a decay factor regression to estimate the material-inherent loss factor η , and a steepest descent algorithm to fit the eigenfrequencies to a model plate with specific dimensions and material properties.

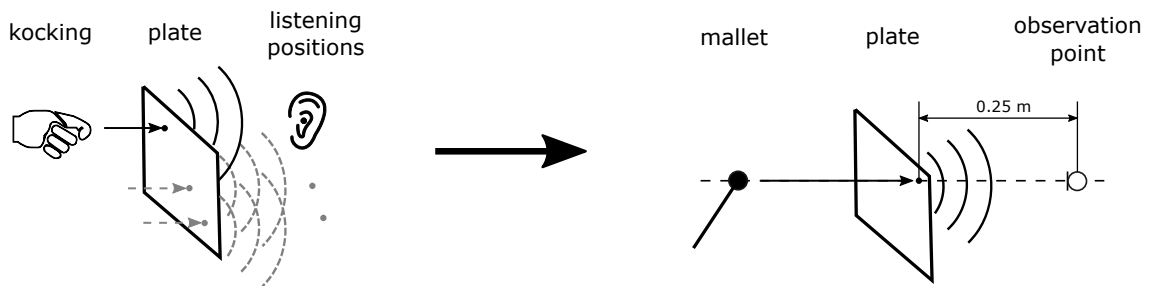


Figure 42 – Sketch of assumed acoustic identification situation (left) and simplified setup for the developed acoustic characterization method (right). Not to scale.

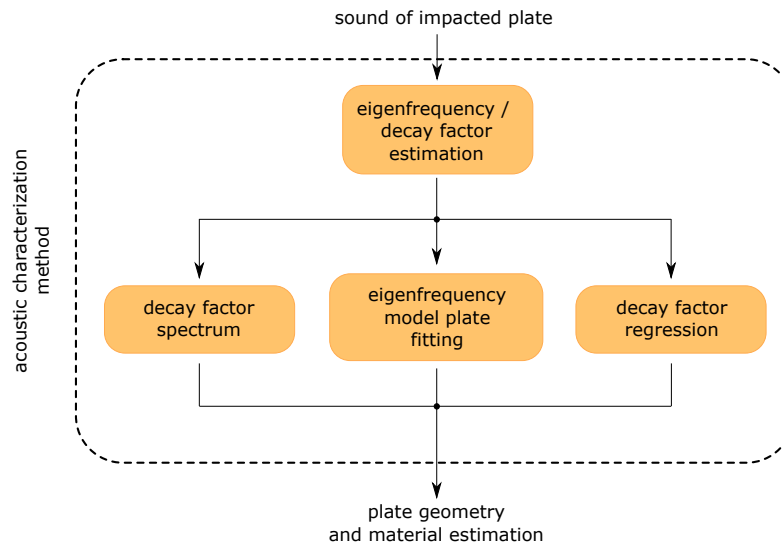


Figure 43 – Overview of the acoustic characterization method.

For all discussed aspects and investigated plates within this section, a plate as in figure 9 in section 2.2 is assumed. Furthermore, if not mentioned otherwise, the plates edges are free as well as all defined quantities and their associated symbols in section 2 are used throughout this section.

4.1 Estimation of Eigenfrequencies and Decay Factors

In order to get a profound basis for the estimation of the geometry and the physical properties of a plate, the first step of the characterization method comprises the extraction of the eigenfrequencies f_m and the decay factors α_m . As illustrated in figure 44, this determination process can be further subdivided into three different tasks. The most prominent eigenfrequencies of the plate sound are extracted using a partial tracking algorithm. Subsequently, the eigenfrequencies control a Gaussian band-pass filter bank that attempts to isolate the decaying modes within the plate sound. In the third part, the decay factor α_m of each mode is estimated with a linear regression applied on the logarithmic envelope of the filtered signal.

The detection and tracking of multiple prominent frequencies in a signal is a frequently encountered task in a wide range of applications, such as in speech processing and synthesis [21], digital audio signal processing in musical applications [22], or engine order tracking in the field of automotive sound engineering [23]. First published in [21], one of the basic partial tracking algorithms connects frequency peaks between frames of the short-time Fourier transform (STFT) of a signal to contiguous peak tracks. While in its original form this algorithm connects peaks with a minimum frequency difference and assumes a stationary short-time signal model, improvements presented in [24] and [25] assign a bandwidth to the tracked partials and allow for an intermediate "sleep" state of peak tracks.

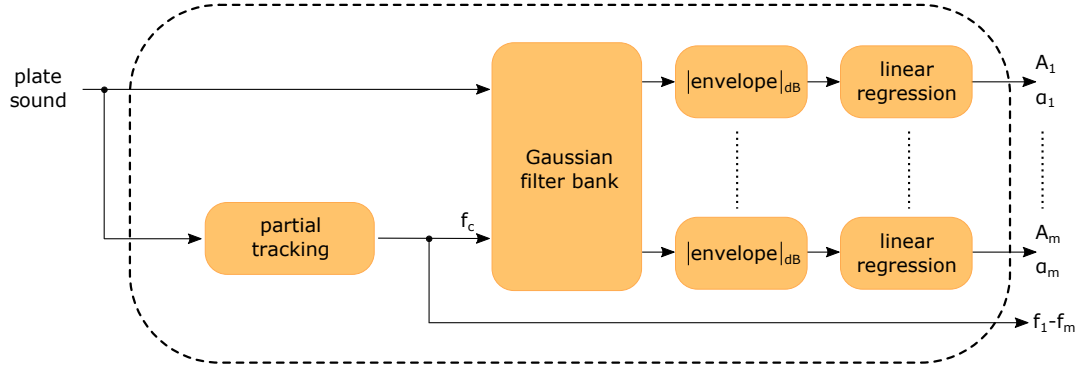


Figure 44 – Overview of the steps involved in the estimation of the eigenfrequencies and decay factors.

For the estimation of the eigenfrequencies f_m in the plate sound, the partial tracking algorithm from [26] was used. Note that this algorithm was selected for the acoustic characterization method due to its availability², but also because of its presented performance in the literature mentioned above. In contrast to the signal model employed in [21], this algorithm uses a model of the form

$$s(t) = \sum_{p=1}^P e^{a_p(t) + j\phi_p(t)} \quad \text{with} \quad \phi_p(t) = \phi_p(0) + 2\pi \int_0^t f_p(u) du, \quad (133)$$

where a_p , ϕ_p and f_p are the instantaneous log-amplitude, phase and frequency of the partial p . For each frequency peak i in the analysis frame k of the STFT centred around $n = 0$, the short-term signal model consists of

$$s(n) = \sum_{i=1}^I e^{\sum_{q=0}^Q \beta_{iq} n^q}, \quad (134)$$

from which the partial properties can be determined with

$$a_{p,k}(n) = \text{Re} \left\{ \sum_{q=0}^Q \beta_{iq} n^q \right\}, \quad \phi_{p,k}(n) = \text{Im} \left\{ \sum_{q=0}^Q \beta_{iq} n^q \right\}, \quad f_{p,k}(n) = \frac{f_s}{2\pi} \text{Im} \left\{ \sum_{q=0}^Q \beta_{iq} q n^{q-1} \right\}. \quad (135)$$

Possibilities for estimating the complex-valued parameter β_{iq} are described in [26], and the default settings for this algorithm uses the distributive derivative method (DDM) with a polynomial order of $Q = 2$. The connection between frequency peaks in two consecutive analysis frames is carried out by solving a linear assignment problem. Being a fundamental combinatorial optimization problem, the basic task can be described with a set of R agents that must be assigned exclusively to a mission within a set of R missions. As visualized in figure 45, the assignment of each agent i to the mission j is associated with the cost C_{ij} in the cost matrix C . Solving the linear assignment problem corresponds to the minimization of

2. Matlab code freely available at www.github.com/jundsp/Fast-Partial-Tracking

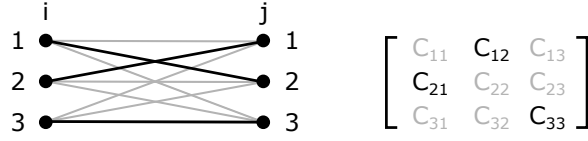


Figure 45 – Illustration of a basic linear assignment problem (left) and the associated cost matrix C (right).

$$\min \left\{ \sum_{i=1}^R \sum_{j=1}^R C_{ij} X_{ij} \right\} \quad \text{with} \quad \sum_{i=1}^R X_{ij} = 1, \quad \sum_{j=1}^R X_{ij} = 1. \quad (136)$$

The matrix X represents a binary matrix only containing values of 1 for assignments between agents and missions. The actual assignment problem for the employed partial tracking algorithm represents a multi-criteria assignment problem, since the objective function consists of two decision criteria and therefore two separate costs - one for connecting two frequency peaks between consecutive analysis frames and one for not connecting them. Calculating these costs and subsequently the cost matrix C is described in detail in [26].

The application of the partial tracking algorithm from [26] on a synthesized and a real sound of the impacted replica plate a_3 is shown in figure 46. Since both plate sounds are rich in radiated modes, the algorithm is able to detect and track the majority of the eigenfrequencies below 3 kHz. Above approximately 3 kHz, radiation damping causes the modes to decay fast after the impact. Furthermore, the low-pass characteristics of the interaction force between the impactor and the plate leads to a weaker excitation of modes in the upper frequency regions. However, an accurate detection and tracking of these modes and their associated eigenfrequencies is not required for the acoustic characterization method. Below 50 Hz, the sound of the real plate visualized in figure 46 contains mostly uncorrelated low-frequency noise, which was deliberately preserved to test the algorithm. For the investigated plate sounds, the partial tracking detected the spectral peaks caused by the noise but did not construct any longer spurious peak tracks that could be mistaken as decaying modes.

For the next analysis step, the average frequencies of the most prominent detected partials serve as center frequencies for a Gaussian band-pass filter bank. An ideal Gaussian filter with the center frequency f_c and the standard deviation σ can be described by

$$h_G(t) = \frac{1}{\sqrt{2\pi}\sigma} e^{-t^2/2\sigma^2} \cos(2\pi f_c t), \quad (137)$$

and has the benefit of preserving the exponential decay of a mode, if the signal $x(t)$ is convolved with the filter impulse response $h_G(t)$. One way to implement the above equation as a discrete-time filter involves truncating the impulse response $h_G(t)$ after shifting it in time by T_0 . For a filter bandwidth Δf with the cut-off gain G , the corresponding standard deviation computes to

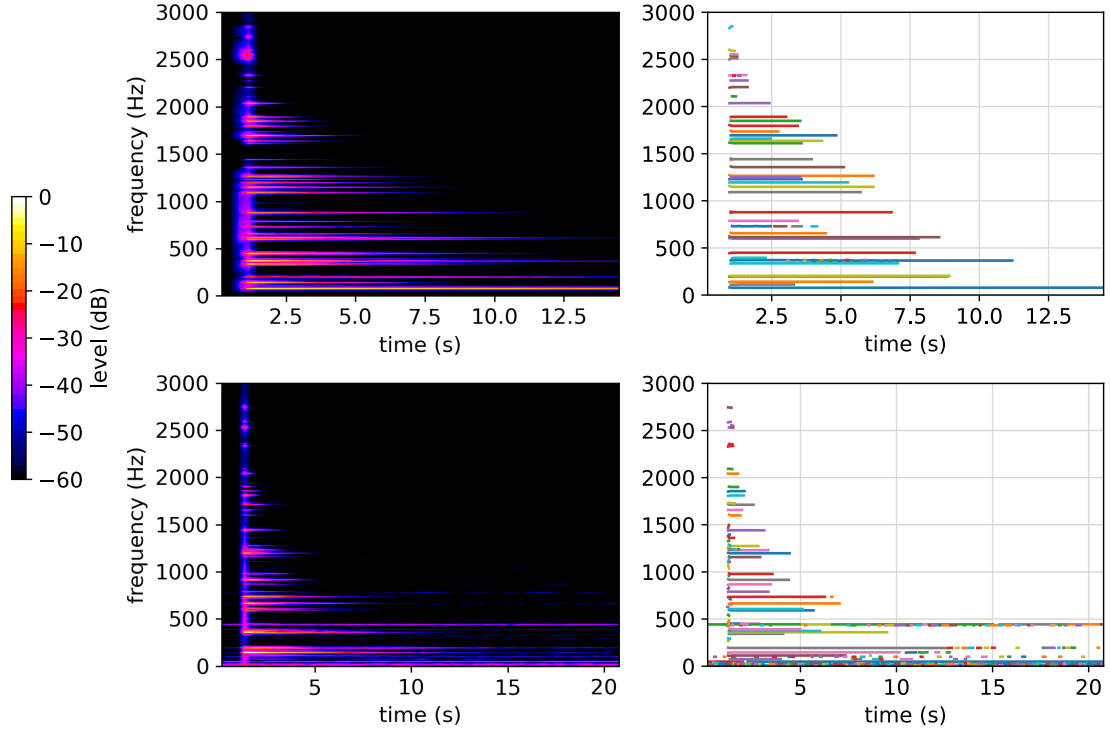


Figure 46 – Spectrogram (left) and extracted partials (right) of the synthesized (top) and real (bottom) sound of the impacted replica plate a_3 .

$$\sigma = \frac{\sqrt{2 \ln(G^{-1})}}{\pi \Delta f}. \quad (138)$$

Methods to efficiently implement Gaussian filters as IIR filters are described in [27]. For the developed characterization method, the band-pass filter bank contains a Gaussian filter for each selected partial with the average frequency $\bar{f}_p = f_m = f_{c,m}$, with $f_{c,m}$ being the center frequency of the filter. In order to minimize the influence of partially overlapping modes, the bandwidth Δf_m of each filter is individually set to

$$\Delta f_m = 2 \min\{|f_m - f_{m-1}|, |f_m - f_{m+1}|\}. \quad (139)$$

For the investigated plate sounds, a cut-off gain of $G_{dB} = -40$ dB lead to a satisfying isolation of slowly decaying modes, if neighbouring modes were overlapping partially. In case of fast decaying modes, the convolution with the filter impulse response h_G may significantly influence and extend the signal envelope. Exemplary frequency responses of designed Gaussian band-pass filters to extract the modes of a plate sound are visualized in figure 47.

In the next step, the envelope $E(t)$ of each band-pass filtered signal $x_m(t)$ is estimated. Using the Hilbert transform, the envelope $E_m(t)$ is determined according to

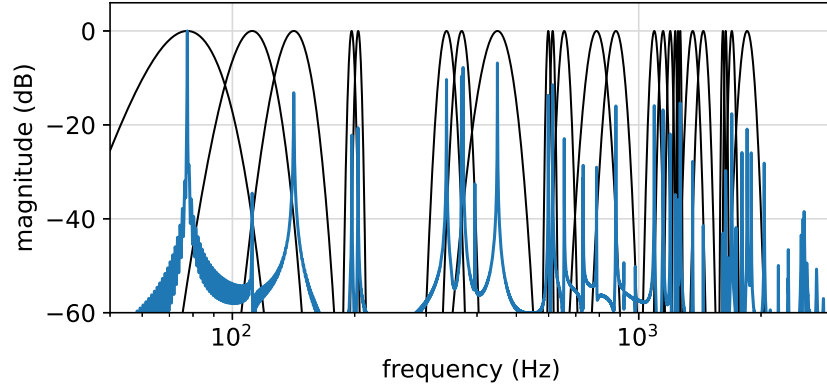


Figure 47 – Frequency responses of designed Gaussian band-pass filters with $G_{dB} = -40$ dB (black) and magnitude spectrum of the synthesized sound of the impacted replica plate a_3 (blue).

$$E_m(t) = |x_m(t) + jH\{x_m(t)\}|, \quad (140)$$

where $H\{\}$ denotes the Hilbert transform. Assuming an extracted exponential decay of the form $E_m(t) = E_{0,m}e^{-\alpha_m t}$, the conversion to

$$\ln(E_m(t)) = -\alpha_m t + \ln(E_{0,m}). \quad (141)$$

leads to a linear decrease with the slope $-\alpha_m$. In practice, this slope is determined with a linear regression and serves as an estimation of the decay factor α_m of the mode m . In order to minimize a potential influence of the Gaussian filter impulse response, its length was considered for the starting point of the linear regression. The intercept $\ln(E_{0,m})$ represents an estimation of the scaling factor A_m in the model from equation 132. However, the scaling factors are not used for the actual characterization procedure, as described in detail in section 4.2. Figure 48 visualizes the estimation of the decay factor with an exemplary band-pass filtered signal of a real sound of the impacted replica plate a_3 .

The application of the entire procedure depicted in figure 44 on the sound of an impacted plate leads to an estimation of the eigenfrequencies f_m and the associated decay factors α_m . For investigated plate sounds rich in weakly damped modes below the critical radiation frequency of the plate, the estimation procedure led to satisfying results. However, since sounds of real impacted plates only approximately correspond to the assumed signal model from equation 132, the estimation procedure usually performs better for synthesized plate sounds, as exemplary shown in figure 49.

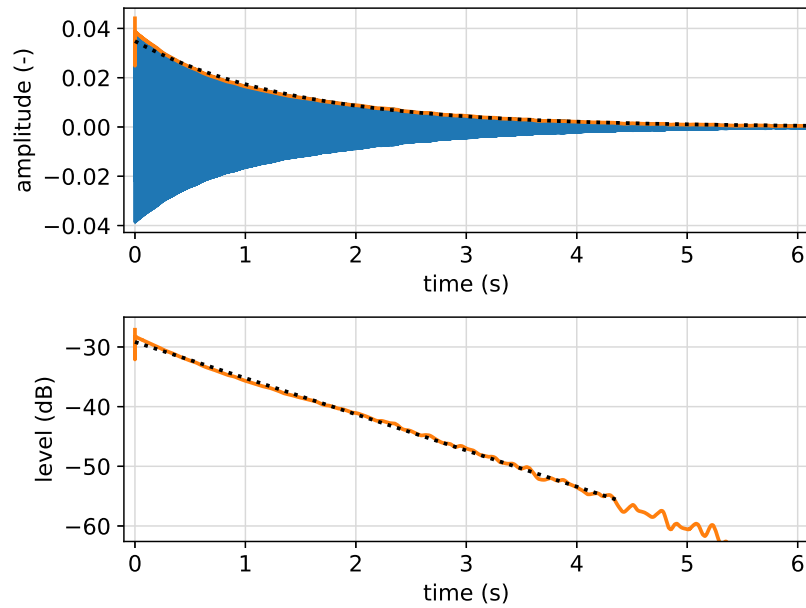


Figure 48 – Top: band-pass filtered signal (blue), determined analytic envelope (orange) and estimated envelope from regression analysis (black) of a real sound of the impacted replica plate a_3 . Bottom: corresponding linear regression (black) of logarithmic envelope (orange).

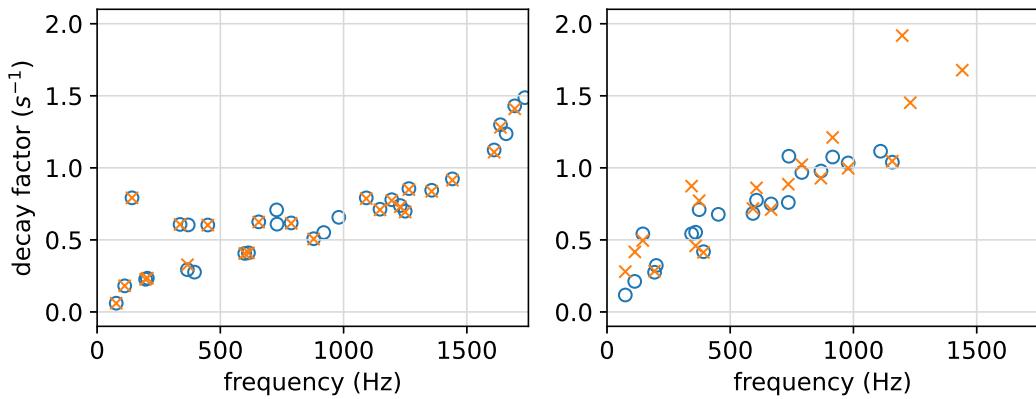


Figure 49 – Actual (blue circles) and extracted (orange "x") decay factors from synthesized (left) and real (right) sound of the impacted replica plate a_3 . The actual decay factors of the real plate were determined from laser vibrometer measurements.

4.2 Estimation of Geometry and Material Properties

The eigenfrequencies f_m and decay factors α_m extracted with the procedure described in the previous section serve as basis for the actual estimation of the geometry and the material of the impacted plate. As visualized in figure 43, the developed acoustic

characterization method employs three different types of analyses to obtain information about the characteristics of the plate. The first comprises an estimation of the critical radiation frequency f_{crit} from the plate sound's third-octave band decay factor spectrum. Below this critical frequency, a simple regression analysis of the frequency-dependent decay factor is carried out to extract information about the plate material, such as the material-inherent loss factor η . The third analysis fits the estimated eigenfrequencies to a large number of model plates with specific dimensions and material properties by solving a linear assignment problem. In conjunction with a steepest descent algorithm, this analysis attempts to find the most likely aspect ratio r_a of the plate. Furthermore, by combining the results from all three analyses, it is possible to estimate the plate area A and the factor $h\sqrt{\frac{E}{\rho}}$.

As mentioned in section 2.5, at the critical radiation frequency f_{crit} of a plate the bending wavelength and the wavelength of the radiated sound have the same value. Below this frequency, the radiation efficiency is weak and consequently the decay factors α_m of the modes in this region are small. On the other hand, modes with eigenfrequencies above f_{crit} decay fast. This behaviour can be exploited to estimate the critical radiation frequency by computing average "decay factors" in different frequency regions.

For the developed characterization method, an average decay factor α_i will be determined for each frequency band i in a third-octave band spectrum, also called third-octave band decay factor spectrum. The α_i for this spectrum are estimated according to the same procedure applied for the modal decay factors α_m . However, instead of the Gaussian band-pass filter bank depicted in figure 44, a third-octave band filter bank according to the IEC 61260-1:2014 [28] standard is now used. Furthermore, the filter center frequencies do not depend on the extracted eigenfrequencies from the partial tracking algorithm. Exemplary results of third-octave band decay factor spectra from the synthesized and the real replica plate a_3 in figure 50 show, that the approximated critical frequencies of the plates are in the vicinity below the decay factor maximum. In fact, for all investigated synthesized plate sounds, the third-octave band below the maximum serves as a good approximation for f_{crit} . Assuming an isotropic plate,

$$f_{crit} = \frac{c_{air}^2}{\pi h} \sqrt{\frac{\rho}{E}} \sqrt{3(1 - \nu^2)} \quad (142)$$

depends on the material properties Young's modulus E , Poisson's ratio ν , the density ρ as well as the plate's thickness h .

The second analysis is carried out in the frequency region of the lowest detected eigenfrequencies from the partial tracking algorithm. As shown for the plate damping law from [9] in the sections 2.3.3 and 3.2, damping dominated by thermoelastic losses depends on the actual mode shapes and therefore shows an erratic behaviour. In contrast, laser vibrometer measurements with glass plates in [9] and in this work showed an almost constant linear increase of the decay factor, if the viscoelastic losses have a major influence for this material. Thus, quantifying the deviation of the decay factor from a hypothetical linear increase over frequency would provide an indicator for the material type of the plate. Considering equation 75, the associated slope would furthermore be an estimation of the material-inherent loss factor η via

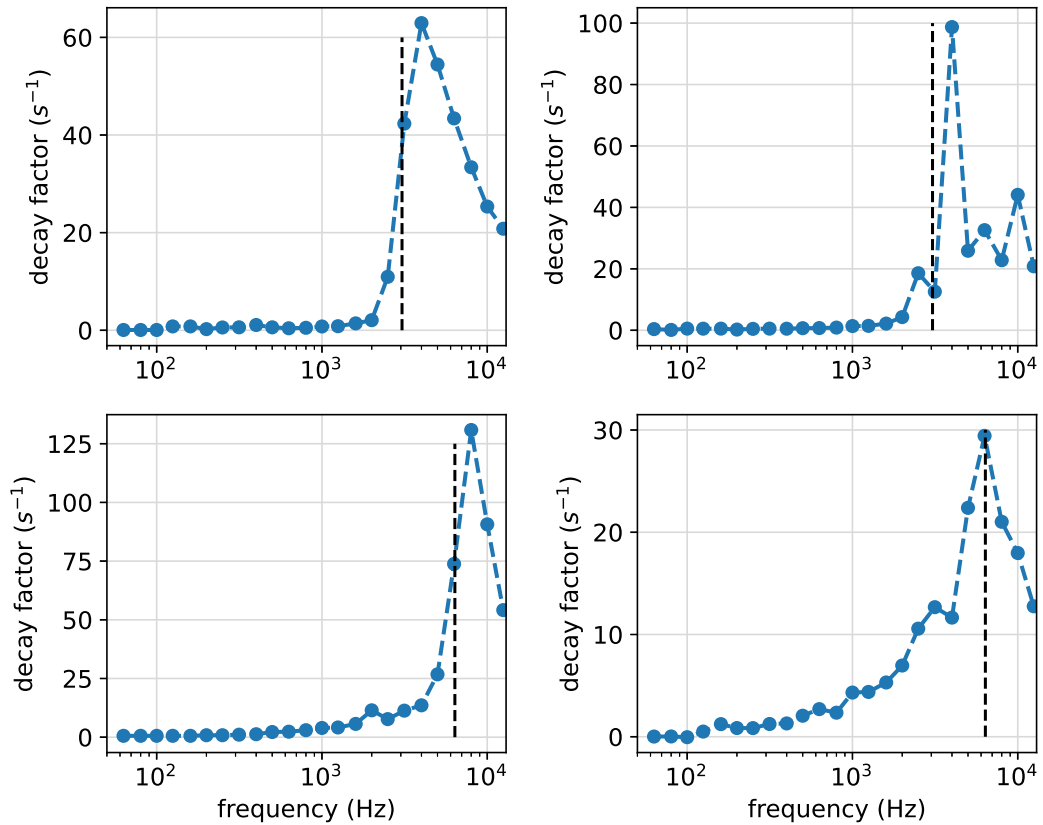


Figure 50 – Third-octave band decay factor spectrum (blue dots) and actual critical radiation frequency (black dashed line) determined from synthesized (left) and real (right) sound of the impacted replica aluminium plate a_3 (top) and the replica plate v_1 (bottom). For the real plate sounds, the actual critical frequencies are unknown and the duplicated frequencies from the synthesized plate solely serve as visual guidance.

$$\eta = \frac{2\alpha}{\omega}. \quad (143)$$

While the slope is simply determined from a linear regression, the deviation of the decay factors from the regression line is quantified by the coefficient of determination r^2 .

The regression analysis described above was carried out on synthesized and real sounds of all three replica plates listed in appendix C. Exemplary results of the aluminium plate a_3 and the glass plate v_1 are visualized in figure 51. As already shown with the laser vibrometer measurements in section 3.3, the decay factors for the aluminium plate show a more erratic behaviour, which results in a lower r^2 as for the investigated glass plate. Since the synthesized glass plate sound is based on the damping law in equation 99, the accurately extracted α_m are literally on the regression line. Even for the real glass plate sound, the r^2 of 0.945 is considerably higher than the coefficients of determination of the aluminium plates. Furthermore, the determined loss factors for glass are significantly larger than for the investigated aluminium plates and agree well with typical literature

Table 11 – Loss factors for bending waves for typical materials used for plates from [13] p. 191 and p. 196. *Data from [29].

material	loss factor η (-)
aluminium	$0.3 - 10 \cdot 10^{-5} / 2.2 - 7.7 \cdot 10^{-4}$ *
steel	$0.2 - 3 \cdot 10^{-4}$
glass	$0.6 - 2 \cdot 10^{-3}$
plexiglass	$2 - 4 \cdot 10^{-2}$
pressed wood panel	$1 - 3 \cdot 10^{-2}$

values listed in table 11. The estimated loss factors for the investigated aluminium plates are outside the value range for typical η mentioned in [13]. However, experiments carried out in [29] on aluminium with results also listed in table 11 show a better agreement with loss factors estimated from sounds of the synthesized and real aluminium replica plates.

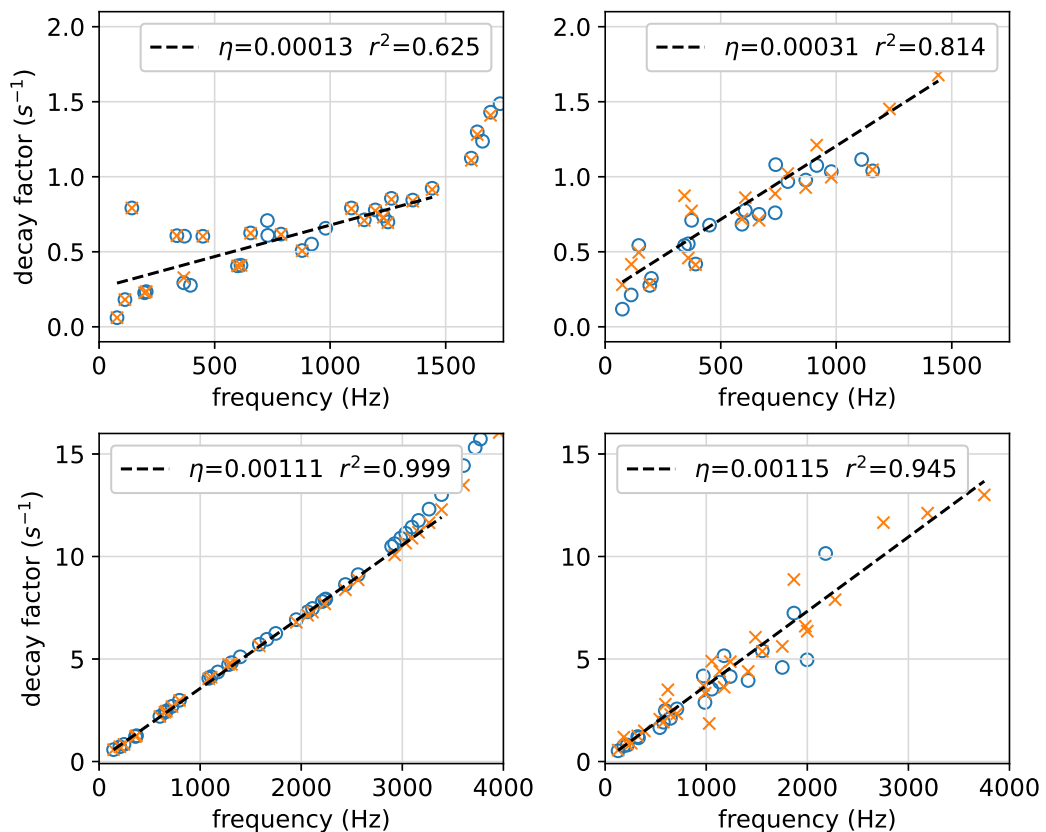


Figure 51 – Fitted regression line (black dashed line) for extracted (orange "x") decay factors from synthesized (left) and real (right) sound of the impacted replica plates a_3 (top) and v_1 (bottom). The actual decay factors (blue circles) of the real replica plates were determined from laser vibrometer measurements.

In summary, it can be stated that a regression analysis applied on accurately extracted decay factors from low modes can provide reasonable information about the construction material of the plate. For the investigated plate sounds, coefficients of determination close to one were obtained for glass plates. In combination with a determined internal loss factor η around 10^{-3} , this analysis provides a good hint that the material of the plate may be glass. A coefficient of determination below 0.9 in conjunction with a loss factor between 10^{-6} and 10^{-3} may indicate the material aluminium. Larger loss factors may be caused by materials with a strong viscoelastic damping, such as woods or plexiglass.

The third analysis for the acoustic characterization method does not utilize decay factors, but the extracted eigenfrequencies from the plate sound. Assuming an isotropic plate, the simplified frequency formula introduced in [7] and recapitulated in equation 68 can be rearranged to

$$f_{mn} = \underbrace{\frac{h\pi}{A} \sqrt{\frac{E}{\rho}} \sqrt{\frac{1}{48(1-\nu^2)}}}_{\Phi(h,A,\rho,E,\nu)} \underbrace{\sqrt{\left(G_x^4 \frac{1}{r_a^2} + G_y^4 r_a^2 + 2\nu H_x H_y + 2(1-\nu) J_x J_y \right)}}_{\text{depends on } \nu, r_a, m, n, BC}. \quad (144)$$

As annotated above, this equation consists of two parts. The first is characterized through the parameter Φ acting as a proportionality factor that depends on all material properties and the dimensions of the isotropic plate. The second part depends on ν , r_a and the boundary expressions G , H , J listed in table 5 and [7].

The aim is now to determine the most likely parameters for Φ and the plate aspect ratio r_a based on a limited number of extracted frequencies from the plate sound, which are labelled as f_i^* for this analysis. The Poisson's ratio is initially assumed as fixed with $\nu = 0.3$, since its value ranges from approximately 0.2 to 0.4 for most relevant materials used to construct plates. For a specific combination of boundary conditions and the associated integer mode numbers m and n , a set of values, dependent on the aspect ratio r_a and scaled by the parameter Φ , can be obtained with equation 144. These values are continuously referred to as the model frequencies f_j' of a hypothetical model plate with the parameter Φ' and the aspect ratio r_a' .

In order to find the closest values Φ_g and $r_{a,g}$ to the true values Φ and r_a of the plate, a steepest descent algorithm is applied for multiple meaningful initial value combinations for $\Phi'[0]$ and $r_a'[0]$. Within each run, the iterative algorithm moves along an error surface function. An exemplary error function is depicted in figure 52. For each iteration step k within a single run, a model plate with a new set of $\Phi'[k]$ and $r_a'[k]$ is chosen, and the resulting model frequencies $f_j'[k]$ are compared to the frequencies f_i^* . Since the number of extracted f_i^* is obviously smaller as the theoretically infinite number of model eigenfrequencies, every f_i^* is exclusively assigned to an f_j' by solving a linear assignment problem as described in section 4.1. The determination of the elements C_{ij} of the corresponding cost matrix \mathbf{C} has been defined with

$$C_{ij} = \frac{|f_i^* - f_j'[k]|}{f_i^*}. \quad (145)$$

Thus, minimizing the cost function as in equation 136 corresponds to an assignment of the extracted frequencies f_i^* to frequencies of the model plate that lead to the overall

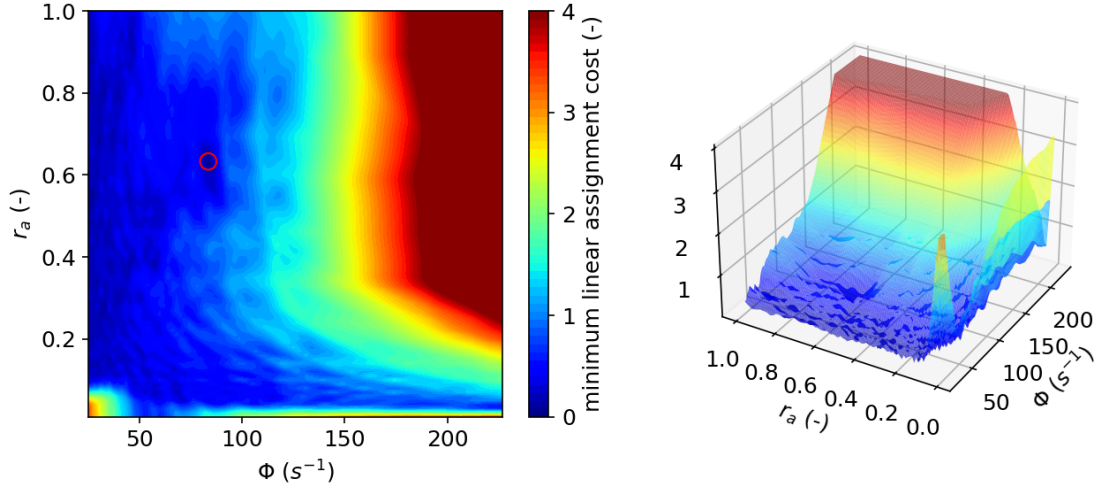


Figure 52 – Top view (left) and isometric view (right) of error function in dependence of Φ' , r'_a and location of true values Φ , r_a (red circle) for the synthesized aluminium replica plate a_1 . The linear assignment problem was solved with the 10 first eigenfrequencies, accurately extracted.

smallest relative frequency deviation for a value pair $\Phi'[k]$ and $r'_a[k]$. For the next iteration step $k + 1$ of the steepest descent algorithm, a new value pair Φ' and r'_a is selected according to

$$\Phi'[k + 1] = \Phi'[k] - \mu_{\Phi} \frac{\partial \min \left\{ \sum_I \sum_J C_{ij} X_{ij} \right\}}{\partial \Phi} \quad (146)$$

and

$$r'_a[k + 1] = r'_a[k] - \mu_{r_a} \frac{\partial \min \left\{ \sum_I \sum_J C_{ij} X_{ij} \right\}}{\partial r_a}, \quad (147)$$

where μ_{Φ} and μ_{r_a} are the associated learning rates. For appropriate learning rates and a sufficient number of iterations, each run of the steepest descent algorithm will converge to a local minimum on the error surface. The error surface in fact corresponds to the cost function minimum of the linear assignment problem in dependence of Φ' and r'_a . If multiple runs of the steepest descent algorithm are carried out with initial value combinations $\Phi'[0]$, $r'_a[0]$ positioned on a regular grid, runs with starting points near a local error function minimum will consistently converge to this same minimum. In areas densely covered with local minima, runs in this area will usually converge to different minima. Both cases are exemplary visualized in figure 53 for the aluminium replica plate a_3 .

After performing multiple runs of the steepest descent algorithm with initial value combinations $\Phi'[0]$, $r'_a[0]$ positioned on a regular grid, a histogram is computed over the found minima for all runs in terms of minimum linear assignment costs. As shown for ideally extracted eigenfrequencies from the synthesized plate in figure 53, the minimum found more than 50 times with the smallest linear assignment costs represents a good

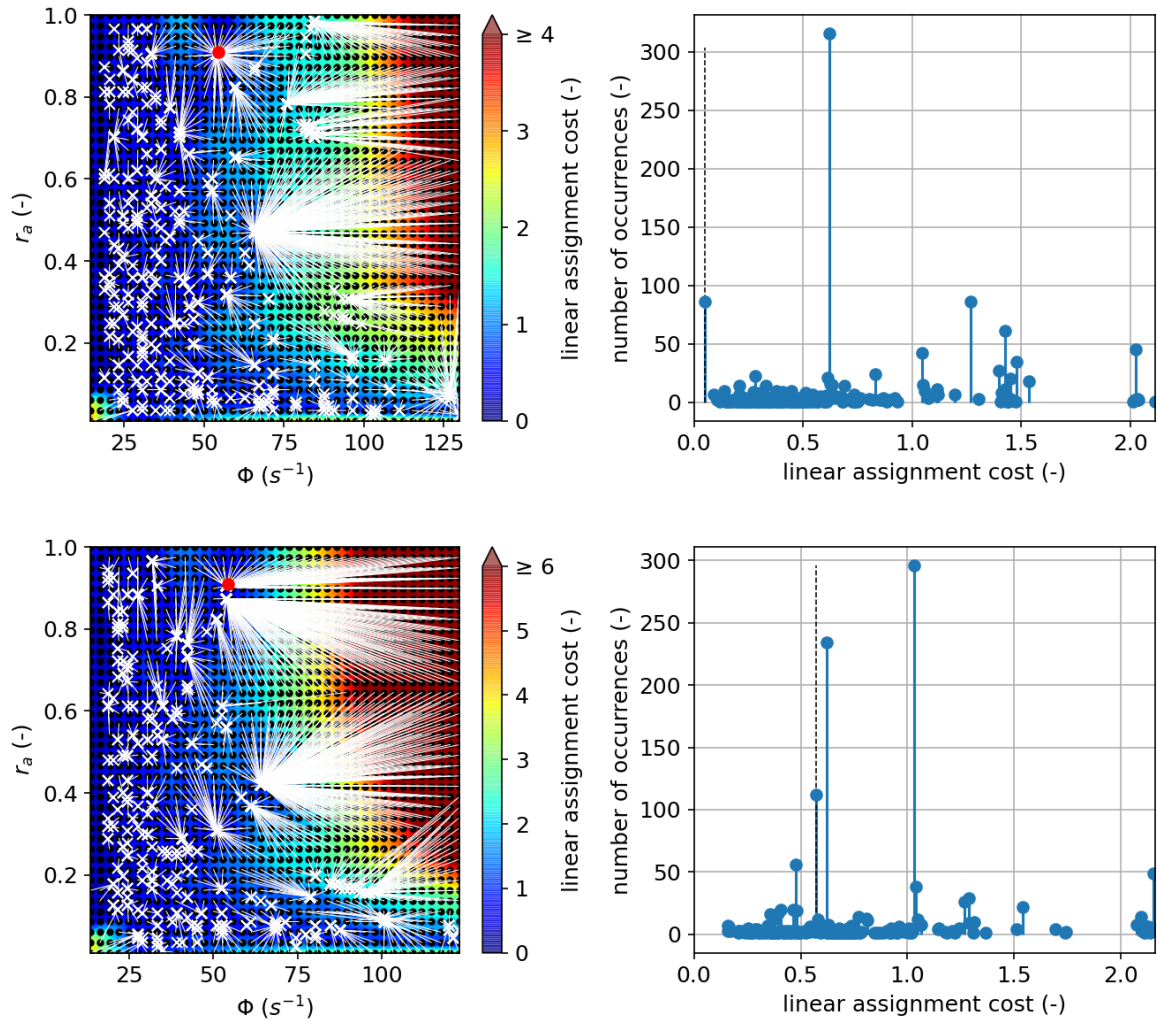


Figure 53 – Error functions (left) and true values (red dots) with steepest descent algorithm initial values (black dots) and connected end values (white "x"), and associated minimum linear assignment cost histograms (right) with best fit to true values (black dashed lines) for a synthesized (top) and a real (bottom) sound of the impacted replica plate a_3 . The linear assignment problems were solved with the 10 first eigenfrequencies, ideally extracted for the synthesized sound, and extracted with the procedure from section 4.1 for the real sound.

estimate $\Phi'_g, r'_{a,g}$ for the true value pair Φ, r_a of the plate. For the sound of the real impacted plate with extracted frequencies using the method from section 4.1, the results draw a similar picture, but not as unambiguously as for the synthesized plate sound. This can be mainly traced back to the eigenfrequencies of the real aluminium plate, which obviously differ from the ones predicted with equation 144. As shown in section 2.2 in figure 16, the resulting frequency error for square plates can be up to 13.5 % for the lowest modes and hence the linear assignment costs are generally larger as for the synthesized plate. However, the algorithm is still able to detect a local minimum close to the true value pair Φ, r_a . For all here discussed examples with the steepest descent

algorithm analysis, a restricted value range was assumed for the initial value $\Phi'[0]$. If the value range would be extended to large values, the linear assignment costs and subsequently the error function would simply increase further. However, an extension to smaller initial values of $\Phi'[0]$ corresponds to an increase of the modal density of the model plate. Hence, the limit case of a plate with an infinitely large modal density would always lead to a linear assignment with a cost of zero for the finite number of extracted frequencies f_i^* . Therefore, for the case studies described in the next section, a plausible lower limit for $\Phi'[0]$ was set based on an estimate of the modal density $D(f)$, which was simply computed as the inverse of the average frequency distance between two detected neighbouring eigenfrequencies.

4.3 Case Studies

Within this section, the developed acoustic characterization method for rectangular plates will be validated. To this end, multiple real and synthesized sounds of impacted plates and physical objects were recorded and created. These sounds include all plates described in appendix C and section 3.3 as well as virtual objects.

Real plates were recorded as described in section 3.3 and depicted in figure 40. All investigated real and synthesized objects for this validation and the associated characterization results are listed in table 12. Since measuring Young's modulus E and Poisson's ratio ν of real plates was out of scope of this work, average values computed from multiple text books values were employed for the elastic parameters. Besides the often mentioned materials glass and aluminium in previous sections of this work, the selection of objects also includes two plates from [9] made of spruce and carbon fibres. Sounds from plates consisting of the latter materials usually decay rapidly due to their inherent viscoelastic damping of bending waves. Consequently, the accurate extraction of eigenfrequencies and decay factors is significantly more challenging as for materials with weak material-inherent damping such as metals or glasses.

The performance of the acoustic characterization method was assessed with respect to multiple aspects. The first includes a comparison of the estimated loss factor η and the coefficient of determination r^2 obtained with the procedure described in section 4.2 with typical values ranges for the material from [13]. A best guess for the plate area A was made using the estimated critical radiation frequency f_{crit} and the aspect ratio with the procedures from the previous section.

The detected areas A and aspect ratios r_a for the isotropic synthesized aluminium and glass plates listed in table 12 show a good agreement with the corresponding true parameters. Furthermore, all estimated loss factors η of these plates are within plausible literature value ranges for the materials. For the real counterparts of the aluminium and glass plates, the determined loss factors are similar and are within the literature value ranges. However, the model plate fitting procedure with the steepest descent algorithm did not lead to a clear result for all investigated real plates. This could be traced back to the measured eigenfrequencies, which obviously differ from predicted eigenfrequencies with the underlying formula, given in equation 144. Nevertheless, if the model plate

fitting could find a clear best fit, the estimated aspect ratio r_a and subsequently the plate area A were close to the true values. For the investigated synthesized wooden plate, the estimated loss factor η is close to the given literature value. However, the model plate fitting did not succeed since the assumed orthotropy for the wooden plate leads to significantly different eigenfrequencies with equation 67 than with equation 144. The same issue occurred for the investigated synthesized plate sound of the plate made of carbon fibres.

Table 12 – Investigated objects for the validation of the acoustic characterization method. In every value cell, the first value represents the true value, the second the estimated value. *Represents or includes average data from text books. **Orthotropy assumed. Employed Young's modulus, Poisson's ratio and critical radiation frequency are geometric averages. \approx Ambiguous results, no estimation possible.

object	material	loss factor η (-)	loss factor coefficient of determination r^2 (-)	critical radiation frequency f_{crit} (KHz)	aspect ratio r_a (-)	Φ (s ⁻¹)	area A (m ²)
replica plate a1 synthesized	aluminium	2.2 - 7.7 · 10 ⁻⁴ * / 2.1 · 10 ⁻⁴	- / 0.33	6.00 / 6.30	0.63 / 0.62	83.5* / 79.3	0.059 / 0.059
replica plate a1 real	aluminium	2.2 - 7.7 · 10 ⁻⁴ * / 2.8 · 10 ⁻⁴	- / 0.43	- / 6.30	0.63 / 0.76	- / 78.48	0.059 / 0.059
replica plate a3 synthesized	aluminium	2.2 - 7.7 · 10 ⁻⁴ * / 1.3 · 10 ⁻⁴	- / 0.63	3.05 / 3.15	0.91 / 0.90	54.3* / 55.1	0.178 / 0.170
replica plate a3 real	aluminium	2.2 - 7.7 · 10 ⁻⁴ * / 3.1 · 10 ⁻⁴	- / 0.81	- / 3.15	0.91 / \approx	- / 54.5	0.178 / 0.171
replica plate v1 synthesized	glass	0.6 - 2 · 10 ⁻³ * / 1.1 · 10 ⁻³	- / 1.00	6.37 / 6.30	0.97 / 0.93	89.7* / 96.5	0.052 / 0.048
replica plate v1 real	glass	0.6 - 2 · 10 ⁻³ * / 1.2 · 10 ⁻³	- / 0.95	- / 5.00	0.96 / \approx	- / \approx	0.052 / \approx
plate c1 synthesized**	carbon fibres	- / 2.1 · 10 ⁻³	- / 0.33	6.37 / 8.00	0.50 / \approx	57.1 / \approx	0.08 / \approx
plate b1 synthesized**	spruce	\approx 8 · 10 ⁻³ / 7.6 · 10 ⁻³	- / 0.64	5.04 / 5.00	0.8 / \approx	27.52 / \approx	0.212 / \approx

5 Summary and Outlook

In this work, the acoustic characterization of rectangular plates was investigated. To this end, a comprehensive physical model to synthesize the sounds of impacted plates was implemented. By employing sounds synthesized from this model as well as sounds from real impacted plates, the acoustic characterization method developed within this work was validated.

The implemented modal synthesis model allows for control of the actual material-inherent properties and geometries of isotropic and orthotropic rectangular plates with different simple boundary conditions. With a developed Python interface to a FE framework, the model also offers the possibility to use more accurate mode shapes and eigenfrequencies obtained from FE simulations. Each part of the implemented model was validated with results from literature or own results obtained from conducted acoustic or laser vibrometer measurements. The comparison between synthesized sounds of exemplary impacted plates showed a good perceptive agreement with their real-life counterparts.

The second part of this work comprised the development of a method to detect the material properties and the plate geometry from sounds of impacted rectangular plates. Using both the estimated eigenfrequencies and decay factors as part of a simple signal model consisting of exponentially decaying sinusoids, three different analysis methods were developed to extract information from plate sounds. If the sound was rich in moderately decaying partials, the information was sufficient to provide a close estimate of the actual size and aspect ratio of the impacted plate. By computing the average material-inherent loss factor from the estimated decay factors, the determination of the most likely material was possible for the investigated plates.

Considering the results from listening experiments about the identification of physical properties from plates and bars from [17], [10] and [15], the results from the present work prove that an algorithmic acoustic detection of the properties of rectangular plates can be superior to the estimation of these properties carried out by an average human auditory system. However, the validation of the developed acoustic characterization method revealed several aspects that could be improved in future work:

- In its current state, the characterization method assumes a rectangular plate with free edges. Since the underlying frequency formula from [7] for the model plate fitting procedure also considers different boundary conditions, a next investigation step could be the distinction between different boundary conditions.
- In order to distinguish between more different construction materials for plates, a comprehensive database of material-inherent loss factors would significantly improve the acoustic characterization method. The data in [13] provides a basis, but own laser vibrometer measurements from this work and results from [29] reveal the potential to refine value ranges for different materials.
- The extraction of eigenfrequencies and decay factors forms the basis for all further analysis steps in the acoustic characterization method. The detection and tracking of prominent frequencies in a signal as well as the decay determination of a mode are each a research topic in their own right [26] [36]. Thus, improving the accuracy

of the extraction methods for these parameters would subsequently increase the potential for a more accurate acoustic characterization of rectangular plates.

- In its current state, the performance of the acoustic characterization method decreases for objects that are more bar- than plate-shaped. This could be attributed to the more erratic behaviour of the decay factors caused by the material-inherent thermoelastic or viscoelastic losses. Furthermore, the smaller modal density of bar-shaped objects leads to more ambiguous results for the aspect ratio and area estimation with the developed model plate fitting procedure. However, taking the modal density of bar-shaped objects more precisely into account could overcome these problems.

A Derivations of Equations Regarded to Thin Rectangular Plates

A.1 Potential Energy in a Vibrating Plate

According to [7], the potential energy E_{pot} and the mechanical energy E_{kin} in a thin plate are

$$E_{pot} = \int_0^{L_y} \int_0^{L_x} \frac{1}{2} \frac{Eh^3}{12(1-\nu^2)} \left[\left(\frac{\partial^2 W}{\partial x^2} \right)^2 + 2\nu \frac{\partial^2 W}{\partial x^2} \frac{\partial^2 W}{\partial y^2} + \left(\frac{\partial^2 W}{\partial y^2} \right)^2 + 2(1-\nu) \left(\frac{\partial^2 W}{\partial x \partial y} \right)^2 \right] dx dy, \quad (148)$$

where W is the transverse vibration of the plate. In order to have a consistent notation with [9], the four rigidity constants D_1 to D_4 are introduced into the above equation, as in [31]. While for D_1 , D_2 and D_3 this is a straight-forward procedure, in case of D_4 the identity

$$\frac{1-x}{1-x^2} = \frac{1}{1+x} \quad \text{for } x \neq 1 \quad (149)$$

must be applied. The resulting expression

$$E_{pot} = \frac{h^3}{2} \int_0^{L_y} \int_0^{L_x} \left[D_1 \left(\frac{\partial^2 W}{\partial x^2} \right)^2 + D_2 \frac{\partial^2 W}{\partial x^2} \frac{\partial^2 W}{\partial y^2} + D_3 \left(\frac{\partial^2 W}{\partial y^2} \right)^2 + D_4 \left(\frac{\partial^2 W}{\partial x \partial y} \right)^2 \right] dx dy \quad (150)$$

is valid for orthotropic thin plates and is equivalent to equation 1 in [31].

A.2 Eigenfrequencies of an Orthotropic Plate

Various literature sources like [7], [5] and [12] contain simple formulas to determine the eigenfrequencies of a thin isotropic or orthotropic plate. However, none of them present a simple formula to calculate the eigenfrequencies of an orthotropic plate for any combination of free, clamped or simply supported edges. The following derivation is based on considerations from Marian Weger.

According to [7] equation 15 and 16, the approximate angular eigenfrequency ω_{mn} can be determined with

$$\omega_{mn} = \frac{2\pi^2 h}{L_x^2} \sqrt{\frac{E}{48\rho(1-\nu^2)}} \sqrt{G_x^4 + G_y^4 \frac{L_x^4}{L_y^4} + \frac{2L_x^2}{L_y^2} [\nu H_x H_y + (1-\nu) J_x J_y]}. \quad (151)$$

By incorporating the expression $\sqrt{\frac{E}{12(1-\nu^2)}}$ into the dimensionless frequency factor, one can include the well-known rigidity constants D_1 to D_4 but for an isotropic plate to obtain

$$\omega_{mn} = \frac{\pi^2 h}{\sqrt{\rho} L_x^2} \sqrt{D_1 G_x^4 + D_3 G_y^4 \frac{L_x^4}{L_y^4} + D_2 \frac{L_x^2}{L_y^2} H_x H_y + D_4 \frac{L_x^2}{L_y^2} J_x J_y}. \quad (152)$$

If now the length L_x is rearranged in the equation, the result

$$\omega_{mn} = \frac{\pi^2 h}{\sqrt{\rho}} \sqrt{D_1 \frac{G_x^4}{L_x^4} + D_3 \frac{G_y^4}{L_y^4} + D_2 \frac{H_x H_y}{L_x^2 L_y^2} + D_4 \frac{J_x J_y}{L_x^2 L_y^2}} \quad (153)$$

has the same form as the eigenfrequencies of a simply supported orthotropic plate given in [5], equation 3.157. Note that the rigidity constants in [5] already include the factor h^3 . Since an orthotropic plate has the same mode shapes as an isotropic plate, the coefficients for G , H and J derived by Warburton can also be used in the above equation. By using the rigidity constants D_1 to D_4 but for an orthotropic plate, equation 153 makes it possible to determine the eigenfrequencies of an orthotropic plate for any boundary for combination of free, clamped and simply supported edges.

A.3 Frequency Correction for Square Modes of a Free Plate

If the aspect ratio of a rectangular plate with all edges free approaches one, the elastic interaction between mode pairs of the type $\{m, n\}$ and $\{n, m\}$, where $m - n$ is a non-zero even number, influences the eigenfrequencies of these modes. As described in [12], Poisson coupling for the mixed mode $\{m, n\} + \{m, n\}$ increases and the added stiffness for the mixed mode $\{m, n\} - \{n, m\}$ decreases the eigenfrequency compared to the eigenfrequency obtained from equation 67 without elastic interaction. Therefore, Warburton introduced in [7] a correction factor $\Delta\kappa_{sq}$ that is added to the non-dimensional frequency factor κ according to

$$\kappa_{sq\pm}^2 = \kappa^2 \pm \Delta\kappa_{sq}^2, \quad (154)$$

whereas κ is defined in equation 69. For bar-mode-shaped mode pairs of the type $\{m, 0\} \pm \{0, m\}$ with $m = 2, 4, 6, \dots$, this correction factor is

$$\Delta\kappa_{sq}^2 = \pm 2\nu G_x^2 \frac{8}{\pi^2}. \quad (155)$$

Twisting mode pairs of the form $\{m, 1\} \pm \{1, m\}$ with $m = 3, 5, 7, \dots$ include the factor

$$\Delta\kappa_{sq}^2 = \pm 4\nu J_y \frac{H_x^2}{G_x^2} \pm 2(1 - \nu) J_y^2 \frac{4}{3}. \quad (156)$$

For all remaining mode pairs where Poisson coupling and an added stiffness influences the eigenfrequency, the pairs of the type $\{m, n\} \pm \{n, m\}$ with $m > 1$ and $n > 1$, the

correction factor is

$$\Delta\kappa_{sq}^2 = \pm \frac{16\nu}{\pi^2} [G_x^4(A+B)^2 + G_y^4(A-B)^2] \\ \pm \frac{32(1-\nu)}{\pi^2} G_x^2 G_y^2 (A+C)^2.$$

For this case, the factors A , B and C are given by

$$A = \frac{1}{G_x + G_y}, \quad B = \frac{G_x - G_y}{G_x^2 + G_y^2}, \quad C = \frac{G_x + G_y}{G_x^2 + G_y^2}. \quad (157)$$

Note that the frequency coefficients G , H and J for free edges are listed in table 5 and furthermore available in [7].

B Modal Densities of Selected Objects

In order to use the modal density as information to detect the shape and material properties of simple objects, this section includes the derivation of the modal density of selected objects. For this purpose, we define the number of modes $N(k)$ below the wavenumber k , as in [32]. The statistical modal density $D(f)$ as the number of modes per hertz can be determined with

$$D(f) = \frac{dN(f)}{df}, \quad (158)$$

where $N(f)$ is the number of modes with eigenfrequencies lower than the frequency f . Another mathematically equivalent definition of the statistical modal density that includes the wave speed c is

$$D(f) = \frac{2\pi}{c} \frac{dN(k)}{dk}. \quad (159)$$

This equation will be used to derive the modal density of bars in the next subsection.

B.1 Thin Bars

As stated in [33], the wavelength of a 1-dimensional mode with the number n is given as

$$\lambda_n = \frac{2L}{n + \delta_{BC}}, \quad (160)$$

with δ_{BC} being a factor between $0 \leq |\delta_{BC}| \leq 1$ that depends on the boundary conditions of the system. Approximate values for these factors are listed in table 13 for various boundary conditions of a bar. Based on the wavelengths, the corresponding wavenumbers k_n are given by

$$k_n = (n + \delta_{BC}) \frac{\pi}{L}. \quad (161)$$

Rearranging this equation to $n = N(k)$ and inserting it into equation 159, the modal density of a thin bar can be derived to

$$D(f) = \frac{2L}{c}. \quad (162)$$

Note that this density is independent of the boundary conditions and is furthermore proportional to $1/\sqrt{f}$ for bending waves, considering their speed of

$$c = \sqrt{2\pi f K c_L}. \quad (163)$$

In contrast to the modal density, the number of modes $N(f)$ below a certain frequency does depend on the boundary condition and can be derived to

$$N(f) = \sqrt{\frac{2\pi f L}{K c_L}} \frac{L}{\pi} - \delta_{BC}. \quad (164)$$

Table 13 – Approximate factors for δ_{BC} for a bar with both ends free (ff), one end clamped and one end free (cf), and both ends simply supported (ss).

bc	δ_{BC}
ff	1/2
cf	-1/2
ss	0
cc	1/2
cs	1/4

C Investigated Plates

This appendix contains detailed information about the main investigated plates in this work. In order ensure comparability with literature results, these plates were the two aluminium plates a_1 and a_3 as well as the glass plate v_1 from [9]. For the execution of own acoustic and laser vibrometer measurements, these three plates were replicated and are shown in figure 54 and figure 57. Table 14 contains the corresponding dimensions and materials parameters of the replica plates as well as of the literature plates. Note that due to manufacturing tolerances, the properties of the replica plates are slightly different than the parameters of the plates from [9].

For the particular validation step of the overall synthesis model with the literature results from [18], a different aluminium plate was investigated. The corresponding characteristics of this plate are listed in table 15.

Table 14 – Dimensions and material properties of the investigated plates. In every cell, the first value corresponds to the value of the literature plate, the second to the replica plate. *No data available from literature source, but can be derived from measured rigidity constants. **In [9], rounded value of 2.0 mm is listed.

	plate a_1	plate a_3	plate v_1
material type	aluminium		glass
length L_x (m)	0.304 / 0.305	0.4195 / 0.442	0.2295 / 0.231
length L_y (m)	0.192 / 0.193	0.400 / 0.402	0.2205 / 0.223
thickness h (mm)	2.0 / 2.0	4.0 / 3.9	2.1** / 1.9
density ρ (kg / m ³)	2660 / 2633	2660 / 2599	2550 / 2434
Young's modulus E (GPa)		* / -	* / -
Poisson's ratio ν (-)		* / -	* / -
rigidity constant D_1 (MPa)		6160 / -	6700 / -
rigidity constant D_4 (MPa)		8600 / -	10270 / -



Figure 54 – Aluminium replica plate a_3 (left) and glass replica plate v_1 (right).

Table 15 – Dimensions and material properties of the investigated plate from [18]. *No data available from literature source. Instead, average values from text books are listed that were used for the validation of the synthesis model.

	plate a ₂
material type	aluminium
length L_x (m)	0.405
length L_y (m)	0.325
thickness h (mm)	3.0
density ρ (kg / m ³)	2660*
Young's modulus E (GPa)	69*
Poisson's ratio ν (-)	0.3*

D FE Simulation Framework and its Validation

Finite element (FE) simulations were employed in multiple parts of this work. All investigated plates and bars were simulated with the open source software Elmer³. With the SmitcSolver [34], Elmer provides a practical routine to determine the eigenfrequencies and mode shapes of rectangular-shaped objects. The underlying Mindlin–Reissner plate theory is an extension of the Kirchhoff–Love plate theory that takes also the potential effect of out-of-plane shear forces \mathcal{T}_z into account. Subsequently, cross sectional areas that were normal to the out-of-plane axis before deformation are not necessarily normal to the axis after deformation. However, if the plate’s thickness h is significantly smaller than the bending wavelengths the Mindlin–Reissner plate model represents a penalty approximation of the Kirchhoff–Love plate theory.

Within this work, a simple application programming interface (API) has been written in the programming language Python for the Elmer SmitcSolver. This API enables the determination of mode shapes and the associated eigenfrequencies of isotropic rectangular plates with FE simulations using Python. Internally, the API carries out the same procedures as described in [35]. Note that a detailed study of the underlying theory of FE models and simulations was out of scope of this work.

In order to validate the SmitcSolver of Elmer, multiple tests with plates and bars under different conditions were carried out within this work. Here, the results of the most obvious test case, a plate simply supported on all edges, is presented. Figure 55 shows the relative difference between the simulated dimensionless frequency factor κ and the exact results from the analytic solution for different numbers of finite elements N_x and N_y in the corresponding x - and y -direction of the plate. The larger increase for small numbers of N_x and N_y can be attributed to the insufficient number of elements used for the simulations. As stated in numerous text books on FEM, at least 6 to 10 elements should be considered per wavelength of the mode shape. However, if this rule of thumb is fulfilled, simulated and analytically determined eigenfrequencies show a very good agreement.

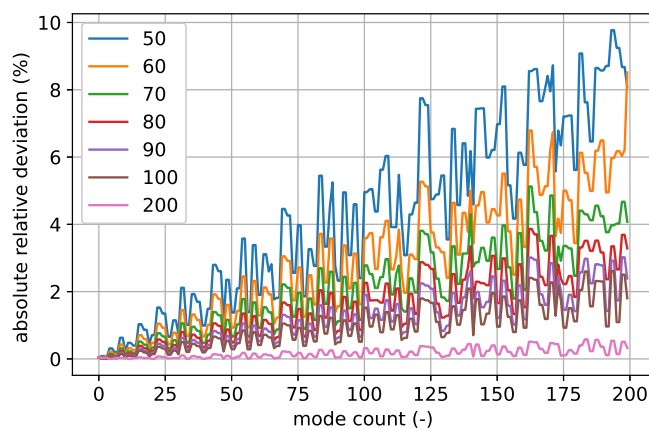


Figure 55 – FE simulation validation for various numbers of elements in each plate dimension for a simply supported plate.

3. freely available at www.elmerfem.org

E Laser Vibrometer Measurements

In order to determine the modal decay factors α_{mn} for the investigated plates listed in appendix C, laser vibrometer measurements were carried out in this work. The employed measurement procedure was heavily inspired by the approach described in [9]. As visualized in figure 56, the measurement setup consisted of a laser vibrometer of the type Polytec RSV-150 in front of a suspended free plate. The plate suspension device was built similarly to the device described in [16] and is shown in figure 57. For potentially reproducing the decay factor measurement results in [9], the investigated plates were also suspended with a nylon tread of 0.4 mm diameter. The necessary holes for the suspension and the twisting prevention were drilled near the plate edges at $L_x/2$ and $L_y/2$.

The plate under investigation was acoustically excited by a loudspeaker fed with a sine wave from a signal generator. For each mode, the signal frequency was adjusted to the corresponding value of the presimulated eigenfrequency from FE simulations of the plate. The measurement position of the laser vibrometer was adjusted to a maximum of the presimulated mode shape while also considering nodes of modes that may significantly overlap with the current mode in terms of their frequency responses. Then a fine tuning of the signal frequency was carried out until the magnitude of the monitored velocity signal from the laser vibrometer indicated a local maximum. The found frequency was recorded as the measured actual eigenfrequency for the presimulated mode.

For estimating the decay factor α of a mode, the excitation signal tuned to the eigenfrequency was suddenly turned off and the decay of the velocity signal $v(t)$ from the laser vibrometer was recorded. The signal envelope $E(t)$ was then estimated using

$$E(t) = |v(t) + jH\{v(t)\}|, \quad (165)$$

where $H\{\}$ denotes the Hilbert transform. Assuming an extracted exponential decay of the form $E(t) = E_0 e^{-\alpha t}$, the conversion to

$$\ln(E(t)) = -\alpha t + \ln(E_0). \quad (166)$$

leads to a linear decrease with the slope $-\alpha$. In practice, this slope served as estimation for the decay factor, determined from the measurement data with a simple linear regression, as exemplary depicted in figure 58.

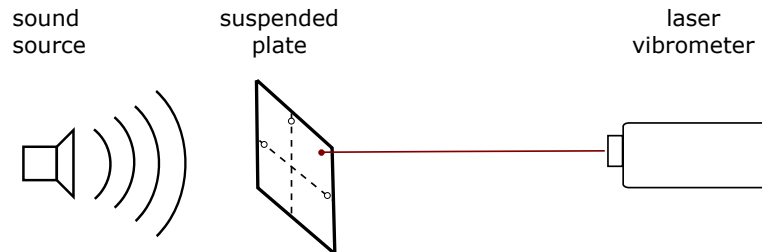


Figure 56 – Laser vibrometer measurement setup.



Figure 57 – Laser vibrometer measurements (left) and built plate suspension device with aluminium replica plate a_1 (right).

Table 16 – Device list for laser vibrometer measurements. *Served as signal generator, real-time oscilloscope and data recorder.

device	manufacturer	type	remark
loudspeaker	JBL (chassis)	-	custom-made
laser vibrometer	Polytec	RSV-150	-
vibrometer controller	Polytec	RSV-150	-
lens	Polytec	RSV-A-261 f2610	-
audio sound card	Focusrite	Clarett 4Pro USB	-
MacBook Pro*	Apple	13 inch, late 2011	-
audio power amplifier	Bruel and Kjaer	2716C	-

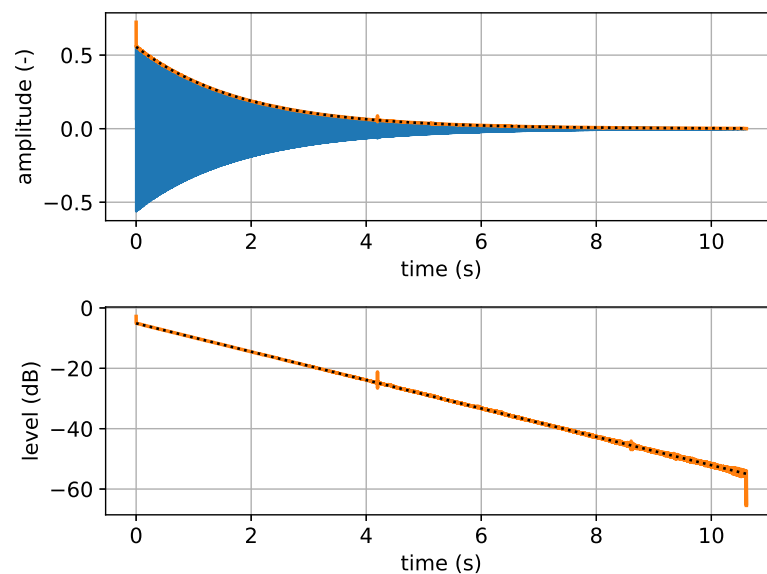


Figure 58 – Top: exemplary recorded velocity signal (blue), determined analytic envelope (orange) and estimated envelope from regression analysis (black). Bottom: linear regression (black) of logarithmic envelope (orange).

References

- [1] C. Steele, C. Balch, *"Introduction to the Theory of Plates"* 2009: Stanford University, Lecture Notes.
- [2] N. Fletcher, T. Rossing, *"The Physics of Musical Instruments"* 1998: 2nd Edition, Springer Verlag.
- [3] J. Wandinger, *"Balkenschwingungen"* 2007: lecture notes on course Elastodynamik 2, available online http://wandinger.userweb.mwn.de/LA_Elastodynamik_2/kap_3_balken.pdf.
- [4] R. Lyon, R. DeJong, *"Theory and Application of Statistical Energy Analysis"* 1995: 2nd Edition, Butterworth-Heinemann.
- [5] A. Chaigne, J. Kergomard, *"Acoustics of Musical Instruments"* 2016: Springer Verlag.
- [6] A. Leissa, *"Vibration of Plates"* 1969: National Aeronautics and Space Administration.
- [7] G. Warburton, *"The Vibration of Rectangular Plates"* 1954: Proceedings of the Institution of Mechanical Engineers, Sage.
- [8] A. Chaigne, V. Doutaut, *"Numerical simulations of xylophones. I. Time-domain modelling of the vibrating bars"* 1997: The Journal of the Acoustical Society of America, Vol. 101, pp. 539 - 557.
- [9] A. Chaigne, C. Lambourg, *"Time-domain simulation of damped impacted plates, I. Theory and experiments"* 2001: The Journal of the Acoustical Society of America, Vol. 109, pp. 1422 - 1432.
- [10] S. McAdams, A. Chaigne, *"The psychomechanics of simulated sound sources: Material properties of impacted bars"* 2004: The Journal of the Acoustical Society of America, Vol. 115, pp. 1306 - 1320.
- [11] M. Aramaki, M. Besson, *"Controlling the Perceived Material in an Impact Sound Synthesizer"* 2010: IEEE Transactions on Audio, Speech and Language Processing, Vol. 19, No. 2, pp. 301 - 314.
- [12] T. Rossing, *"Springer Handbook of Acoustics"* 2014: Springer Verlag.
- [13] L. Cremer, M. Heckl, *"Structure-Borne Sound"* 2005: Springer Verlag.
- [14] M. Möser, *"Technische Akustik"* 2012: 9th Edition, Springer-Vieweg.
- [15] S. McAdams, V. Roussarie, *"The psychomechanics of simulated sound sources: Material properties of impacted thin plates"* 2010: The Journal of the Acoustical Society of America, Vol. 128, pp. 1401 - 1413.
- [16] B.L. Giordano, S. McAdams, *"Material identification of real impact sounds: Effects of size variation in steel, glass, wood, and plexiglass plates"* 2006: The Journal of the Acoustical Society of America, Vol. 119, pp. 1171 - 1181.
- [17] R.L. Klatzky et al., *"Perception of material from contact sounds"* 2000: Presence in Teleoperators and Virtual Environment, Vol. 9, pp. 399 - 410.

- [18] P. Troccaz, R. Woodcock, "*Acoustic radiation due to the inelastic impact of a sphere on a rectangular plate*" 2000: Journal of the Acoustical Society of America, Vol. 109, No. 5, Part 1, pp. 2197 - 2202.
- [19] E. Williams, "*Numerical evaluation of the radiation from unbaffled, finite plates using the FFT*" 1983: The Journal of the Acoustical Society of America, Vol. 74, pp. 343 - 347.
- [20] A. Putra, D.J. Thompson, "*Sound radiation from rectangular baffled and unbaffled plates*" 2010: Applied Acoustics, Vol. 71, pp. 1113 - 1125.
- [21] R.J. McAulay, T.F. Quatieri, "*Speech Analysis / Synthesis Based on a Sinusoidal Representation*" 1986: IEEE Transactions on Acoustics, Speech, and Signal Processing, Vol. 34, No. 4, pp. 744 - 754.
- [22] M. Lagrange et al., "*Tracking Partial for the sinusoidal Modeling of polyphonic Sounds*" 2005: IEEE Transactions on Acoustics, Speech, and Signal Processing, Vol. 3, pp. 229 - 232.
- [23] M. Czuka, "*Development of an analysis method for the extraction of sound synthesis parameters from driving noise of motor vehicles*" 2014: Audio Engineering Student Project, Austria.
- [24] K. Fitz, L. Haken, "*Bandwidth enhanced sinusoidal modelling in Lemur*" 1995: Proceedings of the International Computer Music Conference, pp. 154 - 157, Canada.
- [25] X. Serra, J.O. Smith, "*Spectral modeling synthesis: a sound analysis / synthesis system based on a deterministic plus stochastic decomposition*" 1990: Computer Music Journal, Vol. 14, No. 4, pp. 12 - 24.
- [26] J. Neri, P. Depalle, "*Fast Partial Tracking of Audio with real-time Capability through linear programming*" 2018: Proceedings of the 21st International Conference on Digital Audio Effects, pp. 326 - 333, Portugal.
- [27] D. Hale, "*Recursive Gaussian filters*"
- [28] International Electrotechnical Commission, "*IEC 61260-1:2014 - Electroacoustics - Octave-band and fractional-octave-band filters - Part 1: Specifications*" 2014.
- [29] J. Åberg, "*On the Experimental Determination of Damping of Metals and Calculation of Thermal Stresses in Solidifying Shells*" 2006: Doctoral Thesis, Sweden.
- [30] M. Aramaki, M. Besson, "*Controlling the Perceived Material in an Impact Sound Synthesizer*" 2011: IEEE Transactions on Audio, Speech, and Language Processing, Vol. 19, No. 2, pp. 301 - 314.
- [31] M. McIntyre, J. Woodhouse, "*On Measuring the Elastic and Damping Constants for orthotropic Sheet Materials*" 1988: Acta Metallurgica, Vol. 35, No. 6, pp. 1397 - 1416.
- [32] C. Hopkins, "*Sound Insulation*" 2007: 1st Edition, Butterworth-Heinemann.
- [33] R. Lyon, R. DeJong "*Theory and Application of statistical Energy Analysis.*" 1995: 2nd Edition, Butterworth-Heinemann.
- [34] P. Råback, M. Malinen, "*Elmer Models Manual*" May 29 2019.
- [35] CSC - IT Center for Science, "*Elmer GUI Tutorials*" December 19 2018.
- [36] J. Balint, "*Evaluating the decay of sound*" 2020: PhD thesis, Austria.

List of Figures

1	Schematic principle of acoustic detection and the developed acoustic characterization method within this work.	11
2	Geometry and Euler-Bernoulli kinematics of a rectangular bar.	14
3	Typical boundary conditions for a bar.	15
4	First four bending mode shapes on a bar with free ends.	16
5	First four bending mode shapes on a cantilever bar.	18
6	First four bending mode shapes on a bar with hinged ends.	19
7	Bending mode eigenfrequencies for different boundary conditions and bar properties.	20
8	Comparison between mode shapes for different boundary conditions. . . .	21
9	Geometry of a rectangular plate.	23
10	Top view of selected boundary conditions of a rectangular plate.	25
11	Exemplary normalized mode shapes of a rectangular plate with simply supported edges.	26
12	Exemplary vibrational mode shapes of a rectangular plate with free edges according to Warburton.	27
13	Nodal patterns for the mode shapes $\{2, 0\} + \{0, 2\}$ and $\{2, 0\} - \{0, 2\}$ for different aspect ratios of a free plate after Warburton.	28
14	Exemplary normalized mode shapes of a cantilever plate according to Warburton.	29
15	Eigenfrequencies of a rectangular plate with simply supported and free edges.	32
16	Variation of frequency factor for a free plate with different aspect ratios and mode numbers.	32
17	Ascending eigenfrequencies for a steel plate with different boundary conditions and aspect ratios.	33
18	Temperature distribution in a bent plate.	35
19	Stress-strain relation for pure elastic deformation and linear viscoelastic deformation.	35
20	Predicted decay factors of a free isotropic aluminium plate from [9]. . . .	40
21	Damping law of a free isotropic glass plate from [9].	40
22	Contact of a sphere with an infinite rigid plane and resulting interaction force.	41
23	Conphase vibrating plane described with two monopole sources and corresponding geometric setup.	43

24	Vibrating plate in an infinite baffle and sound pressure evaluated at a large distance.	44
25	Acoustic shortcut for a 1-dimensional bending wave.	45
26	Steps involved in the implemented physical sound synthesis model. . . .	47
27	Magnitude and phase response of a damped mass-spring system.	48
28	Geometric setup of the Troccaz synthesis model and the implemented modal synthesis model.	50
29	Steps involved in the implemented physical sound synthesis model. . . .	51
30	Schematic displacement on a vibrating plate and slicing of plate into rectangular surface elements.	52
31	Temporal progression and magnitude spectrum of the impact force for a rubber mallet with a piano impact and a mezzo-forte impact.	54
32	Temporal progression and magnitude spectrum of the impact force for a boxwood mallet with a piano impact and a mezzo-forte impact.	55
33	Comparison between synthesis model mode shapes and shapes obtained from FE simulations for a square plate.	56
34	Basic information of investigated plates.	57
35	Comparison between eigenfrequencies from implemented Warburton method, FE simulations, and measured eigenfrequencies from Chaigne for the aluminium plate a_3 and the glass plate v_1	58
36	Comparison between decay factors from Chaigne [9], own measurements and implementation for the aluminium plate a_1	59
37	Comparison between decay factors from Chaigne [9], own measurements and implementation for the glass plate v_1	61
38	Interaction force of an elasto-plastic impact of a steel sphere with the investigated aluminium plate from Troccaz.	62
39	Comparison between sound pressure of own implemented model, simulated and measured results from Troccaz for observation points located center and off-center from the plate.	62
40	Acoustic measurement setup.	63
41	Spectrograms and magnitude spectra of the synthesized and real sound of the impacted replica plate a_1 at the observation position of mic 1. . . .	64
42	Sketch of assumed acoustic identification situation and simplified setup for the developed acoustic characterization method.	65
43	Overview of the acoustic characterization method.	66
44	Overview of the steps involved in the estimation of the eigenfrequencies and decay factors.	67

45	Illustration of a basic linear assignment problem and the associated cost matrix C	68
46	Spectrogram and extracted partials of the synthesized and real sound of the impacted replica plate a_3	69
47	Frequency responses of designed Gaussian band-pass filters with $G_{dB} = -40$ dB and magnitude spectrum of the synthesized sound of the impacted replica plate a_3	70
48	Band-pass filtered signal, determined analytic envelope and estimated envelope from regression analysis of a real sound of the impacted replica plate a_3 . Corresponding linear regression of logarithmic envelope.	71
49	Actual and extracted decay factors from synthesized and real sound of the impacted replica plate a_3	71
50	Third-octave band decay factor spectrum and actual critical radiation frequency determined from synthesized and real sound of the impacted replica aluminium plate a_3 and the replica plate v_1	73
51	Fitted regression line for extracted decay factors from synthesized and real sound of the impacted replica plates a_3 and v_1	74
52	Top and isometric view of error function in dependence of Φ' , r'_a and location of true values Φ , r_a for the synthesized aluminium replica plate a_1	76
53	Error functions and true values with steepest descent algorithm initial values, connected end values and associated minimum linear assignment cost histograms with best fit to true values for a synthesized and a real sound of the impacted replica plate a_3	77
54	Aluminium replica plate a_3 and glass replica plate v_1	89
55	FE simulation validation for various numbers of elements in each plate dimension for a simply supported plate.	91
56	Laser vibrometer measurement setup.	93
57	Laser vibrometer measurements and built plate suspension device with aluminium replica plate a_1	94
58	Exemplary recorded velocity signal, determined analytic envelope and estimated envelope from regression analysis. Linear regression of logarithmic envelope.	94

List of Tables

1	Normalized eigenfrequencies, normalized wavelengths, nodal positions and allowed $k_n L$ for the first four bending modes of a bar with free ends.	17
2	Normalized eigenfrequencies, normalized wavelengths, nodal positions and allowed $k_n L$ for the first four bending modes of a bar with one clamped and one free end.	18
3	Normalized eigenfrequencies, normalized wavelengths and nodal positions for the first four bending modes of a bar with simply supported ends. . .	19
4	Boundary condition dependent expressions for a bar with free ends, clamped ends, one clamped and one free end.	22
5	Coefficients to determine the eigenfrequencies of a rectangular plate in single dimension for the boundary conditions free-free edges, simply supported edges and clamped-free edges.	31
6	Thermal constants heat capacity, thermal expansion coefficient and thermal conductivity for typical materials from [5].	37
7	Viscoelastic parameters measured in [9].	38
8	Viscous constants for typical materials from [9].	38
9	Model parameters for Hertz's law of contact for a mallet with a rubber and a boxwood head for a piano and a mezzo-forte impact.	53
10	Parameters and material properties used to synthesize the sound of the aluminium replica plate a_1	63
11	Loss factors for bending waves for typical materials used for plate construction from [13].	74
12	Investigated objects for the validation of the acoustic characterization method.	80
13	Approximate factors for δ_{BC} for a bar with both ends free, one end clamped and one end free, and both ends simply supported.	88
14	Dimensions and material properties of the investigated plates.	89
15	Dimensions and material properties of the investigated plate from [18]. . .	90
16	Device list for laser vibrometer measurements.	94